Single photon measurements: from spin-orbit lattices to ultrafast pulses

by

Sandra Cheng

A thesis
presented to the University of Waterloo
in fulfillment of the
thesis requirement for the degree of
Master of Science
in
Physics (Quantum Information)

Waterloo, Ontario, Canada, 2021

Author's Declaration

This thesis consists of material all of which I authored or co-authored: see Statement of Contributions included in the thesis. This is a true copy of the thesis, including any required final revisions, as accepted by my examiners.

I understand that my thesis may be made electronically available to the public.

Statement of Contributions

As is the case for many scientific endeavours, the work that I detail in this thesis is one of true collaborative effort. Specific notes and acknowledgments are made before the chapters introducing the experiments, but I'd like to point out that Andrew Cameron and I worked closely on both. Nothing that either of us has done, the other hasn't helped with or at least doesn't know about, and we've both taken a fair amount of turns adjusting, aligning and manipulating various parts of both experimental setups. I'd also like to make note that both setups have been heavily worked on by Sacha Schwarz, before he finished his postdoctoral position in the lab group.

Abstract

Single photons are naturally suited to quantum information processes as they can carry entanglement in multiple degrees of freedom and maintain coherence easily. In order to fully harness single photons for this use, it is vital to be able to mould, manipulate and measure their properties in all of these degrees of freedom. In the spirit of working towards this overarching goal, this thesis consists of two experiments that control and evaluate entangled single photon pairs.

In the first, we generate lattices of spin-orbit entangled photon states which are used in a remote state preparation protocol. The success of the protocol is confirmed by using an electron-multiplying intensified CCD camera and a pixelwise tomography technique. We propose that these hybrid lattice states be used in quantum communications, and quantum sensing and control. The pixelwise analysis may also be helpful for observing other spatially-dependent entangled states.

In the second, one partner of an energy-time entangled pair is sent through an ultrafast switch which functions by the optical Kerr effect. It is a work-in-progress with the goal of demonstrating a sub-picosecond switching speed for the further manipulation of single photons. All-optical switching is not limited by electronic speed which makes it important for applications for classical and quantum communications, and imaging and microscopy applications. In particular, we propose that this all-optical Kerr switch is used for the reconstruction of a two-photon entangled state in a third-order cross-correlation.

Acknowledgements

I am lucky to have so many people who support me in various ways. I really can't thank all of you enough, but I shall try. First: I am extremely grateful to my supervisor, Kevin Resch, for giving me a chance. Thanks for taking me under your wing. I've learned an incredible amount by being in this lab group and if I didn't have responsibilities elsewhere, I'd stay for my PhD. Thank you to David Hawthorn and Michael Reimer for taking time out of their busy schedules to agree to sit on my committee.

Next: my deepest, sincerest gratitude to Andrew Cameron. I could not have asked for a better lab partner. You've taught me an extreme amount, both inside and outside the lab. You've supported and guided me throughout most of my time at IQC. Thanks for the introducing me to more bands. I could go on but...I don't really have the words. I think you know how I feel, anyways.

Michael Grabowecky: without you, I wouldn't have passed my courses. Thanks for always answering my questions and being patient. Benjamin MacLellan: a new and awesome addition with good cheer. Thanks for sitting with me and helping me pass my G2 driving test. Christopher Pollack: for that mildly illegal crack. Jack Bishop and Benjamin Wong: for the funnies and your good-natured personalities. Sacha Schwarz: for your advice in the lab. Patrick Daley: for his mathematical perspective and teaching personality. Ruoxuan Xu: for your company. Eugene Adjei: for your brilliant grin and mind. John Donohue: for basically being our unpaid postdoctoral fellow and further introducing me to outreach. Other past members of the lab: thanks to the spirits you've left, because I don't know what I would've done without your notes. Additional thanks must be given to Andrew, Ben, Ben, Jack and Mike for editing my thesis, and everyone else who's offered.

Thanks to our enthused and friendly neighbourhood scientists in Thomas Jennewein's lab: Joanna Krynski, Ramy Tannous, Wilson Wu, Youn Lee. Others at IQC, including Alex, Twesh, and Shayan for always taking the time to chat whenever we saw each other before COVID-19. My Waterloo friends that came with me from Queen's: Hadiya Ma, for your encouragement, your company, your gym, and lending me your personality so that I wasn't totally an antisocial hermit at Waterloo. Tong Song: for making me food when I'm hungry, lending me your car, and overall support. Turner Garrow: for helping me get through tough quantum questions.

Thank you to the collaborators on my experiments, especially Kate Fenwick: you've always made me feel welcome, even when I was just an undergrad. Thanks to IQC's staff and support. I could go on, but I'll end with this: I wouldn't have made it to graduate school in the first place without support from my Queen's friends, professors, and colleagues. You know who you are. Thanks for backing me.

Dedication

This is dedicated to my family, to Andy Huynh, to any marginalized person who's trying to make it in science, and to you, especially if you feel like you're not good enough.

Table of Contents

List of Figures

List of Tables

List of Abbreviations

3WM Three-wave mixing 17, 23, 28, 30

APD Avalanche photodiode 15, 21, 63, 65

BBO Barium borate (either α- or β-cut), BaB_2O_4 28, 31

BiBO Bismuth triborate, BiB_3O_6 28, 31, 62

BS Beamsplitter 19, 21

CPTP Completely positive and trace-preserving 7

DFG Difference-frequency generation 28

DoF Degree of freedom 10, 13, 15, 17, 39, 88

EMCCD Electron-multiplying charged coupled device 45

emICCD Electron-multiplying intensified charged coupled device 39, 40, 45, 46, 49, 52, 81, 83, 84

FROG Frequency-resolved optical gating 37, 68

FWHM Full width at half maximum 35, 37, 48, 57, 58

GVD Group velocity dispersion 27

He:Ne Helium-neon laser xi, 59–61, 63

HWP Half-wave plate 13–16, 41, 48, 59, 63, 83

ICCD Intensified charged coupled device 45

LOCC Local operations and classical communication 6, 42

LOV "Lattice of Optical Vortices" xii, 40, 43–45, 48, 52, 83, 85

OAM Orbital angular momentum x, 10, 11, 13, 39, 40, 43, 45, 52

OKS Optical Kerr shutter 56

PBS Polarising beamsplitter 9, 13, 15, 16, 41, 48, 59, 63, 83, 84

POVM Positive operator-valued measure 4, 5

ppKTP Periodically-poled potassium titanyl phosphate, $KTiOPO_4$ 41, 48

QWP Quarter-wave plate 13–16, 48, 83, 85

RSP Remote state preparation x, 1, 20, 22, 30, 31, 39–43, 45–47, 52, 84

SFG Sum-frequency generation x, 28, 35–37, 55, 60, 63, 68

SHG Second harmonic generation x, 28, 31, 36, 62

SMF Single-mode fibre 48, 59, 61–63, 88

SPDC Spontaneous parametric down-conversion x, 17, 18, 20, 21, 28, 29, 31, 41, 48, 62, 87, 88

SPIDER Spectral phase interferometry for direct electric-field reconstruction 37

SPM Self-phase modulation 32, 65

VI Virtual Instrument (LabVIEW code) 87

XPM Cross-phase modulation 32, 56

Chapter 0: Introduction

This thesis is made up of five chapters. I've tried to write this thesis such that each subsequent chapter builds upon its predecessors, but there are some overlaps. Chapters 1 to 3 cover background material from quantum mechanics, experimental quantum optics, and ultrafast and nonlinear optics. Chapter 4 contains information regarding the remote state preparation of spin-orbit lattices, which is often abbreviated as 'the RSP experiment' in this thesis. Chapter 5 contains information on the Kerr switching of entangled photons, which is often shortened to 'the switching experiment' in this thesis.

Chapter 1

A crash course in quantum mechanics

In order to speak about single photons, we will need to know the formalism of quantum mechanics, as it is the fundamental theory which describes nature around the scale of subatomic particles. This chapter is a brief summary of some of the necessary elements in quantum mechanics so that this thesis may be somewhat self-contained (Dirac notation, for example, is not explained). There are many textbooks which teach quantum mechanics (e.g. Ref [1] which was liberally perused) and may serve as helpful companions.

Section 1.1 introduces a notation for describing pure and mixed states. Section 1.2 talks about measuring states. Section 1.3 brings up the idea of combining more than one state into a bigger system and delves into entangled and separable states. Section 1.4 is about transforming and operating on states, and finally Section 1.5 gives a measure for comparing states.

1.1 State vectors and density matrices

Any isolated physical quantum system is associated with a Hilbert space $\mathcal{H}$, which is a complex vector space with an inner product[1]. The system is completely described by a state vector $|\psi\rangle$, which is a unit vector in the Hilbert space. $|\psi\rangle$ contains all of the information needed to tell us how the system interacts with another system, the environment, and measurements.

States can be classified as being pure or mixed. A pure state cannot be thought of as a probabilistic mixture of other states. The converse of a pure state is a mixed state, in that

[1] This allows lengths and angles to be defined in the state space.

it has to be made of a probabilistic combinations of pure states. In quantum mechanics, states are allowed to exist as a superposition of different states, but this is not the same as a probabilistic mixture of pure states. A superposition of pure states is still a pure state. An example of a superposition of the states $|0\rangle = \begin{pmatrix}1\\0\end{pmatrix}$ and $|1\rangle = \begin{pmatrix}0\\1\end{pmatrix}$ is

$$|\psi\rangle_{pure} = \alpha|0\rangle + \beta|1\rangle \tag{1.1}$$

where $|\alpha|^2 + |\beta|^2 = 1$. In the case of an equal superposition, $\alpha = \beta$ such that:

$$|\psi\rangle_{pure\ ex.} = \frac{1}{\sqrt{2}}|0\rangle + \frac{1}{\sqrt{2}}|1\rangle. \tag{1.2}$$

Instead of using state vectors to describe a state, we can also use an equivalent formulation known as the density operator or density matrix. It is necessary to use this formalism to describe a mixed state, as a mixed state cannot be described by a single ket. A pure state $|\psi\rangle$ is related to its density matrix $\hat{\rho}$ by

$$\hat{\rho}_{pure} = |\psi\rangle\langle\psi|. \tag{1.3}$$

Applying Eq. 1.3 to Eq. 1.2 reveals its density matrix to be:

$$\begin{aligned}\hat{\rho}_{pure\ ex.} &= \frac{1}{2}\big(|0\rangle\langle 0| + |0\rangle\langle 1| + |1\rangle\langle 0| + |1\rangle\langle 1|\big)\\ &= \frac{1}{2}\left[\begin{pmatrix}0\\1\end{pmatrix}\begin{pmatrix}0 & 1\end{pmatrix} + \begin{pmatrix}0\\1\end{pmatrix}\begin{pmatrix}1 & 0\end{pmatrix} + \begin{pmatrix}1\\0\end{pmatrix}\begin{pmatrix}0 & 1\end{pmatrix} + \begin{pmatrix}1\\0\end{pmatrix}\begin{pmatrix}1 & 0\end{pmatrix}\right]\\ &= \frac{1}{2}\begin{pmatrix}1 & 1\\1 & 1\end{pmatrix}.\end{aligned} \tag{1.4}$$

A mixed state, in contrast to Eq. 1.3, is a probabilistic mixture of pure states, so its density matrix is described as a sum:

$$\hat{\rho}_{mixed} = \sum_i p_i|\psi_i\rangle\langle\psi_i|, \tag{1.5}$$

where $\sum_i p_i = 1$. For example, take the probabilistic mixture of the states $|0\rangle$ and $|1\rangle$, as opposed to an equal superposition of the states as represented by Eqs. 1.2 and 1.4. Its density matrix is

$$|\psi\rangle_{mixed\ ex.} = \frac{1}{2}|0\rangle\langle 0| + \frac{1}{2}|1\rangle\langle 1| \tag{1.6}$$

$$= \frac{1}{2}\begin{pmatrix}1 & 0\\0 & 1\end{pmatrix}. \tag{1.7}$$

Density matrices should be normalized in that the trace equals 1.

1.2 Quantum measurements

The most general quantum measurement is a positive operator-valued measure (POVM). Suppose that we have a collection of measurement operators $\{\hat{M}_m\}$. These operators act on the state space of some quantum state $|\psi\rangle$ which is equally represented by its density matrix $\hat{\rho}$. The index m refers to the measurement outcomes which can occur in an experiment. If a measurement operator acts on the state $|\psi\rangle$, the probability that result m occurs is

$$p(m) = \langle\psi|\hat{M}_m^\dagger \hat{M}_m|\psi\rangle, \tag{1.8}$$

Eq. 1.8 is more familiarly known as Born's rule. Measurement operators also satisfy the completeness equation because probabilities sum to one:

$$\sum_m \hat{M}_m^\dagger \hat{M}_m = \mathbb{1} \tag{1.9}$$
$$1 = \sum_m p(m) = \langle\psi|\hat{M}_m^\dagger \hat{M}_m|\psi\rangle.$$

Now we define a POVM element which is a positive operator:

$$\hat{E}_m \equiv \hat{M}_m^\dagger \hat{M}_m. \tag{1.10}$$

As above, $\sum_m \hat{E}_m = \mathbb{1}$ and also $p(m) = \langle\psi|\,\hat{E}_m\,|\psi\rangle = \mathrm{Tr}[\rho\hat{E}_m]$. A POVM is a set of these operators $\{\hat{E}_m\}$ measured in a Hilbert space. A POVM is sufficient to determine the probabilities of different measurement outcomes, but cannot reveal the post-measurement state of a system, since we are not given the actual measurement operators $\{\hat{M}_m\}$ themselves.

Projective measurements are a special subclass of POVM measurements. This is the case that $\{\hat{E}_m\}$ are orthogonal projection operators, which shall now be labelled as $\{\hat{P}_m\}$ for clarity:

$$\hat{P}_m \hat{P}_{m'} = \delta_{m,m'} \hat{P}_m. \tag{1.11}$$

In only this instance, all of the POVM elements are actually the measurement operators themselves as $\hat{E}_m \equiv \hat{P}_m^\dagger \hat{P}_m = \hat{P}_m$. The projectors can be written as

$$\hat{E}_i = \hat{P}_i = |k_i\rangle\langle k_i|\,. \tag{1.12}$$

where $|k\rangle$ is a set of vectors on the Hilbert space. Consider again the example of the quantum state $|\psi\rangle$ with density matrix $\hat{\rho}$. In the case of projective measurement, Eq. 1.8 simplifies to

$$p(m) = \langle\psi|\,\hat{P}_m\,|\psi\rangle = \mathrm{Tr}[\hat{\rho}\hat{P}_m]. \tag{1.13}$$

Given that m is the outcome, then the state of the quantum system after measurement is definitively

$$\frac{\hat{P}_m |\psi\rangle}{\sqrt{p(m)}}. \tag{1.14}$$

Here is a classic example from the quantum information field. Let there be some state $|\psi_{trial}\rangle = \alpha |0\rangle + \beta |1\rangle$ where again, α, β are complex and $|\alpha|^2 + |\beta|^2 = 1$. This state is said to be written in the computational basis, which consists of $|0\rangle$ and $|1\rangle$ with the same definitions as previously introduced in Section 1.1. Let $\hat{M}_0$ be the projector which reads out $m = 0$ and $\hat{M}_1$ be the projector which reads out $m = 1$. Then

$$\hat{M}_0 = |0\rangle \langle 0| = \begin{bmatrix} 1 & 0 \\ 0 & 0 \end{bmatrix}$$
$$\hat{M}_1 = |1\rangle \langle 1| = \begin{bmatrix} 0 & 0 \\ 0 & 1 \end{bmatrix}.$$

$\hat{M}_0$ and $\hat{M}_1$ are orthogonal since $\langle 0| 1\rangle = 0$, so I relabel the measurement operators as $\hat{P}_0$ and $\hat{P}_1$. The probability of obtaining the measurement outcome 0 is

$$p(0) = \langle \psi_{trial}| \hat{M}_0^\dagger \hat{M}_0 |\psi_{trial}\rangle = \langle \psi_{trial}| \hat{M}_0 |\psi_{trial}\rangle = |\alpha|^2, \tag{1.15}$$

and the final state of $|\psi_{trial}\rangle$ is

$$\frac{\hat{P}_0 |\psi\rangle}{\sqrt{p(m)}} = \frac{\alpha}{|\alpha|} |0\rangle. \tag{1.16}$$

General POVMs are not used in the experiments in this thesis, only projectors.

1.3 Composite systems and entanglement

Suppose now that we have two isolated systems, A and B, combined in a composite system. The state of the bipartite system $|\psi_{AB}\rangle$ is also a normalized vector in a Hilbert space defined

$$\mathcal{H}_{AB} = \mathcal{H}_A \otimes \mathcal{H}_B. \tag{1.17}$$

The combined Hilbert space is made up of the tensor product between the individual Hilbert spaces of the subsystems A and B. The joint state of the system, given that $|\psi_A\rangle$ and $|\psi_B\rangle$ are the state vectors of the subsystems, is now

$$|\psi_{AB}\rangle = |\psi_A\rangle \otimes |\psi_B\rangle \tag{1.18}$$

which is more commonly abbreviated as $|\psi_A\rangle |\psi_B\rangle = |\psi_A \psi_B\rangle$. Eqs. 1.17 and 1.18 can be generalized to any number of subsystems, although this thesis is limited to bipartite systems. Due to the superposition principle, any normalized sum of the two state vectors from each subsystem is a valid state vector of the bipartite system. However, all the possible states created by superposition do not share the same characteristics.

Any state in $\mathcal{H}_{AB}$ which can be represented in the exact form in Eq. 1.18 is a separable pure state. The most general form of a separable state is

$$|\psi\rangle_{separable} = \sum_m p_m \hat{\rho}_m^A \otimes \hat{\rho}_m^B. \tag{1.19}$$

Following the notation in the previous sections, $\hat{\rho}_m^A$ and $\hat{\rho}_m^B$ are the density matrices of a state, respectively in subsystems A and B, when measured with some outcome m individually (systems A and B have not yet combined at the time of measurement). p_m is the probability that result m occurs. $p_m \geq 0$ and $\sum_m p_m = 1$. Any state which can be decomposed into Eq. 1.19 has classical correlations. This is to say separable states can be created using classical physics: only local operations and classical communication (LOCC) are necessary[2]. I think this is easily seen with the description of Eq. 1.19 by Ref. [2]. Say the systems A and B each have a remote with settings $m = 1, ..., n$, and that by setting m the systems produce states $\hat{\rho}_m^A$ and $\hat{\rho}_m^B$. Say that a random number generator is responsible for producing the numbers $m = 1, ..., n$ with probability p_m. The physical "source" of the correlations is the random number generator which can be a purely classical device.

By definition, an entangled state is one which is not separable [3, 4]. Colloquially, a maximally entangled state means that the subsystems have such strong correlations with each other that they cannot be described separately but rather collectively (you can replace the word 'state' with 'particles', if you like)[3]. Entangled states can be pure or mixed. Just as entangled states cannot be created with local operations (only global operations), local operations cannot affect the degree of entanglement [5]. Local operations can, however, be used to distinguish certain entangled states [6], as is the case in this thesis. See Section 4.2.2 later.

Important examples of pure maximally entangled bipartite states in quantum informa-

[2]Briefly, a local operation in this context refers to a product operation. It acts on one of the subsystems but not the others. Results obtained at one location are independent of any actions performed with space-like separation [3]. Classical communication is communication in the regular sense e.g. one scientist calling up another to tell them of their results.

[3]Non-maximally entangled states exist, but are beyond the scope of this thesis. [7] might be an interesting read regarding the topic.

tion are the four Bell states:

$$|\Phi^+\rangle = \frac{1}{\sqrt{2}}(|00\rangle + |11\rangle) \tag{1.20}$$

$$|\Phi^-\rangle = \frac{1}{\sqrt{2}}(|00\rangle - |11\rangle) \tag{1.21}$$

$$|\Psi^+\rangle = \frac{1}{\sqrt{2}}(|01\rangle + |10\rangle) \tag{1.22}$$

$$|\Psi^-\rangle = \frac{1}{\sqrt{2}}(|01\rangle - |10\rangle). \tag{1.23}$$

They are written in the computational basis as introduced in an example in Section 1.2.

1.4 Transforming quantum states

Up to this point, only isolated systems have been discussed. In reality, all systems interact with others[4]. Measuring a system necessarily means that it is no longer isolated. However, a natural way to describe the dynamics of an open system is to think about a principal system and its interaction with another (say, the environment or a measurement probe) as another closed system.

It is possible to describe an isolated system as it evolves in time by relating the changes in the system's state to the energy in the system. Consider the Schrödinger picture, where it is the quantum state which changes in time as it interacts with its surroundings and other systems, while it is the operators which remain constant in time. Transformations on the state are represented by operators. These should be completely positive and trace-preserving (CPTP) so that when applied to a density matrix, a valid density matrix is output [1].

An important and ubiquitous subclass of CPTP operators are unitary operators. They have the property

$$U^\dagger U = UU^\dagger = \mathbb{1}. \tag{1.24}$$

Applying a unitary operator to a starting quantum state $|\psi\rangle$ or equivalently applying a unitary matrix on a starting density matrix $\hat{\rho}$ transforms it as such:

$$|\psi'\rangle = \hat{U}|\psi\rangle \tag{1.25}$$

$$\hat{\rho}' = \hat{U}\hat{\rho}\hat{U}^\dagger. \tag{1.26}$$

[4]Except the universe as a whole.

Projective measurement operators as described in Section 1.2 are unitaries. A set of important unitaries are the Pauli-X, Pauli-Y and Pauli-Z operators:

$$\hat{\sigma}_x = \begin{pmatrix} 0 & 1 \\ 1 & 0 \end{pmatrix}, \hat{\sigma}_y = \begin{pmatrix} 0 & -i \\ i & 0 \end{pmatrix}, \hat{\sigma}_z = \begin{pmatrix} 1 & 0 \\ 0 & -1 \end{pmatrix}. \tag{1.27}$$

1.5 Quantum fidelity

Quantum fidelity is a type of distance measure between two states which compares how close they are. It expresses the probability that one state passes for the other and defined as [8]

$$\mathcal{F}(\hat{\rho}, \hat{\sigma}) \equiv \mathrm{Tr}\left[\sqrt{\sqrt{\hat{\rho}}\hat{\sigma}\sqrt{\hat{\rho}}}\right]^2. \tag{1.28}$$

For any quantum states $\hat{\rho}$ and $\hat{\sigma}$, $0 \leq \mathcal{F}(\hat{\rho}, \hat{\sigma}) \leq 1$ and $\mathcal{F}(\hat{\rho}, \hat{\sigma}) = \mathcal{F}(\hat{\sigma}, \hat{\rho})$. When calculating the fidelity between a pure state $\hat{\rho} = |\psi\rangle\langle\psi|$ and an arbitrary state, Eq. 1.28 explicitly becomes:

$$\mathcal{F}(\hat{\rho}, \hat{\sigma}) = \langle\psi|\hat{\sigma}|\psi\rangle = \mathrm{Tr}\Big[\hat{\sigma}|\psi\rangle\langle\psi|\Big] \tag{1.29}$$

where the second equality is gained by applying Eq. 1.13. Eq. 1.29 is used often in the lab to see how close our created state $\hat{\sigma}$ is to the theoretical state $\hat{\rho}$. The problem then becomes finding the entries of $\hat{\sigma}$, which is often done by quantum state tomography (detailed further in Section 4.2.5).

Chapter 2

A crash course in experimental quantum optics

Light is a propagation of electromagnetic waves. To get a quantum description of light, the electromagnetic field must be quantized, and by doing so, we have a definition for the photon. A photon is a discrete excitation of the electromagnetic field. Quantum optics is the study of photons and their particle-like behaviour, including how photons interact with other atoms and molecules. This thesis describes two single photon measurement experiments, so this chapter presents some important concepts and tools in optics which we use to carry out the quantum mechanical principles described in Chapter 1.

Section 2.1 explains the photon's role in the field of quantum information. Section 2.3 introduces the idea of polarization, from what it means for light as a wave and what it means in a photon. Section 2.4 talks about waveplates, which work on the principle of birefringence and are widely-used tools in an optics lab. Section 2.5 is all about the use of polarizing beamsplitters (PBSs) as projectors. Sections 2.6 and 2.7 bring up the topics of polarization and energy-time entanglement in photons. Section 2.8 wraps up the chapter by discussing the $g^{(2)}(0)$ measurement, which is a common experimental check to confirm if the photon distribution has quantum character.

2.1 The photon's place in quantum information

When we speak of quantum information, we necessarily speak of qubits. The qubit, or quantum bit, is a two-level quantum system and is the basic fundamental unit of quantum

information, much like how a classical bit is to classical information. While the classical bit is restricted to being either 0 or 1, the qubit can be either $|0\rangle$ or $|1\rangle$ or some linear combination of both at the same time, which you have already seen in the previous chapter. As written in Section 1.2, the state of a qubit $|\psi\rangle$ is represented mathematically as:

$$|\psi\rangle = \alpha\,|0\rangle + \beta\,|1\rangle \tag{2.1}$$

with $|\alpha|^2 + |\beta|^2 = 1$ for normalization. Any physical system which can realise any of the possible superpositions can be used to encode a qubit. There are many candidates such as the atomic levels in atoms and ions [9], superconductors [10], and nuclear spin of particles [11], but in this lab, we use single photons.

There are many ways of encoding a photonic qubit, and this is due to the four main degrees of freedom (DoFs) of photons. These are polarization, energy/time, the radial number, and angular momentum. In a beamlike geometry, the latter two are encompassed by the transverse mode profile [12]. Some common DoFs used in experiments are frequency, time bins, polarization, and spatial distribution arising from orbital angular momentum (OAM). Each has its own advantages and disadvantages. This thesis features OAM and polarization entangled qubits, and energy-time entangled qubits.

2.2 Orbital angular momentum

The azimuthal quantum number, also known as the orbital angular momentum quantum number, determines the OAM of a particle. It is typically denoted as l, and as a consequence of quantization, its value has to be an integer, either positive or negative[1]. In light, OAM is caused by spatially-varying amplitude and phase distributions [13]. Light beams which have OAM have a helical phase structure, where the phase winds azimuthally around the optical axis. This is most easily visualized in cylindrical coordinates, where the optical axis, which is the axis in which the light travels, is $\hat{z}$ and the phase of the light is captured by the azimuthal coordinate $\hat{\phi}$. The magnitude of l describes the number of times that the azimuthal component has travelled a full 2π circumference. Fig. 2.1(a) shows the helical structures produced by the first few positive l values. Positive and negative signs refer to different travel directions which produces handedness in the helical phase structure, shown in Fig. 2.1(b).

[1]It is often shown that l is restricted to positive values. However, this restriction only arises from squaring the angular momentum operator, typically denoted as $\hat{L}$.

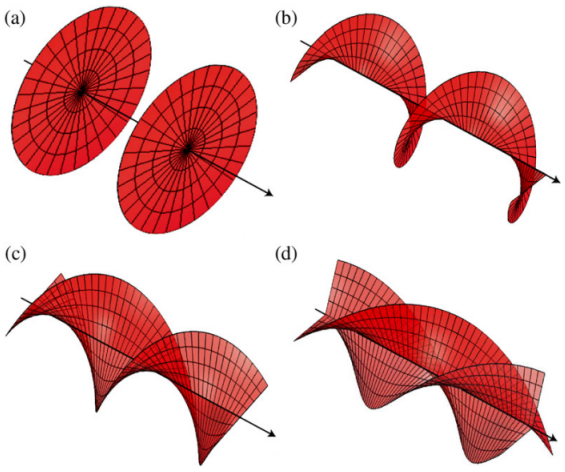

(a) Depiction of the helical phase fronts for beams which have different positive l values. The top-left image, (a), is a plane wave corresponding to $l = 0$. (b) is a single helix corresponding to $l = 1$. (c) is a double-fold helix corresponding to $l = 2$. (d) is a triple-fold helix (pasta fusilli-shaped) corresponding to $l = 3$. Image from Ref. [14].

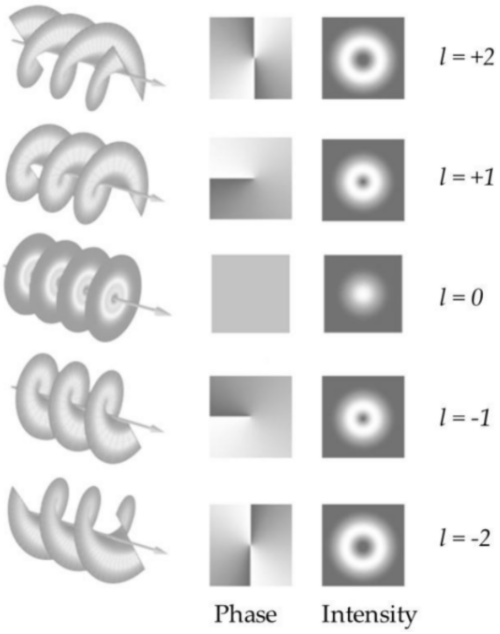

(b) Depiction of optical beams which contain positive and negative OAM. The first column is the beam helical structure (similar to the figure on the left). The second and third columns respectively show the phase and intensity distributions in a cross-section of the corresponding beam. Image from Ref. [15].

Figure 2.1: Images of the beam wavefront shape for different OAM values of l. (a) shows positive l values while (b) compares positive and negative values, as well as showing phase and intensity distributions with beam cross-sections. It is helpful to use cylindrical coordinates, where the beam travelling along $\hat{z}$ and the phase fronts wind around $\hat{\phi}$.

2.3 Polarization

An electromagnetic wave travels in a way such that its electric and magnetic field components always oscillate perpendicular to each other and the direction of travel. Polarization refers to the direction in which the electric field oscillates with respect to some reference, such as an optical table. The axis in which the light travels (parallel to the surface) is often labelled $\hat{z}$, and we follow this convention. So for any beam of light travelling in the

$\hat{z}$ axis, the light can be polarized in the $\hat{x}$ (horizontal) or $\hat{y}$ (vertical). Photons are often thought of in this manner as well.

By only working with photons which are effectively identical except for their polarization, we can describe a photon's state solely by its polarization. Any other transformations on the state are assumed to be blind to all the other properties of the photon. The common encoding convention associates the physical electric field oscillation direction with the computational basis such that:

$$|H\rangle = |0\rangle = \begin{pmatrix} 1 \\ 0 \end{pmatrix}, |V\rangle = |1\rangle = \begin{pmatrix} 0 \\ 1 \end{pmatrix} \tag{2.2}$$

where $|H\rangle$ and $|V\rangle$ respectively refer to horizontally- and vertically-polarized light. An arbitrary pure state in the polarization basis is written as [1]:

$$|\psi\rangle = \cos(\frac{\theta}{2}) |H\rangle + e^{i\phi}\sin(\frac{\theta}{2}) |V\rangle , \tag{2.3}$$

where $0 \leq \theta \leq \pi$ and $0 \leq \phi \leq 2\pi$. I now introduce the notion of the Bloch sphere, which is a 3D sphere that geometrically represents the pure state space of a qubit. Using the computational basis, each pair of antipodal points correspond to a pair of mutually orthogonal state vectors. Unitary operations on the qubit correspond to rotations about the Bloch sphere. Axes correspond respectively to Pauli matrices e.g. a full rotation about the $\hat{z}$-axis is equivalent to applying the $\hat{\sigma}_z$ operator on the qubit. Similarly, the Poincaré sphere is a visualization tool for different polarized light. By now assigning each state vector in the computational basis to a polarization, Eq. 2.3 can be visualized in Fig. 2.2. The six listed states are also known as equatorial states due to their positions on the sphere. The complete polarization convention used in this thesis is listed in Table 2.1. $\{|H\rangle, |V\rangle\}$, $\{|D\rangle, |A\rangle\}$ and $\{|R\rangle, |L\rangle\}$ are not only mutually orthonormal, they are mutually unbiased bases. This means that if a state is prepared in one of these bases, all outcomes are equally probable when a measurement is made in any of the other two bases [16].

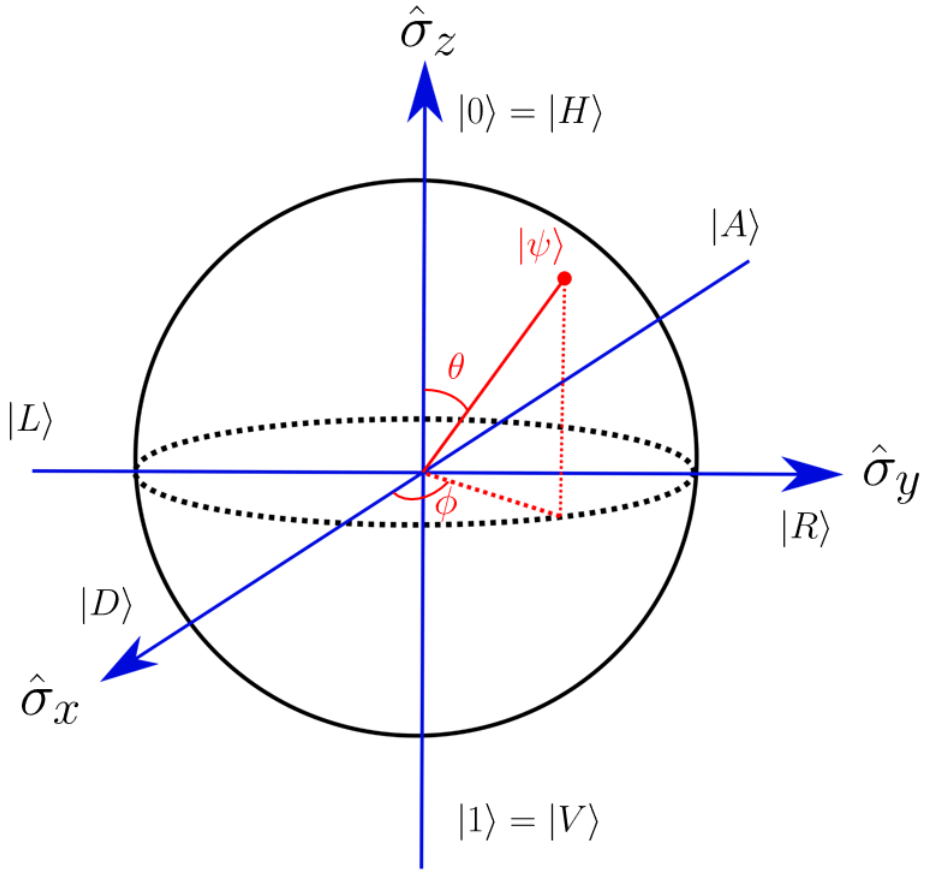

Figure 2.2: Bloch sphere labelled with polarizations as per Table 2.1. The axes correspond to Pauli matrices. All pure states e.g. $|\psi\rangle$ begin at the centre of the sphere and end at the surface of the sphere. Note that the $\{|H\rangle, |V\rangle\}$, $\{|D\rangle, |A\rangle\}$, and $\{|R\rangle, |L\rangle\}$ states are the respective eigenstates of the Pauli-Z, Pauli-X, and Pauli-Y operators.

One of the big advantages of using the polarization DoF is total control. It is straightforward to manipulate a photon's polarization state using half-wave plates (HWPs), quarter-wave plates (QWPs) and polarizing beamsplitters (PBSs).

The polarization of a photon is also related to its quantum spin number, typically denoted as m_s. By projecting the spin operator, typically denoted as $\hat{S}$, in the propagation direction, the resulting two eigenstates are $|R\rangle$ and $|L\rangle$. I note this for a comparison to the description of OAM in Section 2.2, though it is sufficient to think about polarization in terms of the electric field oscillation as described above.

Polarization State	Computational Basis
$\|H\rangle$	$\|0\rangle$
$\|V\rangle$	$\|1\rangle$
$\|D\rangle$	$\frac{1}{\sqrt{2}}(\|0\rangle + \|1\rangle)$
$\|A\rangle$	$\frac{1}{\sqrt{2}}(\|0\rangle - \|1\rangle)$
$\|R\rangle$	$\frac{1}{\sqrt{2}}(\|0\rangle + i\|1\rangle)$
$\|L\rangle$	$\frac{1}{\sqrt{2}}(\|0\rangle - i\|1\rangle)$

Table 2.1: Polarization convention used in our lab. $|H\rangle, |V\rangle, |D\rangle, |A\rangle, |R\rangle$, and $|L\rangle$ are respectively referring to the horizontal, vertical, diagonal, anti-diagonal, right- and left-circular polarization states.

2.4 Birefringence and waveplates

Waveplates work via uniaxial birefringence. Consider monochromatic light. As light passes through a medium, it necessarily slows down. We normally refer to this change of speed in an isotropic material (e.g. vacuum, water) using its refractive index n. There exists materials which are composed of atoms in such a way that different polarizations of light experience different refractive indices[2]. This effect is termed birefringence, and the simplest case is uniaxial birefringence where there are two different refractive indices, the ordinary n_o and extraordinary n_e, which are perpendicular to each other. They are respectively the 'fast' and 'slow' axes because light which is polarized along the ordinary axis passes through faster than light which is polarized along the extraordinary axis. Light travelling along the slow axis is delayed and thus obtains a relative phase to light along the fast axis. Birefringence is described by the difference in refractive indices:

$$\Delta n = |n_o - n_e|. \tag{2.4}$$

A HWP and a QWP respectively cause a relative phase delay of $\phi = \pi$ and $\phi = \frac{\pi}{2}$ where ϕ is as described in Eq. 2.3. These are common polarization manipulation tools found in an optics lab made out of birefringent glass. They implement the unitaries [17]:

$$\hat{U}_{HWP}(\theta) = -i \begin{bmatrix} \cos(2\theta) & \sin(2\theta) \\ \sin(2\theta) & -\cos(2\theta) \end{bmatrix} \tag{2.5}$$

$$\hat{U}_{QWP}(\theta) = \frac{1}{\sqrt{2}} \begin{bmatrix} 1 - i\cos(2\theta) & -i\sin(2\theta) \\ -i\sin(2\theta) & 1 + i\cos(2\theta) \end{bmatrix}. \tag{2.6}$$

[2]These are typically transparent optical crystals; all of the ones in this thesis are of this sort.

Eqs. 2.5 and 2.6 are written in the $\{|H\rangle, |V\rangle\}$ basis and θ is the angle between the fast and slow axes. Note that the factor in front of Eq. 2.5 can be dropped since it acts as a global phase. This means that it acts on all light polarizations passing through, so there isn't any relative phase. As an example of using these unitaries, consider a HWP which is aligned so that $\theta = 0$ and $|H\rangle$ and -$|V\rangle$ are the eigenstates of the operation. Then, for example, $\hat{U}_{HWP}(0)|H\rangle = |H\rangle$ and $\hat{U}_{HWP}(0)|V\rangle = -|V\rangle$. $\hat{U}_{HWP}(0)|D\rangle = |A\rangle$ due to the π phase difference. But say $\theta = 22.5°$, then $\hat{U}_{HWP}(22.5°)|H\rangle = |D\rangle$ and $\hat{U}_{HWP}(22.5°)|V\rangle = |A\rangle$. Note that for any angle, $\hat{U}_{HWP}$ flips $|R\rangle$ to $|L\rangle$ and vice versa. Referring back to Fig 2.2, a HWP is able to grant access to any part of the X-Z plane. A QWP at 45° turns $|H\rangle$ to $|R\rangle$ and $|V\rangle$ to $|L\rangle$ which allows us to move in the Y-Z plane. The combination of a HWP and a QWP thus act like single qubit operations and can thus implement any rotation on the Bloch sphere[3].

Sometimes instead of having a fixed relative delay of π or $\pi/2$, we want a variable retarder which can produce any relative delay $0 \leq \phi \leq 2\pi$. A common way to achieve this is to take a birefringent glass and rotate it about an axis perpendicular to the incoming beam. This changes the amount of glass that the light passes through and therefore the relative delay. In one of the experiments, a tilted QWP is used for this purpose.

Fibre polarization controls (informally known as bat ears) act in a similar way to waveplates by inducing birefringence by bending a fibre. Normally, a holder is used so that three sets of coils can be formed with different bending diameters. Experimentally, they are closer to variable retarders.

2.5 Projection by polarizing beamsplitter

PBSs are often used in conjunction with single photon detectors. All of ours are avalanche photodiodes (APDs) and record photon counts only by converting light into measurable charge. They are insensitive to polarization, frequency, etc. One way of circumventing this insensitivity is coupling the polarization DoF into different spatial paths, at the end of which we put detectors. The PBS is an optical tool which accomplishes this by transmitting $|H\rangle$ and reflecting $|V\rangle$. Looking at either end is equivalent to having performed a projective measurement on the $|H\rangle$ or $|V\rangle$ basis.

In our experiments, we typically transform the arbitrary polarization of the studied quantum states to $|H\rangle$ or $|V\rangle$ and then project onto either basis by use of a PBS. Polarizing

[3] A useful waveplate basis conversion guide (takes any of the 6 polarization states to another) can be found in the QOQI Wiki.

analyzing optics in this thesis normally refers to a setup consisting of a HWP followed by a QWP then a PBS. The probability of measuring a state $|\psi\rangle$ at the transmitted port after passing through these optics is

$$\begin{aligned} p(m = |H\rangle) &= \langle\psi| \left(|H\rangle \langle H| \right) |\psi\rangle \qquad \text{Eq. 1.13} \\ &= |\langle H| \hat{U}_{QWP}(\theta_1)\hat{U}_{HWP}(\theta_2) |\psi\rangle|^2. \end{aligned} \tag{2.7}$$

θ_1 and θ_2 are the angles with which to set the QWP and HWP as per Eqs. 2.6 and 2.5.

Besides performing measurement, this setup can be used for other functions. For example, we normally numerically maximize Eq. 2.7 to obtain θ_1 and θ_2 by individually and respectively replacing the HWP and QWP in the setup with ones whose angles are trusted. For another, Section 2.4 mentions that passing light into fibre causes polarization rotations[4]. If there are polarized photons which pass through fibre before emerging at the other end of the optical table, we are able to correct for phase undesirably gained in the fibre by using this set of optics. This is called fibre compensation.

Related to the workings of a PBS is a polarizer, which is a filter that only lets in light of a specific polarization. Since each port of a PBS performs in this manner, they can be considered linear polarizers. A crossed polarizer scheme is made up of a pair of linear polarizers sandwiching an optic, where the polarizers are oriented in a way such that they eliminate all light if they are placed one after another. It is briefly mentioned in chapter 3 and is detailed in chapter 5.

2.6 Polarization entanglement

Common polarization-entangled states produced with light are the Bell states, which were briefly introduced in Eqs. 1.20, 1.21, 1.22, and 1.23. Recall that $|0\rangle = |H\rangle$ and $|1\rangle = |V\rangle$. The Bell states are superpositions of two orthogonal polarization states. For example, take:

$$|\Psi^+\rangle = \frac{1}{\sqrt{2}}(|HV\rangle + |VH\rangle) = \frac{1}{\sqrt{2}}(|DD\rangle - |AA\rangle) = \frac{1}{\sqrt{2}}(|LL\rangle - |RR\rangle), \tag{2.8}$$

where we see strong anti-correlations in $\{|H\rangle, |V\rangle\}$ and strong correlations in $\{|A\rangle, |D\rangle\}$ and $\{|R\rangle, |L\rangle\}$[5]. If we measure the first photon to be $|H\rangle$ (or $|V\rangle$) then we know that the second photon is $|V\rangle$ (or $|H\rangle$). Note that strong correlations in one basis isn't enough to verify the presence of entanglement, since the mixed state $|HV\rangle\langle HV| + |VH\rangle\langle VH|$ can

[4] Unless a polarization-maintaining fibre is used.

also produce the same $\{|H\rangle, |V\rangle\}$ correlations. A key feature of entanglement is being able to produce strong correlations in different bases.

In this thesis, polarization-entangled states are created by spontaneous parametric down-conversion (SPDC), which is one of the most accessible and controllable sources of photon entanglement [18]. Although SPDC is a form of three-wave mixing (3WM) and arises from nonlinear optics, it is a strictly quantum effect. I mention it here briefly for continuity in the topics of polarization and energy-time entanglement, though the details will be revisited later in Section 3.3 where 3WM is discussed.

When high-energy laser light interacts with a nonlinear crystal, a photon normally termed the pump spontaneously down-converts into a pair of entangled photons, normally called the signal and idler, which are lower in energy and travel spatial paths in accordance with the energy and momentum conservation laws. The efficiency of this process is notoriously low, on the order of one photon down-converting out of a million [19]. There are three different kinds of SPDC categorized by the incoming and outgoing photon polarizations:

- Type-0: pump, signal and idler have the same polarization,
- Type-I: pump polarization is orthogonal to both signal and idler,
- Type-II: signal and idler polarizations are orthogonal to each other.

By using the polarization manipulation tools mentioned in previous sections, we can obtain entangled photon pairs that are polarized in a certain manner (effectively generating one of the Bell states, for example).

2.7 Energy-time entanglement

Polarization entanglement is fairly intuitive and easy to measure with optics tools, but cannot be scaled past qubits (to higher-dimensional qudits) easily. Entanglement in the frequency and time domains of light can be potentially high-dimensional which allows for higher carrying capacity of quantum information, so they are popular DoFs among experimentalists [20, 21].

[5] In this context, correlations mean the measurements on both photons turn out the same, and anti-correlations mean that the measurements on both photons are opposite. The word correlations can also encompass both correlations and anti-correlations like in the last sentence of this paragraph. Also note that I dropped the global phase of i from the $\{|R\rangle, |L\rangle\}$ correlations.

We do not study the correlations for energy-time entanglement in this thesis, but an energy-time entangled state is used. It is created via SPDC which naturally produces energy-time entanglement as the energy of the pump photon must equal the sum of signal and idler energies, $\omega_p = \omega_s + \omega_i$. The process is also spontaneous meaning that the photons are birthed during a small time window such that $t_s - t_i \approx 0$. SPDC thus produces strong correlations in the frequency and time domains in direct analogy to the Einstein-Podolsky-Rosen correlations of position and momentum[6]. These are conjugate variables, meaning that their state vectors are related to each other by a Fourier transform.

One way of representing a correlated two-mode state is [22]

$$|\psi\rangle = \int \mathrm{d}\omega_s \mathrm{d}\omega_i F(\omega_s, \omega_i) a_s^\dagger(\omega_s) a_i^\dagger(\omega_i) |0\rangle . \tag{2.9}$$

Eq. 2.9 is a superposition of the [continuous frequency] creation operators, $a_s^\dagger(\omega_s)$ and $a_i^\dagger(\omega_i)$, which act on the vacuum state and are weighted by the spectral distribution $F(\omega_s, \omega_i)$. $F(\omega_s, \omega_i)$ is the joint spectral amplitude and its properties inform if the two photons, typically labelled 'signal' and 'idler' (even if they aren't created by SPDC), are entangled or not. If the photon pair have strong correlations in frequency and time i.e. they are entangled, then the joint spectral amplitude cannot be a product of states: $F(\omega_s, \omega_i) \neq F_s(\omega_s) F_i(\omega_i)$.

The energy-time entanglement can be detected by violations of uncertainty relations. For example, two separable or classical pulses satisfy the following inequality [23, 24]

$$\Delta(\omega_s + \omega_i)\Delta(t_s - t_i) \geq 1, \tag{2.10}$$

where $\omega_{s,i}$ are the frequencies and $t_{s,i}$ are the times of arrival for the signal and idler photon labelled accordingly. Another way of detecting energy-time entanglement is by using interferometry [25, 26].

2.8 Single photon character: second-order coherence

Quantum and classical light have different statistical distributions which lead to different correlation functions. To gain insight into the type of state created, it is convenient to measure the degree of second-order temporal coherence, which is written as $g^{(2)}(\tau)$. It is a

[6]Note that time is not an observable in quantum mechanics. When speaking about the timing of a photon, we are referring to the intensity as a function of time (which is an observable).

measure of the average correlation between the intensity of a field at two different times, and τ is the time difference.

Consider the second-order coherence function at the zero time delay, $g^{(2)}(0)$. In a quantum optics lab, it corresponds to a measurement which gives the probability of two photons existing at the same instant in time, normalized by the probability of finding a single photon at that time. This can be done by sending the quantum state into a non-polarizing 50:50 beamsplitter (BS) with a detector in each path. A 50:50 BS simply transmits and reflects light with equal probability. The setup is known as a Hanbury Brown-Twiss interferometer [24, 27] and shown in Fig 2.3. Photons are discrete and must end up in one port or the other, so in a perfect laboratory, the probability of two photons existing at the same instant in time is 0 and there are no coincidences (both detectors should not register at the same time; numerator is 0). Perfect single photon light is thus described by $g^{(2)}(0) = 0$, where a $g^{(2)}(0)$ closer to 0 indicates a closer statistical description to that of true single photon light. However, any $g^{(2)}(0) < 1$ is a signature of quantum light[7].

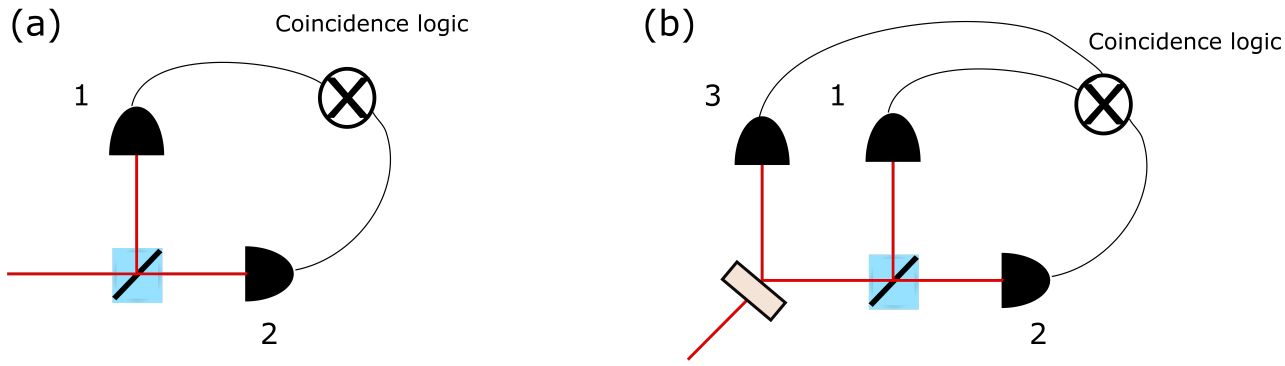

Figure 2.3: Two different $g^{(2)}(0)$ measurements. (a) is an unheralded measurement while (b) is heralded.

In Fig. 2.3(a), $g^{(2)}(0)$ is the probability of measuring a coincidence between detectors 1 and 2, divided by the probability of measuring a photon count (getting a 'click') at each

[7]Starting from second-order temporal coherence function for a classical light field, one can apply Cauchy's inequality and see that for classical light, $g^{(2)}(0) \geq 1$. The same treatment can be done for non-classical light using electric field operators to find that $g^{(2)}(0) < 1$. Ref. [24] takes us through the derivation.

detector [28]. These probabilities are obtained from measured count rates. The probability of a detection at detector 1 within some time frame is given by the average rate of detections at detector 1 multiplied by this time frame. The average rate is simply the total number of detections divided by the total counting time. If we let the detection time frame be Δt, the average rate be R, the total number of detectors be N and the total counting time be ΔT, then the probabilities for detectors 1 and 2, and probability of coincidence counts between them are [29]:

$$P_1 = R_1 \Delta t = \frac{N_1}{\Delta T}\Delta t, \qquad P_2 = R_2 \Delta t = \frac{N_2}{\Delta T}\Delta t \tag{2.11}$$

$$P_{1,2} = R_{1,2} \Delta t = \frac{N_{1,2}}{\Delta T}\Delta t. \tag{2.12}$$

The $g^{(2)}(0)$ in general is thus:

$$g^{(2)}(0) = \frac{P_{1,2}}{P_1 P_2} \tag{2.13}$$

$$g^{(2)}(0) = \frac{N_{1,2}}{N_1 N_2}\frac{\Delta T}{\Delta t} \tag{2.14}$$

Typically, all rates are given in a second ($\Delta T = 1$) and the coincidence window is a shorter time frame, usually $\Delta t = 3$ ns. Eq. 2.14 is more commonly seen as:

$$g^{(2)}(0) = \frac{P_{1,2}}{P_1 P_2} = \frac{N_{1,2}}{N_1 N_2}\frac{1}{\Delta t_{window}}. \tag{2.15}$$

Many experiments calculate the second-order coherence in a heralded manner as depicted in Fig 2.3(b). Both the RSP and the switching experiments do this, whereby counts from one photon is only kept if its presence has been heralded by another. This is often done with a process in which two photons are created at the same time (e.g. via SPDC; the brown rectangle in Fig 2.3(b) is the nonlinear crystal). A coincidence count registered by detectors 1 and 2 is only kept if detector 3 also clicks, which helps cut down on noise. The $g^{(2)}(0)$ is now the probability of a three-fold coincidence between all detectors divided by the two-fold coincidences between detectors 1 and 3, and detectors 2 and 3. In this case, the probability of measuring a photon is the number of photons N divided by the number of heralds. Similarly to above, the probabilities are [29]:

$$P_1 = \frac{N_{1,3}}{N_3}, \qquad P_2 = \frac{N_{2,3}}{N_3} \qquad P_3 = \frac{N_{1,2,3}}{N_3}, \tag{2.16}$$

where we include the new terms $N_{1,2,3}$, which is the number of threefold coincidences, and N_3, the number of counts at detector 3.

$$g^{(2)}(0) = \frac{P_{1,2,3}}{P_{1,3}P_{2,3}} = \frac{N_{1,2,3}}{N_{1,3}N_{2,3}}N_3 \tag{2.17}$$

There is no need to include the coincidence window or total counting time, since the herald is used as a common reference in this case. Eqs 2.15 and 2.17 work for continuous wave lasers. A continuous wave laser is one which is emitted as a continuous beam of light, in contrast to a pulsed laser which emits light in short bursts ('pulses'). A pulsed laser with a repetition rate R produces $1/R$ photons per second, which must be accounted for since having a greater number of photons in a second contributes to a higher number of accidental coincidences. With Eq. 2.15, simply include $1/R$ in the probability denominator, which results in $g^{(2)}(0) = \frac{N_{1,2}R}{N_1 N_2 \Delta t_{window}}$ where the counting time is performed over a time period of a second, as we specified the use of the repetition rate. Other accidental calculations are described by [30]. Accidentals can come from other sources like double-pair emission in SPDC where two photons instead of one are down-converted.

This discussion above pertains to the average intensity correlation of a single field with itself so the $g^{(2)}(0)$ is often called the autocorrelation function[8]. We can also think about the coherences of two spatially or temporally distinct beams, and this instead is referred to as a cross-correlation. The setup would simply be two detectors in each beam path which register coincidences with each other (no BS needed), and the probabilities can be deduced similarly to get an equation identical to Eq. 2.15. The $g^{(2)}(0)$ is often used by experimentalists to ensure that the photons they use still retain quantum character even after passing through a myriad of optics.

A short note regarding the coincidence window: in many quantum optics labs (including ours), the coincidence window is set to be 3 ns partially due to timing jitter. Timing jitter determines the timing resolution of a detector. As photons cause corresponding electric charge in APDs, these electrical pulses are sent to timing electronics which attach time tags to them. However, there is timing uncertainty between the optical signal being input and the output of the electrical signal and this delay is always fluctuating. The width of this statistical distribution is the timing jitter. For most APDs, this is on the order of a nanosecond [31]. 3 ns is an empirical number which maximizes the signal-to-noise ratio of true coincidences. It's a short enough timeframe to cut out noise, but longer than the timing jitter and long enough so that the coincidence count isn't reduced artificially.

[8] *Auto* is a Greek prefix meaning 'self'.

Chapter 3

Ultrafast and nonlinear optics

Ultrafast optics deal with ultrafast phenomena: events that have features which occur within picosecond (ps; 10^{-12} s) timescales or less. This includes ultrashort pulses, which are light pulses that have temporal widths that range from picoseconds to femtoseconds (fs; 10^{-15} s). To put this in perspective, consider a 1-s-long light pulse. Distance is equal to speed multiplied by time, so this hypothetical pulse stretches over 300,000 km. In comparison, a 0.1-ps pulse has an approximate width of 30 μm. Ultrashort pulses have several characteristics which make them useful [32], namely:

- High timing resolution; since the pulse durations have such a short span in time, they can be used to capture processes of a slower duration. An analogy is using a camera snapshot to document the exact moment that a bullet pierces a target. This is only possible because the flash of light from a camera occurs on a shorter timeframe than the event of the bullet hitting the target. Similarly, a fs-long pulse can be used to probe fast dynamics in molecules that occur on the ps timescale, for example.

- High spatial resolution; since the pulses have such a small spatial extent, they can serve to image things that are bigger in size, like a cranial nerve of a mouse [33].

- High bandwidth; a pulse duration is intrinsically connected to its optical bandwidth[1]by the uncertainty principle regarding energy and time. For example, a 100 fs pulse has about a 10 terahertz (THz; 10^{12} Hz) bandwidth, which makes ultrashort pulses useful for communications [34]. For comparison, the continuous wave laser used in the RSP experiment has a bandwidth of less than a MHz.

[1]Bandwidth in this thesis means the range of frequencies contained by the pulse. Differentiating $\omega = \frac{c}{\lambda}$

- Potential for extremely high intensity; for a given pulse energy, the peak power and intensity are inversely proportional to the pulse duration. For example, amplified fs pulses can produce 10^{15} W of peak power [32], which opens up new regimes for study such as laboratory astrophysics [35].

An ultrashort pulse's propensity for high intensity makes it perfect for use in nonlinear optics. As we shall soon see, nonlinear optical effects occur when the polarization density of a medium responds nonlinearly to the incoming electric field, which typically occurs when the incoming light is very intense. Thus, ultrashort pulses are routinely employed to generate nonlinear optical effects.

The experiments in this thesis use nonlinear optical techniques generated by both a continuous wave laser and an ultrafast laser[2]for the generation and characterization of single photons. This chapter introduces relevant concepts, starting with the foundation of classical electromagnetism and optics: Maxwell's equations. Interested readers are encouraged to review Refs. [36] and [32] for more information.

Section 3.1 follows the general treatment of Maxwell's equations to obtain equations that describe nonlinear optics. Section 3.2 discusses the important phenomenon of dispersion in optics. Section 3.3 introduces the general second-order nonlinear effect of three-wave mixing (3WM), and the importance of phase-matching. Section 3.4 introduces the third-order nonlinear optical Kerr effect. Section 3.5 details the concept of characterizing temporal widths of pulses by crosscorrelations and autocorrelations, which is one of the big applications of ultrafast pulses (number one in the bullet-point list!).

3.1 Nonlinear optics

Nonlinear optical effects occur due to the interaction between sufficiently strong laser light[3]and matter, which results in the alteration of the material's nonlinear properties. We start with Maxwell's equations which describe the interactions between the electric field $\mathbf{E}$

with respect to the wavelength λ gives $\Delta\omega = \frac{c}{\lambda^2}\Delta\lambda$, an approximate relationship between a small range of frequencies ω and a small wavelength interval in terms of the speed of light in vacuum c.

[2]A pulsed laser whose pulses are ultrashort.

and magnetic field $\mathbf{H}$ inside a medium [37]:

$$\nabla \cdot \mathbf{D} = \rho_f \tag{3.1}$$

$$\nabla \times \mathbf{E} = -\frac{\partial \mathbf{B}}{\partial t} \tag{3.2}$$

$$\nabla \cdot \mathbf{B} = 0 \tag{3.3}$$

$$\nabla \times \mathbf{H} = \mathbf{J}_f + \frac{\partial \mathbf{D}}{\partial t}. \tag{3.4}$$

Note that bolded quantities are vector fields. ρ_f is the free electric charge density, $\mathbf{J}_f$ is the free current density, and $\mathbf{B}$ is the magnetic flux density (also known as the magnetic induction). $\mathbf{H} = \frac{1}{\mu_0}\mathbf{B} - \mathbf{M}$, where μ_0 is the permeability of free space and $\mathbf{M}$ is the magnetic dipole moment per unit volume. $\mathbf{D} \equiv \epsilon_0 \mathbf{E} + \mathbf{P}$ is the electric displacement, which contains the permittivity of free space, ϵ_0, and the polarization, $\mathbf{P}$, i.e. the dipole moment per unit volume.

Following the usual assumptions in nonlinear optics, we are interested in solutions to these equations in a dielectric material where the material is nonmagnetic ($\mathbf{M} = 0$), and there are no free charges or currents ($\rho_f = 0$, $\mathbf{J}_f = 0$). The magnetic field and magnetic flux density are now proportional: $\mathbf{B} = \mu_0 \mathbf{H}$, and we turn our attention to $\mathbf{D}$. In linear optics, the induced polarization $\mathbf{P}$ depends linearly on the electric field strength $\mathbf{E}$ [36]:

$$\mathbf{P}(t) = \epsilon_0 \chi^{(1)} \mathbf{E}(t), \tag{3.5}$$

where $\chi^{(1)}$ is the linear susceptibility. For simplicity, we assume that the polarization at time t depends only on the instantaneous value of the electric field strength, implying that the medium must also be lossless and dispersionless. This is a reasonable assumption because in transparent material (such as the ones used in the lab), the material response times are estimated to be on the order of ≈ 4 fs [32]. As the electric field intensity changes, the material response is modified in a perturbative manner so we expand the polarization as a power series in the electric field strength[4]:

$$\mathbf{P}(t) = \epsilon_0 [\chi^{(1)}(t)\mathbf{E}(t) + \chi^{(2)}(t)\mathbf{E}^2(t) + \chi^{(3)}(t)\mathbf{E}^3(t) + ...] \tag{3.6}$$

$$\mathbf{P}(t) \equiv \mathbf{P}^{(1)}(t) + \mathbf{P}^{(2)}(t) + \mathbf{P}^{(3)}(t) + ... \tag{3.7}$$

$$\begin{aligned} \mathbf{P}(t) &= \mathbf{P}^{(1)}(t) + \mathbf{P}(t)_{NL} \\ &= \mathbf{P}(t)_L + \mathbf{P}(t)_{NL}, \end{aligned} \tag{3.8}$$

[3] Typically only laser light is intense enough to cause these modifications in matter.

where $\chi^{(2)}$ and $\chi^{(3)}$ are the second- and third-order susceptibilities. The susceptibilities $\chi^{(n)}$ are tensors of rank $n+1$ whose indices determines the strength of the coupling for each frequency and spatial direction. These can be simplified by considering the symmetries of the susceptibility in the material. The indices of the susceptibilities are suppressed for simplicity in writing.

In Eq. 3.8, the linear and nonlinear contributions are separated into $\mathbf{P}(t)_L$ and $\mathbf{P}(t)_{NL}$ respectively. In general, second- and third-order nonlinear optical effects respectively refer to only $\mathbf{P}^{(2)}(t)$ and $\mathbf{P}^{(3)}(t)$ in $\mathbf{P}(t)_{NL}$. This is because in general, the higher-order susceptibility terms are small. In a typical second-order effect, $\chi^{(3)}$ is relatively small and negligible. Third-order effects do have a $\chi^{(2)}$ dependence, but they are normally studied in materials with centrosymmetry[5], which causes $\chi^{(2)}$ to vanish [36].

I proceed to speed-walk through the derivation of the general optical wave equation in nonlinear optics. First, take the curl of Eq. 3.2 and swap the space and time derivatives on the right-hand side of the resulting equation. Then replace $\nabla \times \mathbf{B}$ on the right-hand side with $\mu_0 \frac{\partial \mathbf{D}}{\partial t}$ (our assumptions from earlier, $\mathbf{M} = 0, \mathbf{J}_f = 0$, were applied to Eq. 3.4) to get

$$\nabla \times \nabla \times \mathbf{E} + \mu_0 \frac{\partial^2 \mathbf{D}}{\partial t^2} = 0. \tag{3.9}$$

Eliminate $\mathbf{D}$ from Eq. 3.9 by applying its definition $\mathbf{D} \equiv \epsilon_0 \mathbf{E} + \mathbf{P}$, and use $\mu_0 = \frac{1}{\epsilon_0 c^2}$, and we arrive at the conclusion, the most general wave equation for nonlinear optics:

$$\nabla \times \nabla \times \mathbf{E} + \frac{1}{c^2} \frac{\partial^2}{\partial t^2} \mathbf{E} = -\frac{1}{\epsilon_0 c^2} \frac{\partial^2 \mathbf{P}}{\partial t^2}, \tag{3.10}$$

where $\mathbf{P}$ has been previously given in Eq. 3.7.

Following the usual treatment in nonlinear optics, we apply a vector calculus identity to the first term on left-hand side of Eq. 3.10 to get:

$$\nabla(\nabla \cdot \mathbf{E} - \nabla^2 \mathbf{E}) + \frac{1}{c^2} \frac{\partial^2}{\partial t^2} \mathbf{E} = -\frac{1}{\epsilon_0 c^2} \frac{\partial^2 \mathbf{P}}{\partial t^2}. \tag{3.11}$$

In linear optics, the very first term in Eq. 3.11 disappears because $\nabla \cdot \mathbf{D} = 0$ implies $\nabla \cdot \mathbf{E} = 0$. In nonlinear optics, this term normally remains even for isotropic materials due

[4] If the intensity is past $10^{12} \frac{W}{cm^2}$, we enter the regime of high-intensity physics and this Taylor expansion breaks down.

[5] Centrosymmetric materials have an inversion centre. Simply, this means that for every point at some coordinates (x, y, z) relative to the centre of symmetry, there is another indistinguishable point $(-x, -y, -z)$.

to $\mathbf{D} \equiv \epsilon_0 \mathbf{E} + \mathbf{P}$. The usual treatment is to regard this term as negligible; for certain cases the term vanishes altogether and for others, the contribution is small. The wave equation now can be expressed simply as

$$\nabla^2 \mathbf{E} - \frac{1}{c^2} \frac{\partial^2}{\partial t^2} \mathbf{E} = \frac{1}{\epsilon_0 c^2} \frac{\partial^2}{\partial t^2} \mathbf{P}. \tag{3.12}$$

Now we decompose $\mathbf{P}$ into its linear and nonlinear components as per Eq. 3.8, and do the same for $\mathbf{D} = \epsilon_0 \mathbf{E} + \mathbf{P} = \epsilon_0 \mathbf{E} + \mathbf{P}_L + \mathbf{P}_{NL} = \mathbf{D}_L + \mathbf{P}_{NL}$. We obtain the typical nonlinear optics wave equation:

$$\nabla^2 \mathbf{E} - \frac{1}{\epsilon_0 c^2} \frac{\partial^2 \mathbf{D}_L}{\partial t^2} = \frac{1}{\epsilon_0 c^2} \frac{\partial^2 \mathbf{P}_{NL}}{\partial t^2}. \tag{3.13}$$

It is from this equation that we can obtain coupled-wave equations for incoming and outgoing optical fields. $\mathbf{E}, \mathbf{D}$ and $\mathbf{P}$ must be written as sums of their frequency components ω_i, e.g.:

$$\mathbf{E}(t) = \sum_i \mathbf{E}_i(\omega_i) e^{i(\mathbf{k}_i \cdot \mathbf{r} - \omega_i t)} + \text{c.c.} \tag{3.14}$$

where $\mathbf{k}_i$ is known as the wave vector or momentum vector, and $\mathbf{r}$ contains the spatial coordinates. By using the sums of relevant frequencies in $\mathbf{E}$ and $\mathbf{P}$ and inserting them into Eq. 3.13, one obtains coupled-wave equations with which to study various nonlinear effects at single frequencies.

3.2 Dispersion

Consider a pulse of light propagating in a nonlinear medium. A pulse is a group of frequencies travelling together in a wavepacket (unlike a good continuous wave laser, where one can just assume a single frequency mode). All materials have an index of refraction n which is implicitly a function of frequency ω and direction $\mathbf{k}$, although we will neglect the directionality for simplicity. This means that different frequencies encounter different refractive indices in the same medium, so they travel different speeds. This is referred to as dispersion, or specifically, chromatic dispersion. It is an important consequence in femtosecond lasers because the material lengths are relatively large and the pulses are ultrashort.

The total refractive index $n(\omega)$ is related to the effective susceptibility by the relation: [36]

$$n^2(\omega) = 1 + \chi_{eff}. \tag{3.15}$$

The linear refractive index[6]is $n_L(\omega) = \sqrt{1+\chi^{(1)}(\omega)}$, where the effective susceptibility is simply the linear susceptibility. The phase velocity v_p of any one frequency component ω is

$$v_p = \frac{\omega}{k}, \tag{3.16}$$

where $k = \frac{2\pi}{\lambda}$ is the wavenumber (the scalar of $\mathbf{k}$ in a given direction) and λ is the wavelength corresponding to the frequency ω, related by $c = \omega\lambda$. By using the more familiar relation $n_L = \frac{c}{v_p}$ where c and v are, respectively, the speeds of light in vacuum and in the medium, we can write k as a function of ω:

$$k = \frac{\omega n_L}{c}. \tag{3.17}$$

Mathematically, dispersion can be treated by considering the ω dependence in k. Applying a Taylor expansion around the centre frequency ω_0, $k(\omega)$ becomes [32]:

$$k(\omega) = k(\omega) + \frac{\partial k}{\partial \omega}(\omega-\omega_0) + \frac{\partial^2 k}{\partial \omega^2}\frac{(\omega-\omega_0)^2}{2!} + ... \tag{3.18}$$

$$= k(\omega) + k_1(\omega-\omega_0) + \frac{k_2}{2!}(\omega-\omega_0)^2 + ... \tag{3.19}$$

The zeroth order term in Eq. 3.19 describes a phase shift. The first order term contains the inverse group velocity, v_g^{-1}, and describes an overall time delay which doesn't change the pulse shape. The group velocity is:

$$v_g = \frac{\mathrm{d}\omega}{\mathrm{d}k} \tag{3.20}$$

and it governs the speed at which the wavepacket moves as a whole. The higher-order terms in Eq. 3.19 represent the group delay dispersion or group velocity dispersion (GVD), although in this thesis we limit it to the quadratic term. It contributes a quadratic spectral phase change and leads to a linear variation in frequency delay. Physically we can think about the pulse being 'backlogged' and being stretched out in time resulting in temporal broadening. The bluer wavelengths travel slower (faster) than the redder components resulting in positive (negative) chirp which is what we term normal (anomalous) dispersion. In this thesis, a grating compressor is used to apply negative chirp to pulses that gain positive chirp from travelling in fibre, resulting in an approximately net zero dispersion.

[6]This is typically denoted n in literature, but in this thesis a distinction is made because we will see later in Section 3.4 that the nonlinear refractive index comes into play.

Eq. 3.20 is helpful for computing the temporal dispersion between two pulses of different central frequencies which is termed temporal walk-off (the spatial equivalent is called spatial walk-off: we will see this below in Section 3.3). Temporal walk-off is the difference in time between the two pulses travelling in the medium:

$$\Delta t = (\frac{L}{v_{g1}} - \frac{L}{v_{g2}}) \tag{3.21}$$

$$= L(\frac{n_{g1}}{c} - \frac{n_{g2}}{c})$$

$$= \frac{L}{c}(n_{g1} - n_{g2}), \tag{3.22}$$

where length of the medium is given by L, and the group indices are given by $n_g = \frac{c}{v_g}$. c is the speed of light in vacuum.

3.3 Phase matching in three-wave mixing

I turn the discussion to 3WM and note that the physics mentioned below is the same for the notions of pulsed and continuous wave light. As the name implies, it is a second-order nonlinear effect which involves three optical fields. It can only occur in $\chi^{(2)}$ materials such as BBO and BiBO crystals, both of which are used in this thesis. Common phenomena are:

- Second harmonic generation (SHG), where two input equal fields of low-frequency drive a higher output frequency: $\omega_1 + \omega_1 = \omega_2$,
- Sum-frequency generation (SFG), where two different input fields of low frequency drive a higher output frequency: $\omega_1 + \omega_2 = \omega_3$,
- Difference-frequency generation (DFG), where two input fields drive an output difference frequency: $\omega_1 - \omega_2 = \omega_3$,
- Spontaneous parametric down-conversion (SPDC), where an input field spontaneously generates two output fields. Previously in Sections 2.6 and 2.7 we saw that the two output fields were degenerate, but non-degenerate fields are possible as well: $\omega_1 = \omega_2 + \omega_3$.

It is tempting to think of 3WM as a single event in which only 3 photons of single frequencies are involved. For example, SPDC can be (and is often) depicted in Fig. 3.1 for

a single pump photon of higher energy ω_p converting into two photons with frequencies ω_p and ω_i. Fig 3.1(b) is the corresponding energy diagram.

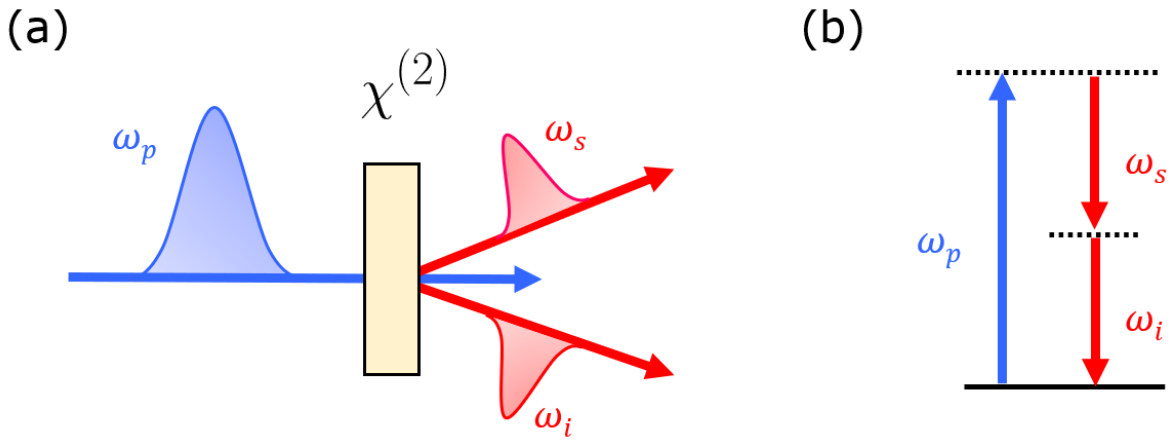

Figure 3.1: SPDC where one pump photon with frequency ω_p down-converts into the signal and idler, with respective frequencies ω_p and ω_i. (a) is a side-view of a diagrammatic representation of the process while (b) is the energy diagram of the process showing $\omega_p = \omega_p + \omega_i$. Since $\omega_p = \omega_i$, this is degenerate SPDC.

These images are not inaccurate but they do not tell the whole story. In the lab, it is a beam of light which interacts with the $\chi^{(2)}$ crystal of some length L. In a single moment in time during SPDC, many photons are being down-converted and creating two outgoing photons each at all parts of the crystal. This results in the outgoing waves having relative phases and, more often than not, they destructively interfere causing less outgoing light. This brings us to the idea of phase-matching.

The phase-matching function is related to a crystal's nonlinearity profile via the Fourier transform and is defined [38, 39, 40]:

$$\Phi_{PMF} = \frac{1}{L}\int_{-\infty}^{+\infty} \chi(z) e^{i\Delta \mathbf{k} z} \mathrm{d}z \tag{3.23}$$

where L is the crystal length, $\chi(z)$ encapsulates the nonlinear optical coupling, and $\Delta\mathbf{k}$ is termed the phase mismatch. For simplicity, we can assume that the nonlinear susceptibility is independent of z, though this assumption cannot be applied to periodically-poled materials and will be addressed later in this section. To find the output spectral waveform,

we can integrate along the crystal length:

$$\Phi_{PMF}(\Delta\mathbf{k}) = \frac{1}{L}\int_0^L \chi(z)e^{i\Delta\mathbf{k}z}\mathrm{d}z,$$
$$\propto \exp(\frac{i\Delta\mathbf{k}L}{2})\mathrm{sinc}(\frac{\Delta\mathbf{k}L}{2}). \tag{3.24}$$

To maximize Eq. 3.24, $\Delta\mathbf{k} = 0$. This equation is known as the phase-matching condition. Now considering the conservation of momentum:

$$\mathbf{k}_p = \mathbf{k}_s + \mathbf{k}_i \tag{3.25}$$
$$\Delta\mathbf{k} = 0 = \mathbf{k}_p - \mathbf{k}_s - \mathbf{k}_i. \tag{3.26}$$

From Eq. 3.26, we see that meeting the phase-matching condition means that the signal and idler photons are always created in phase with the pump. This allows for the maximum efficiency with which to build up the outgoing light intensity. Similar phase-matching equations to Eq. 3.25 can be built for other nonlinear processes, including different kinds of 3WM.

Meeting the phase-matching condition is not trivial, since the wavelengths involved are normally quite disparate (in the RSP experiment, for example, 404 nm photons down-convert into two 808 nm photons each) and spatial walk-off comes into play. There are three main techniques used to meet the phase-matching condition. The first is by quasi-phase-matching, also known as periodic poling, which modulates the nonlinear coefficient so that some of the phase mismatch is reversed periodically. This fabrication technique is performed by inverting birefringent layers, termed domains, in the crystal over a specific length, termed the poling period. Each flip causes a phase shift of π and its nonlinearity profile is now a discontinuous function which only takes on values of $\pm\chi_0$ and can be modelled as a square wave in the $\hat{z}$ direction. The phase-matching function for the entire crystal is now a linear superposition of phase-matching functions for all the individual domains [38]:

$$\Phi_{QPMF}(\Delta\mathbf{k}) \propto \frac{\chi_0}{L}\sum_{n=1}^{N} s_n \int_0^L \mathrm{rect}(\frac{z-z_n}{l_c})e^{i\Delta\mathbf{k}z}\mathrm{d}z,$$
$$\propto \frac{\chi_0 l_c}{L}\mathrm{sinc}(\frac{\Delta\mathbf{k}l_c}{2})\sum_{n=1}^{N} s_n \exp(i\Delta\mathbf{k}z_n). \tag{3.27}$$

s_n is a term which accounts for the phase shift caused by a domain, $z_n = (n - \frac{1}{2})l_c$ is the $\hat{z}$-coordinate of the beginning of the nth domain, and l_c is the length of each domain.

Since a periodically-poled crystal consists of domains which cause a phase change of π, $s_n = e^{in\pi} = (-1)^n$. By inserting s_n into Eq. 3.27, and noting that constructive interference occurs near $\Delta k = \frac{2\pi}{\Lambda}$, where $\Lambda = 2l_c$ is the poling period, we retrieve a new phase-matching function:

$$\Phi_{QPMF}(\Delta\mathbf{k}) \propto \mathrm{sinc}\Big(\frac{(\Delta\mathbf{k} - \frac{2\pi}{\Lambda})L}{2}\Big). \tag{3.28}$$

Eq. 3.28 is maximized when $\Delta\mathbf{k} = \frac{2\pi}{\Lambda}$. Now by considering the conservation of momentum again, the quasi-phase-matching condition for SHG in a periodically-poled material is:

$$\Delta\mathbf{k} = \frac{2\pi}{\Lambda} = \mathbf{k}_p - \mathbf{k}_s - \mathbf{k}_i. \tag{3.29}$$

A manufacturer would tune the poling period Λ to meet the phase-matching condition. Similarly to Eqs. 3.25 and 3.26, other quasi-phase-matching conditions can be built for other nonlinear processes. This technique is outlined more fully in Refs. [38, 41].

The second method used to help meet the phase-matching condition is by temperature tuning. The refractive index (and by extension, $\mathbf{k}$) is temperature-dependent, but note that temperature changes do not make large changes to the phase-matching. The third method is by angle tuning in birefringent media, where the effective index of the extraordinary axis is tuned by changing the relative angle between the crystal face to the propagation of the light, denoted as θ below. For some crystals, it allows for two different wavelengths to follow two different refractive indices, allowing them to travel a similar path for a short while.

For example, in the case of uniaxial birefringence (e.g. BBO), the ordinary wave (whose polarization is along the ordinary axis) follows Eq. 3.17, $k = \frac{\omega n_o}{c}$. The extraordinary wave also follows the same equation except $k = \frac{\omega n_e}{c}$ and n_e is a function of the angle θ where [32]

$$\frac{1}{n_e^2(\theta)} = \frac{\cos^2(\theta)}{n_o^2} + \frac{\sin^2(\theta)}{n_e^2}. \tag{3.30}$$

The effective refractive index for the extraordinary wave varies smoothly between n_o ($\theta = 0$) and n_e ($\theta = 90°$). A major disadvantage of angle tuning is that the incoming field and the extraordinary field quickly diverge from each other and spatial walk-off is caused, resulting in reduced efficiency. Most angle-tuned crystals have a short length to help mitigate this.

In this thesis, we exploit all three phase-matching techniques. In the RSP experiment, we use a periodically-poled potassium titanyl phosphate crystal which is kept in an oven. In the switching experiment, we angle-tune BiBO crystals for SHG and SPDC in the entangled single photon source.

3.4 Optical Kerr effect

The optical Kerr effect is a third-order nonlinear effect. Put simply, it is the change of the refractive index of a medium due to a strong electric field, causing an intensity-dependent refractive index. It is also known as the AC Kerr effect, in contrast to the DC Kerr effect, whose refractive index change is due to a slowly varying electric field (e.g. an applied voltage by electrodes across the $\chi^{(3)}$ medium). As previously mentioned in Section 3.1, many third-order effects are studied in centrosymmetry, rendering the second-order susceptibility $\chi^{(2)}$ zero [36]. We keep this assumption and reduce Eq. 3.6. The nonlinear polarization is thus $\mathbf{P}(t)_{NL} = \epsilon_0 \chi^{(3)}(t)\mathbf{E}^3(t)$, where we let the incoming optical field be represented by $\mathbf{E}(t) = \mathbf{E}(\omega)e^{i\omega t} + \text{c.c.}$ The total polarization is

$$\mathbf{P}(t) = \epsilon_0 \chi^{(1)}(t)\mathbf{E}(t) + \chi^{(3)}(t)\mathbf{E}^3(t). \tag{3.31}$$

By substituting Eq. 3.14 into the nonlinear polarization term and taking its Fourier transform, we obtain

$$\mathbf{P}_{NL}(\omega) = \epsilon_0 \chi^{(3)}(\omega; \omega_i, \omega_j, \omega_k)\mathbf{E}(\omega_i)\mathbf{E}(\omega_j)\mathbf{E}(\omega_k). \tag{3.32}$$

Eq. 3.32 is the most general description of a third-order nonlinear process (in a centrosymmetric medium): $\omega = \omega_i + \omega_j + \omega_k$, where the frequencies may be negatives of each other, equal to each other, or even zero in some effects.

There are two ways of measuring the change in refractive index caused by the optical Kerr effect. When the strong field is used to modulate a weaker electric field, this is known as cross-phase modulation (XPM). When the strong electric field changes its own modulation, this is known as self-phase modulation (SPM). In both XPM and SPM, the modulation comes from the strong field exerting a change in the medium's refractive index. However, in this thesis, we are interested only in XPM.

XPM is described by $\omega_w = \omega_w + \omega_p - \omega_p$ and Eq. 3.32 becomes

$$\mathbf{P}_{NL}(\omega_w) = 6\epsilon_0 \chi^{(3)}(\omega_w; \omega_w, \omega_p, -\omega_p)|\mathbf{E}(\omega_p)|^2\mathbf{E}(\omega_w), \tag{3.33}$$

where ω_p is the strong pump field and ω_w is the weak wave.

Eq. 3.33 is substituted into the Fourier transform of Eq. 3.32:

$$\begin{aligned} \mathbf{P}(\omega_w) &= \epsilon_0 \chi^{(1)}(t)\mathbf{E}(\omega_w) + 6\epsilon_0 \chi^{(3)}|\mathbf{E}(\omega_p)|^2\mathbf{E}(\omega_w). \\ \mathbf{P}(\omega_w) &= \epsilon_0 \chi_{eff}\mathbf{E}(\omega_w), \end{aligned} \tag{3.34}$$

where by grouping up the terms we have an effective susceptibility $\chi_{eff} = \chi^{(1)} + 6\chi^{(3)}|\mathbf{E}(\omega_p)|^2$.

We would like an equation for the intensity-dependent refractive index. Recall Eq. 3.15 which relates the total refractive index n to χ_{eff}, which in this case becomes:

$$n = \sqrt{1 + \chi^{(1)} + 6\chi^{(3)}|\mathbf{E}(\omega_p)|^2}. \tag{3.35}$$

The total refractive index n can also be written as [36, 32]:

$$n = n_L + \bar{n}_{NL}\langle \mathbf{E}^2(t)\rangle \tag{3.36}$$

where it is composed of the linear refractive index, and $\bar{n}_{NL}$ is another optical constant, sometimes called the second-order refractive index, multiplied by the time-averaged intensity of the incoming optical field. Since we let $\mathbf{E}(t) = \mathbf{E}(\omega)e^{i\omega t} + \text{c.c}$, then $\langle \mathbf{E}^2\rangle = 2|\mathbf{E}(\omega)|^2$. Eq. 3.36 becomes

$$n = n_L + 2\bar{n}_{NL}|\mathbf{E}(\omega_p)|^2 \tag{3.37}$$

We can compare Eqs. 3.35 and 3.37 to get a relation between the linear and the second-order refractive indices:

$$n^2 = 1 + \chi_{eff} \tag{3.38}$$

$$\left(n_L + 2\bar{n}_{NL}|\mathbf{E}(\omega_p)|^2\right)^2 = 1 + \chi^{(1)} + 6\chi^{(3)}|\mathbf{E}(\omega_p)|^2 \tag{3.39}$$

$$n_L^2 + 4n_L\bar{n}_{NL}|\mathbf{E}(\omega_p)|^2 + 4\bar{n}_{NL}^2|\mathbf{E}(\omega_p)|^4 = n_L^2 + 6\chi^{(3)}|\mathbf{E}(\omega_p)|^2 \tag{3.40}$$

$$4n_L\bar{n}_{NL}|\mathbf{E}(\omega_p)|^2 = n_L^2 + 6\chi^{(3)}|\mathbf{E}(\omega_p)|^2 - n_L^2. \tag{3.41}$$

$$\bar{n}_{NL} = \frac{3\chi^{(3)}}{2n_L}. \tag{3.42}$$

Note that from Eq. 3.40 to Eq 3.41, the $|\mathbf{E}(\omega_p)|^4$ term was dropped. This is a valid approximation for many materials since $\bar{n}_{NL}^2$ is negligibly small. Replacing Eq. 3.42 in Eq. 3.37 gives the explicit intensity-dependent refractive index as

$$n = n_L + \frac{3\chi^{(3)}}{n_L}|\mathbf{E}(\omega_p)|^2. \tag{3.43}$$

The more common way of expressing the intensity-dependent refractive index is

$$n = n_L + n_{NL}I, \tag{3.44}$$

where $I = 2n_L\epsilon_0 c|\mathbf{E}(\omega_p)|^2$ is the time-averaged intensity of the strong optical wave. Eqs. 3.44 and 3.37 have to be equal, so by substituting one into the other, the relation between the two nonlinear coefficients is

$$n_{NL} = \frac{\bar{n}_{NL}}{n_L\epsilon_0 c}. \tag{3.45}$$

Inserting Eq. 3.42 into Eq. 3.45 gets us the relation between n_{NL} and $\chi^{(3)}$:

$$n_{NL} = \frac{3\chi^{(3)}}{2n_L^2\epsilon_0 c}. \tag{3.46}$$

Replacing the equation for n_{n_L} (Eq. 3.46) into the more common intensity-dependent refractive index equation (Eq. 3.44) retrieves Eq. 3.43, so the preference of using either $\bar{n}_{NL}$ or n_{NL} is up to the scientist. As a quick reminder, n is a function of the momentum vector $\mathbf{k}$, so the change of refractive index is only along the direction of the strong electric field and this is what Eq. 3.43 describes. Using Eq. 2.4, the birefringence is given by:

$$\begin{aligned}\Delta n &= |n_o - n_e| \\ &= |n_L - n| \\ &= \frac{3\chi^{(3)}}{n_L}|\mathbf{E}(\omega)|^2.\end{aligned} \tag{3.47}$$

The optical Kerr effect underlies the optical Kerr switch in the switching experiment.

3.5 Characterizing temporal widths

In the beginning of this chapter, high timing resolution was mentioned as one of the big applications of ultrashort pulses. This section is all about measuring the temporal width of a pulse. First, how do you characterize a pulse? Let's simplify Eq. 3.14 for an electric field in time which is linearly polarized:

$$E(t) = \frac{1}{2}\sqrt{I(t)}e^{i(\phi(t)-\omega t)} + \text{c.c.}, \tag{3.48}$$

where $I(t)$ and $\phi(t)$ are the time-dependent intensity and phase of the pulse and ω is the frequency. We can take the Fourier transform of the time-domain to receive its spectral-domain equivalent, where the electric field is similarly described by an intensity and phase, though we shall now refer to these specifically as the spectrum $I(\omega)$ and spectral phase

$\phi(\omega)$. To know everything about a pulse means knowing both its intensity and phase in either the temporal or spectral domain, since the other can be obtained via the Fourier transform.

I restrict our discussion to only measurements of intensity, which is the easier of the two to obtain but nonetheless independently reveals essential information. One such information is the pulse's temporal width. As long as a detector's temporal resolution is shorter than the pulse, a temporal waveform can be reconstructed (time on the $\hat{x}$-axis and intensity is on the $\hat{y}$-axis). A common way of describing a pulse width is by the full-width half-maximum (FWHM), calculated by taking the difference between the two time values at the halved intensity value, and then multiplied by a compensation value depending on its shape (e.g. Gaussian, sech^2). I note that instead of the FWHM, some researchers prefer to use the standard deviation of the distribution. In any case, the spectral width is obtained similarly to the temporal width and is straightforward if using a spectrometer.

The problem with ultrashort pulses is that the temporal resolution of many detectors is on the order of nanoseconds and is inherently limited by the electronic speed in the working mechanism. In general, measuring ultrashort pulses involves interferometric and nonlinear effects, which rely on the timescales of the optical processes involved and the pulses themselves. I will now detail nonlinear auto-correlation and cross-correlation which indeed are intensity measurements only and thus suffices to determine (or at least, make a good estimate of) an ultrashort pulse's temporal width. Nonlinear cross-correlation is a type of ultrafast optical gating. A pulse of interest is mapped by a nonlinear interaction with a known reference pulse in a nonlinear medium with some time delay τ, normally implemented with a delay line (e.g. retroreflector on a motor). I use the example of SFG, shown in Fig. 3.2. The reference or gate pulse and the measured or signal pulse have temporal fields $E_g(t)$ and $E_s(t)$ (following the form of Eq. 3.48).

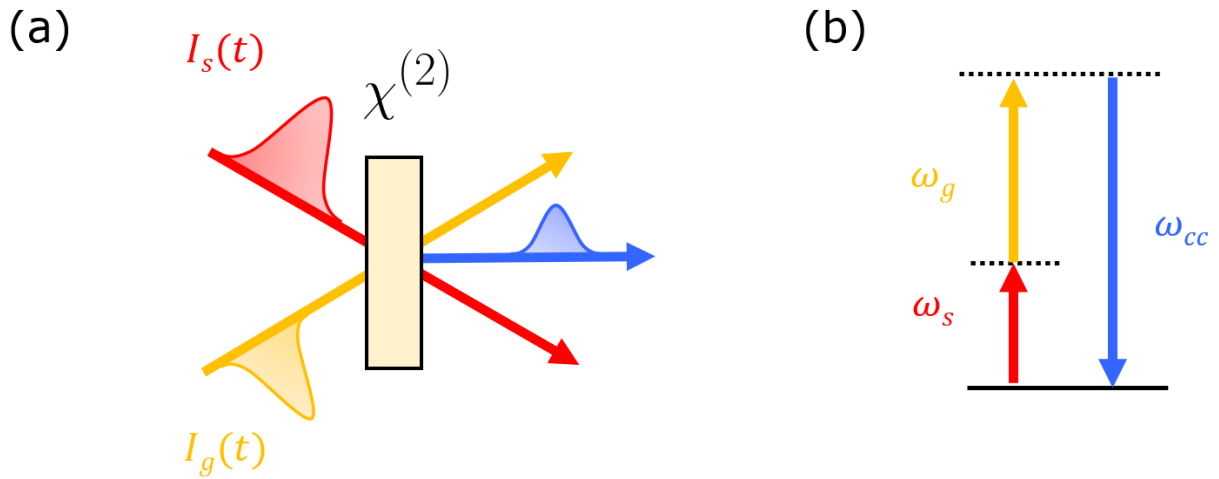

Figure 3.2: SFG where two input fields of low frequencies, where $I_s(t)$ is centred at ω_g and $I_g(t)$ is centred at ω_p, create a higher output frequency field centred at ω_{cc}. In the case that the two input fields are identical, it is termed SHG. (a) is a side-view of a diagrammatic representation of the process while (b) is the energy diagram of the process showing $\omega_g + \omega_p = \omega_{cc}$.

Overlapping the two pulses generates different sum-frequency intensities in time, each which can be measured with a slow detector (e.g. power meter). The time-integrated power of the upconverted signal at each time delay is proportional to the intensity cross-correlation, $I_{cc}(t)$ [42]:

$$I_{cc}(\tau) \propto \int_{\infty}^{\infty} I_s(t) I_g(t-\tau) \mathrm{d}t. \tag{3.49}$$

All second-order effects follow this general form. Ideally, $I_g(t)$ should be a delta function $\delta_g(t)$ and then Eq. 3.49 would yield $I_s(t)$ exactly, but realistically the gate pulse is of a finite width which makes the measured cross-correlation broader. For example, if the pulses are well-described Gaussians with temporal widths of Δ_g and Δ_s, then

$$E_g(t) = \exp\left[\frac{-t^2}{4\Delta_g^2}\right], \qquad E_s(t) = \exp\left[\frac{-t^2}{4\Delta_s^2}\right]$$

$$I_s(\tau) = \exp\left[\frac{-t^2}{2\Delta_s^2}\right] \tag{3.50}$$

$$I_{cc}(\tau) \propto \exp\left[\frac{-\tau^2}{2(\Delta_g^2 + \Delta_s^2)}\right]. \tag{3.51}$$

The broadened temporal width measured by the cross-correlation in Eq. 3.51 is: $\Delta\tau = \sqrt{\Delta t_s^2 + \Delta t_g^2}$, in the standard deviation definition. Note that the FWHM is related to the standard deviation by the relation:

$$\text{FWHM}(\tau) = 2\sqrt{2\ln(2)}\Delta\tau. \tag{3.52}$$

If a reference pulse is unavailable, experimentalists will use the same pulse for the signal and gate. In this case, $I_g(t) = I_s(t)$, and Eq. 3.49 is now an intensity autocorrelation. The broadening in this scenario is well-known for different functional forms. The deconvolution factor for the FWHM is respectively $\sqrt{2}$ and 1.54 for Gaussian- and sech^2-shaped pulses [42]. Note that the resulting measurement is necessarily symmetric and it is not unique. An autocorrelation measurement could correspond to two pulses of different intensities. A higher-order autocorrelation removes symmetry, but is also not unique [42]. This is because third-order effects generate a signal intensity which is proportional to three factors of intensities due to having three involved fields, which breaks the ambiguity.

Let's take the example of the Kerr effect. Say our ultrafast pump pulse, $E_g(t)$, has enough intensity to cause a birefringence (obeying Eq. 3.47) in the Kerr medium, which causes it to act like a waveplate. We can set up the Kerr medium in between crossed polarizers so that if the signal pulse, $E_s(t)$, is $|H\rangle$, then it rotates to $|V\rangle$ whenever the gate pulse is present and causing local birefringence. As above, we add a delay τ between the gate and the signal and let our detector collect only $|V\rangle$ light. The third-order cross-correlation is

$$I(t) \propto \int_{-\infty}^{\infty} I_g(t) I_g(t-\tau) I_s(t-\tau) \mathrm{d}t. \tag{3.53}$$

Similar to the second-order case, a third-order autocorrelation will use the same pulse for both signal and gate and produce $I(t) \propto I_g(t) I_g^2(t-\tau)$.

For interest: popular, fully-characterizing techniques in ultrashort pulse reconstruction are spectral phase interferometry for direct electric-field reconstruction (SPIDER) [43, 44] and frequency-resolved optical gating (FROG) [45, 42]. The nonlinear cross-correlation and autocorrelation techniques explained above are used in FROG. In both, algorithms are required to reconstruct the intensity and phase.

The switching experiment performs an autocorrelation with SFG to obtain the temporal width of the gate pulse, and it also involves using the Kerr effect to perform a cross-correlation with the gate pulse and signal pulse. This will be discussed in greater detail in Chapter 5.

Chapter 4

Remote state preparation of spin-orbit lattices

Notes and acknowledgments

The contents of this chapter has been submitted to *Physical Review Letters* and is available as an ArXiv preprint [46].

Author contributions

The study was conceived through many discussions but especially by **Dusan Sarenac**, **Dmitry Pushin**, **Kevin Resch** and **Thomas Jennewein**.
Michael Grabowecky helped with experimental considerations.
Connor Kapahi helped with post-processing considerations.
Sacha Schwarz ran a previous version of the experiment.
Andrew Cameron and **Sandra Cheng** re-aligned and simulated the final version of the experiment before carrying it out and analyzing the data.
Andrew Cameron wrote the first draft of the manuscript.
All authors contributed to the final draft of the submitted manuscript.

4.1 Motivation and chapter overview

In the RSP experiment, an optical lattice of spin-orbit states is remotely prepared with polarization-entangled photon pairs. We verify the successful remote preparation by measuring the spatially-dependent correlation rates using an electron-multiplying intensified CCD (emICCD) camera, and performing pixel-wise quantum state tomography.

The story first starts with structured matter-waves. Structured or hyperentangled states are words describing hybrid entanglement, whereby two or more DoFs are entangled. Structured electrons [47, 48] and neutrons [49, 50] are of particular interest in the field of quantum optics and quantum information due to the combination of high dimensionality provided by the orbital angular momentum (OAM) DoF, and high robustness provided by the polarization DoF. Further work has led to a lattice of spin-orbit[1]neutron states [51]. By virtue of the system agnosticism of the quantum information formalism, we can move from neutrons to photons and produce an optical lattice of spin-orbit states. Previously, these lattices have been used in experiments involving the optical Talbot effect [52, 53], optical lattice shaping [54, 55], and the direct detection of optical spin-orbit states by the human eye [56, 57].

This RSP experiment extends the study of optical lattices of spin-orbit states further into photonics, allowing quantum correlations and other capabilities to be explored, such as multi-particle entanglement. The periodicity of optical structured lattices could be useful for quantum sensing [58, 59, 60] and control [61, 62]. The aforementioned advantages of high dimensionality and robustness also make optical structured lattices attractive to quantum communications research [63, 64, 65, 66, 67].

High dimensionality, which can be provided easily by the OAM DoF, is coveted by quantum information researchers due to its enhanced information carrying capacity. OAM modes (beams with different l values) are orthogonal to each other. This orthogonality allows simultaneous multiplexing, demultiplexing, and spatial co-propagation, and all with limited crosstalk. More information regarding OAM communications can be found in Refs. [68, 69]. On the other hand, polarization is the most widely applied DoF in quantum information processing [12]. There are many established and readily accessible methods for manipulating polarization, some of which has been introduced in chapter 2. Combining both DoFs allows us to use the advantages of both. Ref. [70] has specific uses of hyperentanglement in research.

Section 4.2 goes through the concepts needed to understand the RSP experiment. The

[1]This term is used for a specific structured state whose entanglement is between the spin and OAM DoFs.

subsections include: the entangled-photon source (4.2.1); how the RSP works (4.2.2); the LOV prisms by which we use to couple polarization and OAM (4.2.3); the emICCD which is the detector we use to collect our data (4.2.4); and an overview of quantum state tomography, which is how we reconstruct our states (4.2.5). Section 4.3 and Section 4.4 goes through the experimental setup and results, and Section 4.5 concludes the experiment.

4.2 Theory and concepts

4.2.1 Sagnac source

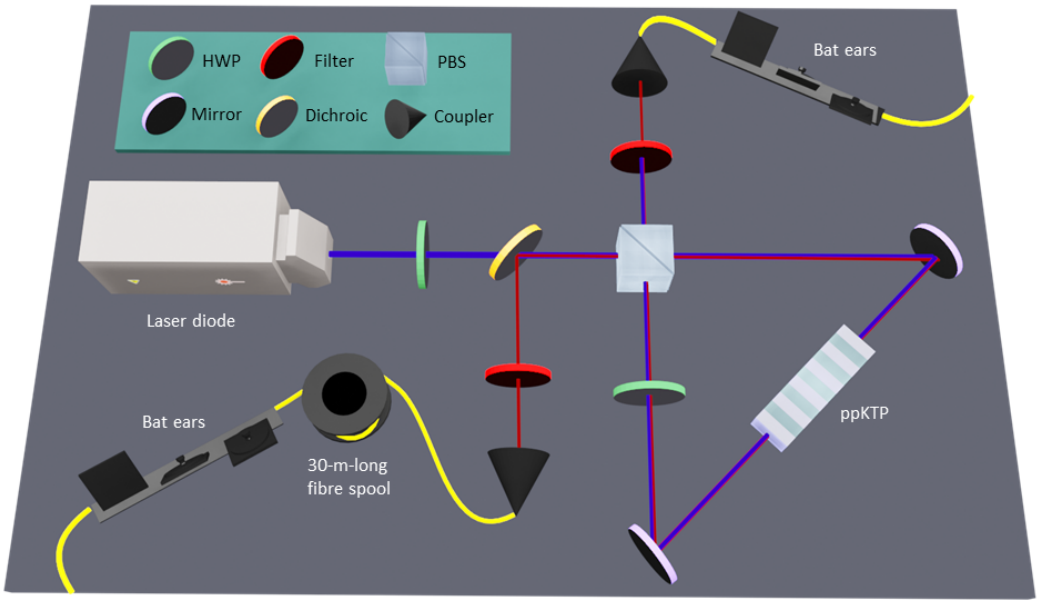

Figure 4.1: The Sagnac source which generates the polarization-entangled photon pairs used in the RSP experiment.

The entangled single photon source in the RSP experiment, as depicted in Fig. 4.1, utilizes an interferometer in a Sagnac configuration where two counter-propagating paths travel in a closed loop. Interference occurs upon the recombination of the two optical paths. In the Sagnac source, the closed loop encompasses the two mirrors and the nonlinear

crystal. The Toptica iWave laser used in the Sagnac source is a continuous wave laser diode centred at 404 nm. An initial HWP sets the polarization of the incoming light. The 404 nm blue light passes through a dichroic mirror which transmits blue light and reflects red, which is split on a PBS. By configuring the second HWP so that $\hat{U}_{HWP}(45°)\,|V\rangle = |H\rangle$, two indistinguishable paths are created. Both pump a 10-mm-long periodically-poled potassium titanyl phosphate crystal (ppKTP). It is kept at 75°c to accomplish phase-matching conditions. Type-II SPDC occurs in the ppKTP and one blue photon down-converts into twin photons at 808 nm with the orthogonal polarizations of $|H\rangle$ and $|V\rangle$.

In the source, incoming $|H\rangle$ light traverses clockwise around the ppKTP as shown in Fig. 4.1. SPDC creates a horizontally polarized signal photon, $|H_s\rangle$, and one vertically polarized idler photon, $|V_i\rangle$. Both of them pass through the HWP and their polarizations are rotated, resulting in $|V_s\rangle$ and $|H_i\rangle$. $|V_s\rangle$ is reflected by both the PBS and the dichroic mirror to pass through the bottom coupler. $|H_i\rangle$ transmits through to the top coupler.

Similarly, incoming $|V\rangle$ light traverses counterclockwise around the ppKTP, and is rotated to $|H\rangle$ by the HWP. SPDC creates $|H_s\rangle$ and $|V_i\rangle$. $|H_s\rangle$ transmits through the PBS and is reflected by the dichroic mirror into the bottom coupler, while $|V_i\rangle$ is reflected into the top coupler.

By choosing to set the polarization of the initial HWP to be $|D\rangle$, then both $|H\rangle$ and $|V\rangle$ paths are taken. The state produced by the Sagnac source is:

$$|\psi\rangle = |H_i\rangle|V_s\rangle + e^{i\phi}|V_i\rangle|H_s\rangle, \tag{4.1}$$

where the relative phase between both arms of the coupler, ϕ, is set by changing the phase in one arm. We could do this in many ways like adjusting the polarization via bat ears, but we do so by using a tilted quarter (not shown in Fig 4.1) just before the bottom coupler[2]. By changing ϕ, two of the four Bell states, $|\Psi^+\rangle$ and $|\Psi^-\rangle$, can be attained. The other two Bell states, $|\Phi^+\rangle$ and $|\Phi^-\rangle$, can be achieved by adjusting the bat ears to give the desired quantum correlations. In the RSP experiment, we let Eq. 4.1 take the form of the $|\Phi^+\rangle$ state.

Lydia Vermeyden's thesis [71] is the unofficial QOQI authority on the Sagnac source. The authority refers to Deny Hamel's thesis [72] for detailed instructions on setting the Bell state using correlations, since he was the original designer of the source.

[2]Simply for experimental convenience. Splitting this work up into two optics makes the correlations easier to obtain.

4.2.2 Remote state preparation

In a RSP protocol, a known state is transmitted from a sender ("Alice") to a receiver ("Bob") using LOCC and prior entanglement of the state. In our experiment, only the high-entanglement limit is relevant since our state is maximally entangled, so the content in this subsection only pertains to this regime. The RSP protocol is fully outlined in all cases in Ref. [73].

The simplest case of RSP is when Alice transmits an equatorial state to Bob. Assume that Alice and Bob share a pair of qubits (a pair of entangled photons in our case) which represent the Bell state

$$|\Psi^-\rangle = \frac{1}{\sqrt{2}}\left(|HV\rangle - |VH\rangle\right). \tag{4.2}$$

To remotely prepare some equatorial state $|\psi\rangle = |H\rangle + e^{i\phi}|V\rangle$, Alice takes her qubit and performs a local operation by measuring in some basis $\{\psi, \psi^\perp\}$, where $\psi^\perp$ is the orthogonal state to ψ, such as $\{|H\rangle, |V\rangle\}, \{|A\rangle, |D\rangle\}$ or $\{|R\rangle, |L\rangle\}$. If Alice measures and sees the outcome $\psi^\perp$, she knows that Bob has the desired state ψ. Alternatively, if Alice's outcome is ψ, then Bob has the orthogonal state $\psi^\perp$. In this instance, Alice classically communicates with Bob, who applies $\hat{\sigma}_z$ to his measurement, which rotates $\psi^\perp$ by 180° on the Bloch sphere to the desired state ψ. This corrective transformation only works for equatorial states.

In our experiment, the Bell state used is

$$\begin{aligned} |\Phi^+\rangle &= \frac{1}{\sqrt{2}}\left(|LR\rangle + |RL\rangle\right) \\ &= \frac{1}{\sqrt{2}}\left(|HH\rangle + |VV\rangle\right) \\ &= \frac{1}{\sqrt{2}}\left(|DD\rangle + |AA\rangle\right). \end{aligned} \tag{4.3}$$

Due to the nature of this state, corrective transformation is not required. To project the $|H\rangle$, $|V\rangle$, $|A\rangle$, $|D\rangle$, $|R\rangle$ and $|L\rangle$ states on the signal photon, we respectively measure $|H\rangle$, $|V\rangle$, $|A\rangle$, $|D\rangle$, $|L\rangle$ and $|R\rangle$ on the idler photon.

4.2.3 Lattice of Optical Vortices prisms

Recent works, such as Ref. [74], exploited the close operational relationship between systems involving neutrons, and photonic systems. The following derivation is described in

more detail in Refs. [74, 75]. Similarly to how a neutron's spin can be manipulated by magnetic field gradients, a photon's polarization can be controlled by birefringence gradients. We start with the coupling operator that describes the effect of a quadrupole magnetic field gradient on a neutron's spin, and allow a birefringent gradient to follow exactly the same form:

$$\hat{U} = e^{i\frac{\pi r}{d}[\cos(\phi)\hat{\sigma_x}+\sin(\phi)\hat{\sigma_z}]}. \tag{4.4}$$

Cylindrical coordinates are used in Eq. 4.4 where the neutron is travelling parallel to the $\hat{z}-$axis, r, ϕ are the polar coordinates, and d is the distance the light has to travel to perform a full rotation on the Bloch sphere. After applying the Suzuki-Trotter expansion to Eq. 4.4 and swapping to Cartesian coordinates so that $x = r\cos(\phi)$ and $y = r\sin(\phi)$, the coupling operator becomes:

$$e^{i(\frac{\pi}{d})(x\hat{\sigma}_x+y\hat{\sigma_z})} = \lim_{N\to\infty}(e^{i(\frac{\pi}{d})\frac{x\hat{\sigma}_x}{N}}e^{i(\frac{\pi}{d})\frac{y\hat{\sigma}_z}{N}})^N. \tag{4.5}$$

By considering the truncation of the right-hand side of Eq 4.5, the equation may be interpreted in an optics scenario as a sequence of N perpendicular linear birefringent gradients. By setting the origin of the axes to be (x_0, y_0), and letting the gradients be independent from N, we obtain the operators of the two optical axes:

$$\begin{aligned}\hat{U}_x &= e^{i\frac{\pi}{a}(x-x_0)\hat{\sigma}_x} \\ \hat{U}_y &= e^{i\frac{\pi}{a}(y-y_0)\hat{\sigma}_z},\end{aligned} \tag{4.6}$$

where $a = Nd$. The operators in Eq. 4.6 can be applied straightforwardly to an incoming photon travelling parallel to the $\hat{z}$-axis. Physically, the $\hat{U}_y$ and $\hat{U}_x$ operators can be modelled, respectively, by a prism which has an optical axis along the prism incline, and a second prism which has its optical axis offset by 45° from the first. These N number of perpendicular prism pairs, made out of quartz, are called "Lattice of Optical Vortices" (LOV) prism pairs.

The lattice of spin-orbit states is created by sending in circularly-polarized light into the LOV prism pairs. In the RSP experiment, $N = 2$, as shown in Fig. 4.2. The initial two-photon state generated by the Sagnac source is the Bell state, $|\Phi^+\rangle = \frac{1}{\sqrt{2}}(|LR\rangle + |RL\rangle)$. By sending the signal photon through $N = 2$ sets of LOV prism pairs, the prepared OAM lattice state is

$$|\Psi^{N=2}_{\text{LOV}}\rangle(x, y) = \frac{\alpha(x, y)}{\sqrt{2}}\left[(\hat{U}_x\hat{U}_y)^2 \otimes \mathbb{1}_2\right]|\Phi^+\rangle, \tag{4.7}$$

where $\alpha(x, y)$ describes the incoming Gaussian beam envelope, and $\mathbb{1}_2$ is the 2×2 identity matrix.

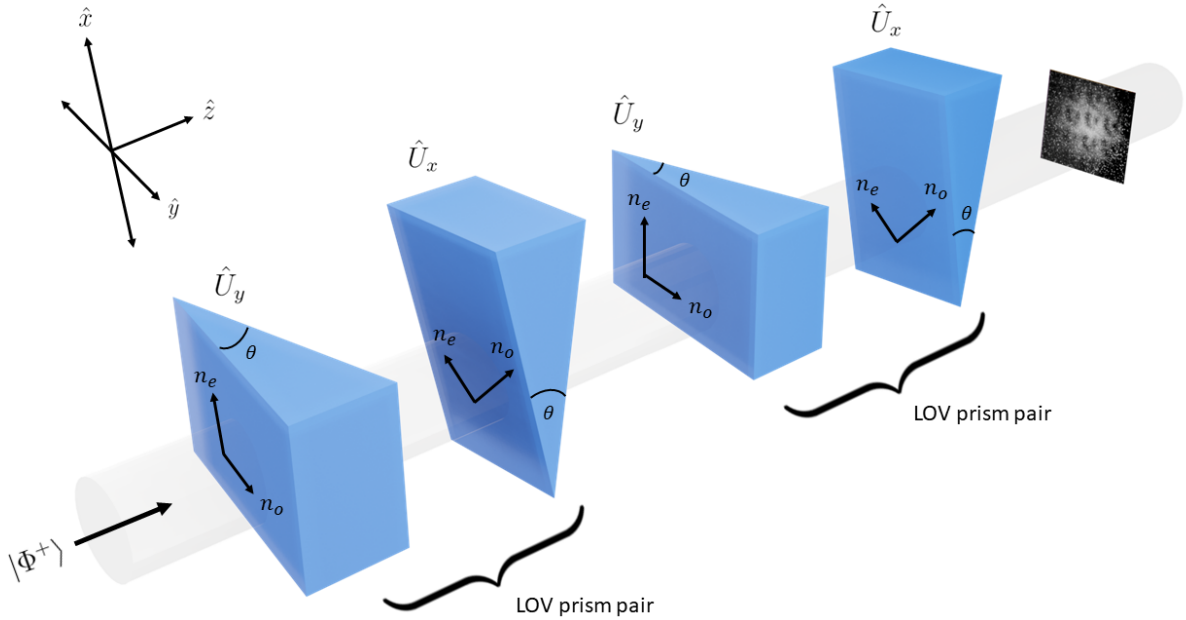

Figure 4.2: Diagram depicting an $N = 2$ lattice of spin-orbit states produced by passing $|\Phi^+\rangle$ through perpendicular pairs of quartz prisms whose optical axes are offset by 45°. A sample lattice pattern is detected (polarization projective measurement and spatial-resolving detector not shown).

To take a closer look at what happens when $|\Phi^+\rangle$ passes through the prism pairs, we apply the operators in Eq. 4.6 on the polarization states $|L\rangle$ and $|R\rangle$ to get

$$(\hat{U}_x\hat{U}_y)^2|L\rangle = A(x,y)|L\rangle + B(x,y)|R\rangle \tag{4.8}$$

and

$$(\hat{U}_x\hat{U}_y)^2|R\rangle = A(x,y)|R\rangle + B(x,y)|L\rangle, \tag{4.9}$$

where for a given spatial location (x, y), $A(x, y)$ and $B(x, y)$ are complex-valued amplitudes such that $|A(x,y)|^2 + |B(x,y)|^2 = 1$ when normalized. Examining Eqs. 4.8 and 4.9 shows that the LOV prism pairs are represented by unitary matrices which couple a photon's polarization to its spatial mode. Where photons pass through more of the quartz (in the $\hat{z}$-axis), a greater phase shift (i.e. greater polarization rotation) occurs due to the birefringence. Thus, different polarization projections applied to Eq. 4.7 will lead to different intensity patterns. Each pattern is a tessellation, because the prisms have been designed

so that when light has travelled a distance of a through the prisms, the phase shift is a multiple of $Nd = 2\pi$, resulting in a repeated pattern. a is called the lattice spacing, and can be written as $a = \lambda(\Delta n \tan(\theta))^{-1}$, where photon wavelength is λ, prism birefringence is Δn and the prism incline angle is θ. All of the LOV prisms in the RSP experiment have the same birefringence and are cut at the same incline angle.

This configuration of $N = 2$ LOV prism pairs corresponds to $l = \pm 1$. Note that the change in OAM number is not straightforward and requires additional prisms and polarization projective measurements. See Ref. [74] on how to change l.

In our experiment using the RSP protocol, only the signal photons are sent through the LOV prisms. The signal photon spatial patterns are conditioned on idler photon polarization measurements.

4.2.4 Electron-multiplying intensified CCD camera

The single photon camera used in the experiment is an electron-multiplying intensified CCD (emICCD) camera (PI-Max4: 1024 EMB by Princeton Instruments) and it uses the LightField software program. It is made up of a combination of an electron-multiplying CCD (EMCCD), and an intensified CCD (ICCD).

Here, we describe the picture-taking process and begin with the function of a standard ICCD. The process of picture-taking starts with incoming photons passing through the intensifier input window and hitting a photocathode causing the photoelectric effect, whereby one photon releases one electron from a metal with low work energy. The electrons are accelerated to a micro-channel plate made up of glass channels, and upon collision with the channel walls, they cause more electrons to be released. As these electron avalanches exit the channels, they are further accelerated by a high voltage and hit a phosphor screen. The inverse photoelectric effect happens, where the phosphorus absorbs the electrons and releases the same, discrete number of photons. The photons are then directed to an extra-sensitive CCD by fibre-optic coupling, and produce charge at the pixels they strike. These electrons first travel through a normal serial register. Here, the electron multiplication technique of an EMCCD comes in: the electrons then pass through a second extended register and are accelerated using a higher (relative to a normal serial register like the first) voltage. Secondary electrons are released within the register's silicon by impact ionization. These charges all reach an amplifier and create an electrical signal which is interpreted by the computer.

The electrons move from the intensifier into the micro-channel plate because the voltage at the plate is more positive. Increasing or decreasing the voltage at the plate respectively

changes the amount of electron gain caused by channel wall collision. This is the intensifier gain. Increasing or decreasing the voltage in the second register similarly changes the electron multiplier gain.

The emICCD has an electronically-controlled fast shutter. It can be programmed to open and collect data for less than 0.5 ns, but in the RSP experiment, we choose a 3 ns window. For timing purposes, the emICCD can also incorporate an electronic gate delay after it has received an electronic signal from a separate detector, but it must be more than 27 ns, else the camera cannot react fast enough. In our experiment, the emICCD only collects signal photons after it is triggered by the detection of their projection-measured idler partners. In order to compensate for the minimum electronic delay of 27 ns, the signal photons pass through a 30-m-long fibre spool. Refer to Appendix A on finding the optimal gate delay, which is the time after receiving the idler photon that the camera waits before opening the 3 ns window, and which has to be input into LightField.

The emICCD differentiates between exposures and frames. An exposure (a CCD-Accumulation on LightField) is a single instance of data collection when the shutter opens and closes. A frame is produced when analog data from the emICCD is digitized. If there are 100 exposures and 20 frames, then the shutter opens and closes $20 \times 100 = 2000$ times. The 20 frames are added together to produce a single image. For each polarization measurement, we accumulate signal photons for 2000 exposures in a single frame, and trigger the camera at a rate of 15 kHz (if there is less than 15,000 idler photons registered in a second, then the shutter remains closed). Every exposure takes about 2.35 sec to record. We focus on a 140×140 pixel area on the camera, and each pixel is 13 μm $\times 13$ μm.

There are several sources of error. The emICCD's CCD array is cooled to -20°c before collecting data and this helps reduce dark counts, but heat can still cause pixels to light up. Cosmic rays which pass through the shutter can be mistaken for photons and cause electrons to be released and pixels to light up in this way. Dust, or anything physical, can cause misfires by interfering with the intensifier. We also note that the quantum efficiency[3]of the camera at our photon wavelength is about 25%.

The camera's manual ([76]) and Matthew Brown's thesis ([77]) have additional helpful information beyond the contents of this section.

[3]This is the probability of photo-electrons being released by a photon which enters the camera.

4.2.5 Quantum state tomography

One way of ensuring that a quantum state has been prepared correctly is to reconstruct its density matrix from experimental measurements. This process is called quantum state tomography, which is accomplished by performing a tomographically complete set of measurements on identical copies of the prepared state. A set of measurements is tomographically complete if the measurement operators form an operator basis on the Hilbert space of the system. The set that we use in the RSP experiment is $\{|H\rangle, |V\rangle, |D\rangle, |R\rangle\}$. A two-photon density matrix is 4×4, so there are 16 elements to be solved for, thus 16 count statistics must be provided by 16 different measurements.

One common density matrix reconstruction method is linear tomography, which uses Born's rule to infer probabilities by comparing the relative counts of different measurements. However, linear tomography can produce unphysical density matrices when the count statistics are noisy. This scenario applies to the RSP experiment as our counts are subject to noise from the emICCD, so instead, we employ a maximum likelihood quantum state tomography algorithm based on Ref. [78].

In the maximum likelihood tomography approach, a density matrix which is constrained to be physical is randomly generated as an initial guess for an optimization routine. The physicality constraints are hermiticity, positivity, and normalization. The likelihood error function, $\mathcal{L}$, is minimized numerically over the set of all density matrices:

$$\mathcal{L}(\hat{\rho}) = \sum_{i=1}^{16} \frac{\left[\mathcal{N}\mathrm{Tr}(\hat{\rho}|\psi_i\rangle\langle\psi_i|) - n_i\right]^2}{2\mathcal{N}\mathrm{Tr}(\hat{\rho}|\psi_i\rangle\langle\psi_i|)}. \tag{4.10}$$

$\hat{\rho}$ is the two-photon density operator to be reconstructed, i is the variable which indexes the 16 different measurements, $|\psi_i\rangle\langle\psi_i|$ are the measurement operators, n_i are the raw counts measured in the experiment, and $\mathcal{N}$ is the total number of counts before the projective measurement. $\mathcal{N}$ is retrieved from a subset of the measurements using the following relationship:

$$\begin{aligned}\mathcal{N} = {} & \mathrm{Tr}(\hat{\rho}|\mathrm{HH}\rangle\langle\mathrm{HH}|) + \mathrm{Tr}(\hat{\rho}|\mathrm{VV}\rangle\langle\mathrm{VV}|) \\ & + \mathrm{Tr}(\hat{\rho}|\mathrm{HV}\rangle\langle\mathrm{HV}|) + \mathrm{Tr}(\hat{\rho}|\mathrm{VH}\rangle\langle\mathrm{VH}|).\end{aligned} \tag{4.11}$$

In the RSP experiment, maximum likelihood tomography is used twice. Firstly, it is used to obtain the Bell state fidelity directly after the Sagnac interferometer. Secondly, the fidelity of the each pixel position with all four Bell states was calculated with both the experimental and simulated intensity distributions. In both cases, Eq. 1.28 is used.

4.3 Experimental setup

The experiment consists of four main parts, as depicted in Fig. 4.3. Heralded entangled photon pairs are generated via type-II SPDC by the Sagnac source, shown in the top left yellow area. A 10-mm-long periodically-poled potassium titanyl phosphate crystal (ppKTP) is pumped using a 404 nm continuous wave diode laser to produce degenerate photon pairs centered at $\lambda = 808$ nm with a spectral bandwidth (FWHM) of 0.4 nm. The outputs of the Sagnac source are coupled into single mode fibres (SMFs), and immediately after leaving the source, the $|\Phi^+\rangle$ Bell state was measured to have a fidelity of 96%.

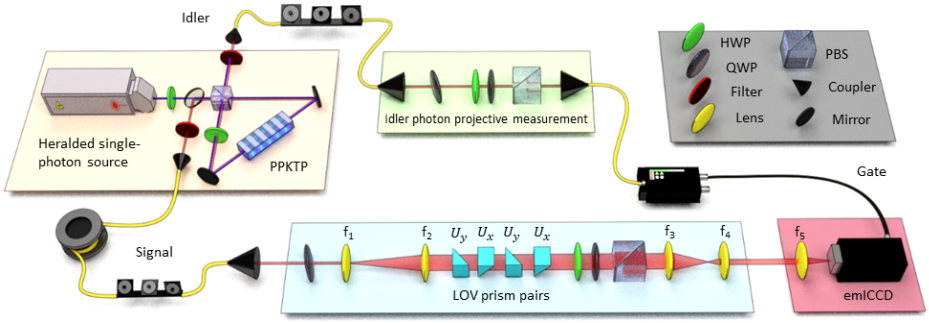

Figure 4.3: A schematic of the RSP experiment.

The signal photons then passes through a 30-m-long fibre spool and polarization control in the form of bat ears before being magnified by an optical telescope, made out of lenses f_1 and f_2. The telescope magnifies the signal photons by a factor of 8.3, before they pass through two sets of LOV prism pairs. The magnification controls the number of lattice periods in the emerging intensity pattern by illuminating a larger portion of the prisms, and was chosen such that a 3×3 pattern is observed in the intensity distributions. The prisms are cut at an incline angle of $\theta = 2°$. Eq. 2.4 is used to calculate the birefringence $\Delta n = |n_e - n_o| = 0.0089$ for the photon wavelength of 808 nm in quartz.

The modified signal photons are sent through polarization analyzing optics which consist of a HWP, a QWP, and a PBS. Finally, the beam is demagnified by a factor of 4 by means of a second optical telescope, made out of lenses f_3 and f_4, and the signal photons are sent to the emICCD camera.

The idler photons are directly sent to polarization analyzing optics and detected by an avalanche photodiode which triggers the emICCD, opening an electronic gate for 3 ns in order to collect data. The simulated intensity distributions were produced in Python.

4.4 Results

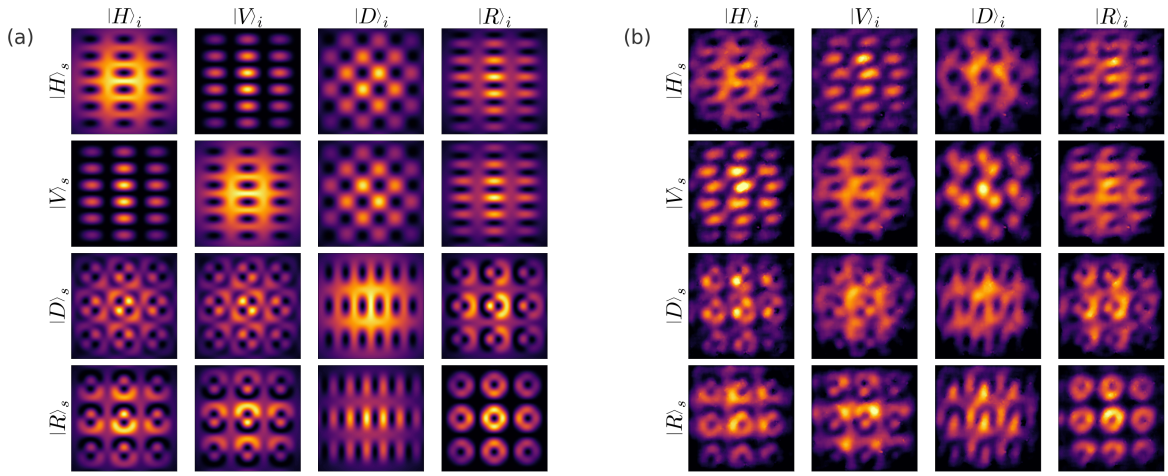

Figure 4.4: Theoretical predictions (a) and experimental results (b) for the 16 intensity distributions corresponding to the tomographically complete set of $\{|H\rangle, |V\rangle, |D\rangle, |R\rangle\}$.

In Fig. 4.4, we compare the theoretically calculated (Fig. 4.4(a)) and experimentally measured (Fig. 4.4(b)) two-dimensional intensity patterns for all 16 measurement configurations in the tomographically complete set $\{|H\rangle, |V\rangle, |D\rangle, |R\rangle\}$. Rows and columns are organized by signal and idler projective measurements, respectively, and labelled by the corresponding polarization.

The theoretical predictions and the experimental data are in qualitative agreement. LOV prism pair alignment challenges associated with setting and maintaining the phase is the most probable cause of slight pattern distortion as compared with theory. In both cases, we used a grid of 140×140 points. In the image plane of the emICCD, the simulated lattice spacing in Fig. 4.4(a) is 0.519 ± 0.015 mm, while the measured lattice spacing in Fig. 4.4(b) is 0.522 ± 0.013 mm.

For the purpose of viewing the intensity distributions for qualitative assessment, the raw intensity profiles from the emICCD are normalized, and post-processed using background subtraction and an adaptive two-dimensional Gaussian image filter. An artificial colour scheme was used for visual clarity, since the emICCD records photon counts only.

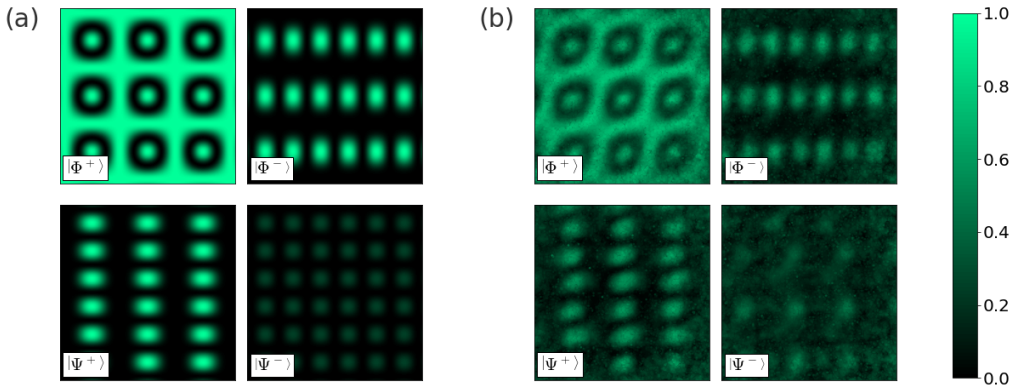

Figure 4.5: Plots of pixel-wise maximum likelihood tomography by means of the fidelity of all four Bell states. (a) Tomography seeded with simulated intensity distributions shown in Fig 4.4(a). (b) Tomography seeded with experimental intensity distributions shown in Fig. 4.4(b).

In Fig. 4.5, we take the theoretical and experimental density matrices, $\hat{\rho}(x, y)$, calculated at each pixel position, and present the fidelity with each of the four Bell states using Eq. 1.29. For example, the top left image in Fig. 4.5(a) shows how similar the theoretical density matrices, $\hat{\rho}(x, y)$, are to the $|\Phi^+\rangle$ Bell state by plotting the fidelity $\mathcal{F}(x, y) = \mathrm{Tr}\left[\hat{\rho}(x, y) |\Phi^+\rangle \langle\Phi^+|\right]$. In both the theoretical and experimental case, $|\Phi^+\rangle$, $|\Phi^-\rangle$, $|\Psi^+\rangle$, and $|\Psi^-\rangle$ Bell state fidelities are shown. There is good qualitative agreement between experiment and theory, with a reduced experimental fidelity overall.

The pixel-wise quantum tomography code which produced Fig. 4.5 was seeded with the intensity distributions shown in Fig. 4.4. This is to say, each pixel (x, y) in each image in Fig. 4.5 used the 16 density matrices (represented in each measurement configuration in Fig. 4.4) computed at that position (x, y), for quantum tomography. For the purpose of computing the experimental density matrices, the raw counts from the sum of exposures are used.

When comparing the $|\Phi^+\rangle$ of Fig. 4.5(a) and Fig. 4.5(b), you can see that the areas around the ring-shaped regions, along with the centre of these regions, have had a phase rotation of a multiple of 2π from the starting Bell state $|\Phi^+\rangle$. Looking at the other images in Fig. 4.5, it is apparent that at different pixel positions, the input state has been rotated

to other Bell states. Pixel-wise quantum state tomography thus enables a visualization technique to show how the spin-orbit lattice state evolves across the transverse beam profile.

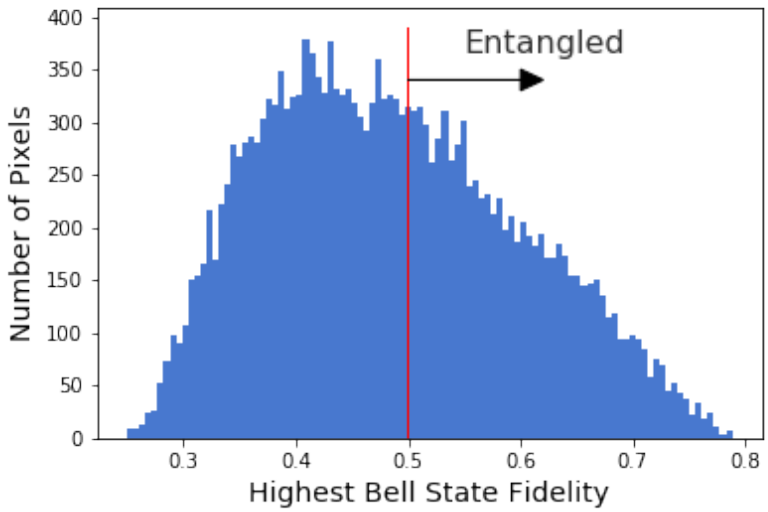

Figure 4.6: Histogram of the highest Bell state fidelity over all pixel positions. A red line is overlaid at 0.5 fidelity. All pixels with a fidelity greater than 0.5 with one of the four Bell states are definitely entangled.

A histogram presenting the highest Bell state fidelity at each pixel position is presented in Fig. 4.6. Recall that every experimental density matrix belonging to a pixel had its fidelity calculated with each of the four Bell states as shown in Fig. 4.5(b). The highest fidelity, regardless of which Bell state it was with, was plotted in Fig. 4.6. In the experimental case, 42.5% of all pixel locations have a fidelity of more than 0.5 with one of the four Bell states. This confirms entanglement between the signal photons measured at the pixel locations and the idler photons that trigger the camera because qubit separable states cannot achieve a Bell state fidelity of more than 0.5 [3]. In the theoretical case, 85.7% of pixel locations are entangled in this way, so even with perfect image contrast and quantum state preparation, not all positions of this pattern significantly overlap with one of the four Bell states. 14.3% of pixel locations instead must have been rotated by the prisms such that they overlap with other maximally entangled states.

The slight pattern distortion is the most likely cause of the decrease in number of entangled pixels. Having a higher initial Bell state fidelity (we started with 96%) would

help increase the experimental number of pixels which have a Bell state fidelity of more than 0.5. Some error may be due to random fluctuations arising from the emICCD mechanisms. Also, the entanglement might have degraded because the prisms might not be manufactured perfectly. If the prisms were fabricated with some flaws, their physical birefringent linear gradients would not be modelled well by the unitaries (given in Eq. 4.6), and passing through the LOV prisms would cause the entanglement to drop.

I note that plotting Bell state fidelities helps to illustrate the spatially-dependent rotation of the two-photon spin-orbit lattice state. Fig. 4.6 supports the verification of the successful remote preparation of spin-orbit states.

4.5 Conclusion

In the RSP experiment, we implement a remotely prepared optical lattice of spin-orbit states by passing polarization-entangled photon pairs into two pairs of LOV prisms. The success of the remote preparation of the spin-orbit entangled state is verified using an emICCD camera using a pixel-wise quantum tomography algorithm. We observe that the entanglement present in the starting two-photon Bell state transforms such that there are overlaps with different Bell states depending on which portion of the LOV prism pairs the signal photon passes through. We also show that pixel-wise quantum tomography on images acquired by an emICCD camera is a useful method for observing spatially-dependent two-photon states.

In general, this work advances the study of quantum correlations of structured beams with lattice frameworks. It promotes a less common method for producing spin-orbit states, which is normally done by q-plates [79, 80] and spatial light modulators [81]. The periodicity of these novel lattice structures can be employed in applications in quantum sensing and control, such as in the creation of all-optical memory devices using the interference of OAM lattices [62] and the continuous and non-destructive measurement of the average deviation of atoms relative to their lattice sites [60]. This work demonstrates but a few of these structures; changing the polarization angles gives access to a larger variety.

Spin-orbit states have also proven useful to combat turbulence, as correlations between polarization and OAM have shown to preserve encoded states after propagation in diffuse media [67, 82], thus a lattice of such states as produced in the RSP experiment may be additionally helpful for robustness. Future work might include using a higher number of LOV prism pairs in order to have lattices that access higher radial quantum numbers, as quantum communication protocols benefit from having a larger alphabet to encode spin-orbit states. The RSP experiment demonstrates methods of manipulating and measuring

spin-orbit entangled photon pairs, which work towards the objective of being able to fully utilize single photons for quantum information processing purposes.

Chapter 5

Kerr switching of entangled photons

Notes and acknowledgments

The work in this chapter has not been fully completed.

Contributions

This study is an on-going collaboration between labs of Kevin Resch and Benjamin Sussman. The idea was conceived by **Kevin Resch** from a paper written by the Sussman group [83].
Philip Bustard, **Duncan England**, **Sacha Schwarz**, and **Kate Fenwick** are helping with ongoing support and strategy in experimental considerations.
Andrew Cameron and **Sandra Cheng** have aligned the current experimental setup and are taking data.

5.1 Motivation and chapter overview

In the switching experiment, the goal is to use the optical Kerr effect in a bare fibre to switch an entangled photon. Given our parameters of the fibre length, the temporal width of the gate, and wavelengths of the gate and signal, the intrinsic switching speed is on the order of 0.3 ps. Furthermore, Ref. [83] has also demonstrated that it is possible to

switch single photons with an efficiency close to 1 without the decoherence of the quantum properties of the photons.

Switching light is probably what you think it is: being able to flip between two states of light. In this project, the difference is between polarization states. All-optical switching's claim to fame is not being limited by electronic speed and has a myriad of applications: in both classical [84, 85], quantum communications [86, 87], biomedical imaging [88], and microscopy [89]. The work in this chapter was primarily motivated by Ref. [83] in that our current interest lies in increasing the switching speed of single photons by using a shorter optical fibre Kerr medium. They have presented a Kerr switching speed of 1.7 ps and we are interested in sub-picosecond optical gating, which requires sub-picosecond speeds for sub-picosecond time resolution. Ultimately, this project aims to reconstruct the two-photon entangled state by using the Kerr effect in a third-order cross-correlation as partially described by Eq. 3.53. Separation by polarization is straightforward and effective, and the switching efficiency can be made to be rather high. This gives Kerr switching an advantage over other kinds of optical gating based on parametric nonlinear effects such as SFG [90], which relies on the low efficiency of up-conversion to provide signal. As long as the switching speed is on similar timescales to that of the signal (and eventually, idler) temporal widths, it is viable to use for the reconstruction of a joint two-photon entangled state [91].

Section 5.2, supplemented with Section 3.4, covers the theory and concepts belying the Kerr switch including the switching model used. Section 5.3 goes through a preliminary experimental setup with results for the switching of continuous wave light. Section 5.4 details the current experimental setup for the switching of single entangled photons. In particular, section 5.4.2 introduces future experimental considerations, including the characterization of the noise arising from the pump. Section 5.5 comprises of concluding remarks.

5.2 Theory and concepts

5.2.1 Optical Kerr switching

Much of the theory regarding the $\chi^{(3)}$ optical Kerr effect has already been fleshed out in Section 3.4, and the contents of this section continue from there. Previously, we have seen that a propagation of an intense optical field, termed the pump field or the gate, through a centrosymmetric $\chi^{(3)}$ medium is the cause of the intensity-dependent refractive index. Since the pump field induces this change in refractive index along its polarization axis, it effectively causes a localized birefringence in the Kerr medium and essentially causes the

medium to mimic a waveplate wherever the pump pulse is located. With this behaviour, the polarization of a much weaker pulse can be rotated. This secondary pulse, normally called the signal, must have an intensity which is significantly lower than the pump so that we may assume it does not affect the refractive index. This specific use of the optical Kerr effect where one wavelength of light affects the phase of another is XPM. In our setup, the Kerr medium is the core of a bare fibre (Thorlabs S630-HP), which is made of pure silica. It is surrounded by cladding made of fluorine-doped silica.

In many instances, the Kerr medium is sandwiched between two crossed polarizers in a configuration known as an optical Kerr shutter (OKS) [92]. Fig 5.1 is a simplified diagram of the OKS in our setup. A dichroic mirror is first used to reflect the gate and transmit the signal into the bare fibre. After the medium, a spectral filter is used to remove the gate so that only the signal is collected.

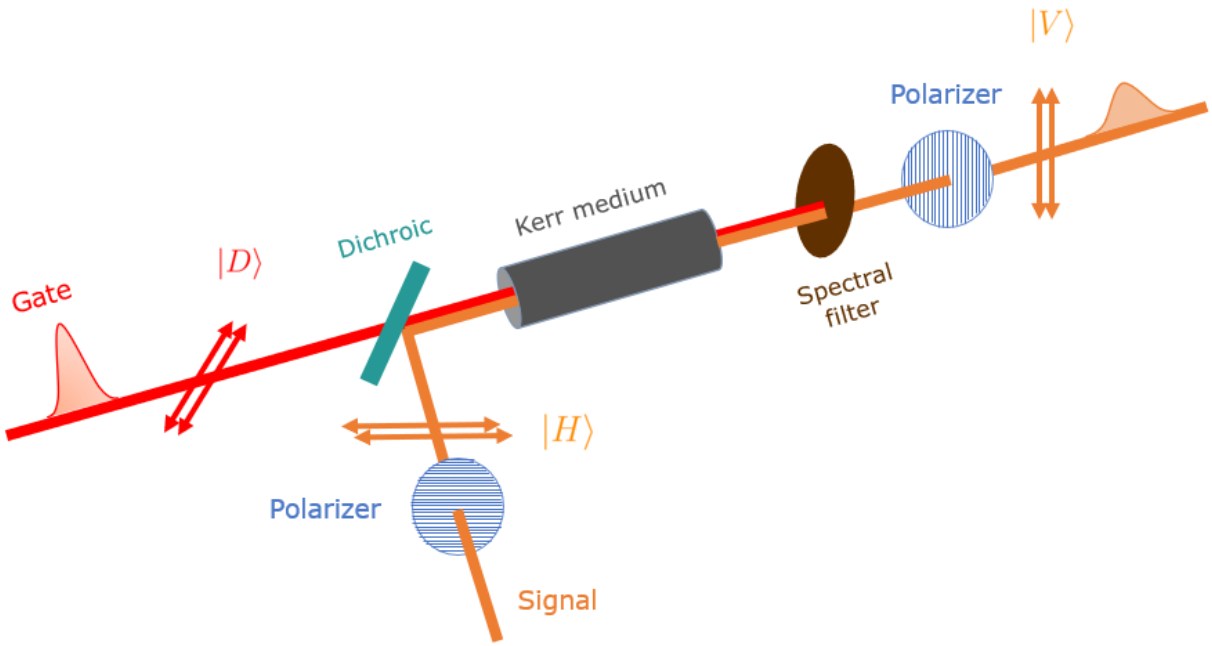

Figure 5.1: A diagram of an optical Kerr shutter with a dichroic mirror before the Kerr medium, a bare fibre, and a spectral filter after the medium. The polarizations of the optical fields involved are indicated on the diagram.

The switching efficiency η of the OKS setup is [93]

$$\eta = \sin^2(2\theta)\sin^2(\frac{\Delta\phi}{2}) \tag{5.1}$$

where θ is the angle between the pump and signal polarizations, and $\Delta\phi$ is the phase shift induced by the pump beam. $0 \leq \eta \leq 1$, where 0 means no polarization rotation and 1 is polarization rotation to an orthogonal state. Signal photons which have been successfully rotated by the pump pulse are 'switched'. Note that the factor $\sin^2(2\theta)$ arises purely from the addition of the crossed polarizers. To maximize Eq. 5.1, $\theta = \pm 45°$. $\Delta\phi$ is given by the B-integral, which is a measure of the nonlinear phase shift of light along the optical axis of a nonlinear optical system. It is expressed as [94]:

$$\Delta\phi = \frac{2\pi n_{NL}}{\lambda_{signal}} \int_{z=0}^{z=L} I(z,t)\mathrm{d}z, \tag{5.2}$$

where n_{NL} is nonlinear refractive index, λ_{signal} is the signal wavelength, $I(z,t) = |\mathbf{E}(z)|^2$ is the pump intensity as it travels through the fibre and z is a length parameter describing the distance along the medium.

For practicality, the pump and signal are often located in different spectral regions, so temporal walk-off must be considered for a better model of Eq. 5.2. If the pulses do not travel together in the medium, then the rotation of the signal photon cannot occur and the overall efficiency is decreased. The temporal walk-off between the gate pulse and the signal pulse is given by Eqs. 3.21 or 3.22, where L is the length of the Kerr medium and $n_{gp} = \frac{c}{v_{gp}}$ and $n_{gs} = \frac{c}{v_{gs}}$ are the group indices of the pump and the signal in the medium. We can now express the intensity profile of the pump $I(z,t)$ in the reference frame where we are moving with the signal photon. Let $T = t - \frac{z}{v_{gs}}$, and the temporal walk-off be defined as $d_w = \frac{1}{v_{gp}} - \frac{1}{v_{gs}}$.

By letting $\theta = +45°$ in the experiment, the switching efficiency can now be written as:

$$\eta(T) = \sin^2\left(\frac{\pi n_{NL}}{\lambda_{signal}} \int_{z=0}^{z=L} I(z, T - zd_w)\mathrm{d}z\right). \tag{5.3}$$

The form of $I(z, T - zd_w)$ is dependent on the shape of a pump shape. In this experiment, we assume a Gaussian profile with an intensity given by:

$$I_{pump}(T) = I_0 \exp\left[\frac{-4\ln(2)(T - zd_w)^2}{\Delta\tau_{pump}^2}\right], \tag{5.4}$$

where I_0 is the peak intensity of the pump, $\Delta\tau_{pump}$ is the temporal width of the pump (FWHM) and as above, $T = t - \frac{z}{v_{gs}}$.

Additionally, note that the peak intensity is related to the peak power P_{peak} and area by:

$$I_0 = \frac{P_{peak}}{\pi r^2}, \tag{5.5}$$

where r is the radius of the pump pulse. Since it travels in an optical fibre, we can estimate r as the field mode diameter of the fibre divided by two. The peak power is related to the average power P_{avg}, the pulsed laser repetition rate R, and the pump pulse duration, $\Delta\tau_{pump}$, by:

$$\frac{P_{avg}}{R} = P_{peak}\Delta\tau_{pump}. \tag{5.6}$$

Putting Eq. 5.6 into Eq. 5.5, the peak pump power I_0 in terms of average power P_{avg} as measured by a power meter in the lab, is:

$$I_0 = \frac{P_{avg}}{R\Delta\tau_{pump}\pi r^2}. \tag{5.7}$$

Eq. 5.3 is only a description of the switch if the signal input is a delta function, so Eq. 5.3 is referred to as the intrinsic response function. For an experimental model of the switch, the temporal width of the signal must be considered. In this case, the intrinsic response must be integrated over the duration of the signal weighted by its temporal profile $I_{signal}(t)$:

$$\eta_R(T) = \int_{-\infty}^{\infty} \eta(T) I_{signal}(t) \mathrm{d}t, \tag{5.8}$$

where, similar to Eq. 5.4, the signal pulse is assumed to be Gaussian:

$$I_{signal}(t) = I_s \exp\Big[\frac{-T^2}{\Delta\tau_{signal}^2}\Big], \tag{5.9}$$

where the peak intensity of the signal, I_s, is assumed to be negligibly small and does not affect the refractive index. Eq. 5.8 has dependencies on four factors: the temporal width of the pump and signal, the temporal walk-off between the two pulses, and the length of the medium. The FWHM of this function gives the experimental switching speed. In this work, the switching medium is a bare fibre of fused silica which bears centrosymmetry. The n_{NL} for fused silica has been empirically measured to be about $3 \times 10^{-16} \frac{\mathrm{cm}^2}{\mathrm{W}}$ [94]. Recall that to see a noticeable change in the refractive index as per Eq. 3.44, the term $n_{NL}I$ must be significantly high. We achieve this by using an ultrashort pulse for the pump which is focussed down to a few-micron spot size, so the induced birefringence occurs at ultrafast timescales. The bare fibre was chosen despite the relatively low n_{NL} of silica because of its waveguiding properties, which allow for better overlap of the pulses, and its commercial availability.

5.3 Proof-of-principle continuous wave switching

Before attemping to switch single photons, a proof-of-concept of Kerr switching in a bare fibre was demonstrated. A helium-neon (He:Ne) laser (Thorlabs HRS015B), centred at 633 nm, was switched by means of a pulsed gate centred at 775 nm in a 10-cm-long bare fibre (Thorlabs S630-HP), as depicted in Fig. 5.2. The ultrashort gate comes from a 80 MHz repetition rate Titanium:Sapphire laser (Chameleon Ultra II from Coherent) and is coloured red. The He:Ne is coloured pink. Both wavelengths were measured by a handheld spectrometer (OceanOptics HR2000+).

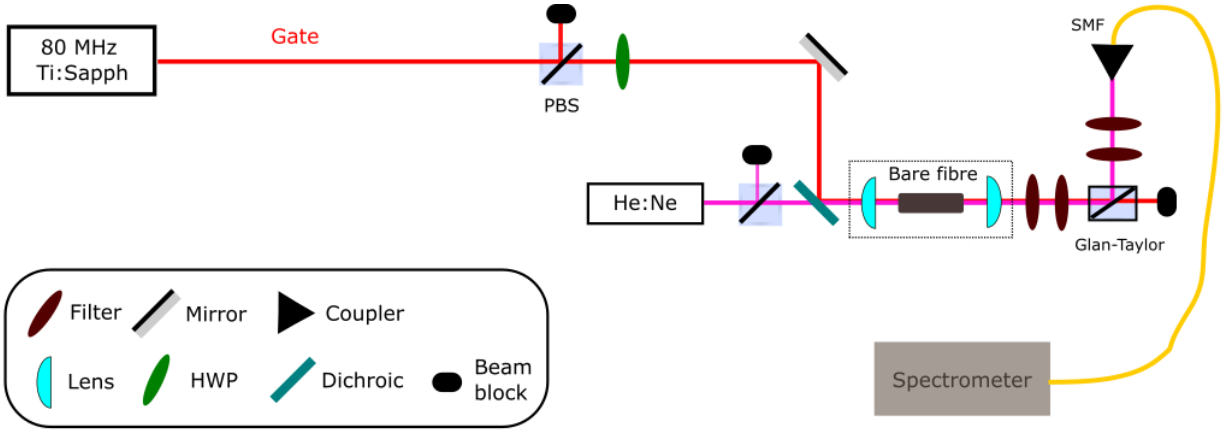

Figure 5.2: Schematic of the switching experiment with a continuous wave laser.

The gate was set to $|D\rangle$ (by a PBS and HWP) and the input He:Ne light was set to $|H\rangle$ (by a PBS) for maximum switching efficiency ($\theta = \pm 45°$, as per Eq. 5.1). Both passed through a lens to be focused into the bare fibre. Another lens was set up after the fibre to collimate the outgoing light, since it disperses quickly after exiting a waveguide. After the Kerr switch, a set of filters and an efficient PBS (a Glan-Taylor) were used to remove the gate, and He:Ne light which had not been switched. The rotated light, now at $|V\rangle$, was coupled into a SMF and was passed into a spectrometer (Princeton Instruments: Acton SP-2750). The average powers of the He:Ne and the gate were respectively 50 μW and 50 mW (measured just after the Kerr medium) with bare fibre coupling efficiencies of 35% and 21%. General experimental and alignnment procedures for coupling light into a bare fibre can be found in Appendix D.

The spectrometer was used to collect spectra of four different combinations of the gate and the He:Ne being ON and OFF for proper characterization of the switching response.

ON means light was allowed to pass through the bare fibre, and OFF means light was blocked from entering the fibre. The four configurations correspond to:

- He:Ne ON, gate ON: switching,
- He:Ne ON, gate OFF: He:Ne light leakthrough (unswitched light),
- He:Ne OFF, gate ON: other nonlinear effects (e.g. self-phase modulation),
- He:Ne OFF, gate OFF: background noise.

In each configuration, 5000 spectra were collected with a 10 ms integration time each.

5.3.1 Experimental continuous wave switching response

In the continuous wave case, the signal beam is on at all times, so the intrinsic response, Eq. 5.3, defines the switching efficiency of the input light; there is no need to use Eq. 5.8. We use the experimental parameters of: 775 nm pump wavelength, 633 nm He:Ne wavelength, fibre length of 10 cm, $n_{NL} = 3 \times 10^{-16} \frac{\text{cm}^2}{\text{W}}$ for silica, $r = 2.1 \times 10^{-6}$ m for the field mode diameter, and a pump duration of 220 fs (measured by autocorrelation with SFG). The group velocities were calculated from experimentally determined values of n_{gp} and $n_{g_{He:Ne}}$ [95]. By taking a fast Fourier transform of Eq. 5.3, the theoretical spectral response can be obtained. This is the orange curve shown in Fig. 5.3.

The four different experimental datasets were collected and averaged to generate the final switching response curve of the He:Ne [96]:

$$I_{switched} = (I_{He:NeON,gateON} - I_{He:NeON,gateOFF}) - (I_{He:NeOFF,gateON} - I_{He:NeOFF,gateOFF}). \tag{5.10}$$

The curve is denoted by blue dots in Fig. 5.3. There is a single negative intensity value which can be disregarded. It arises from noise, causing the combination of all spectra in Eq. 5.10 to add up to a negative intensity.

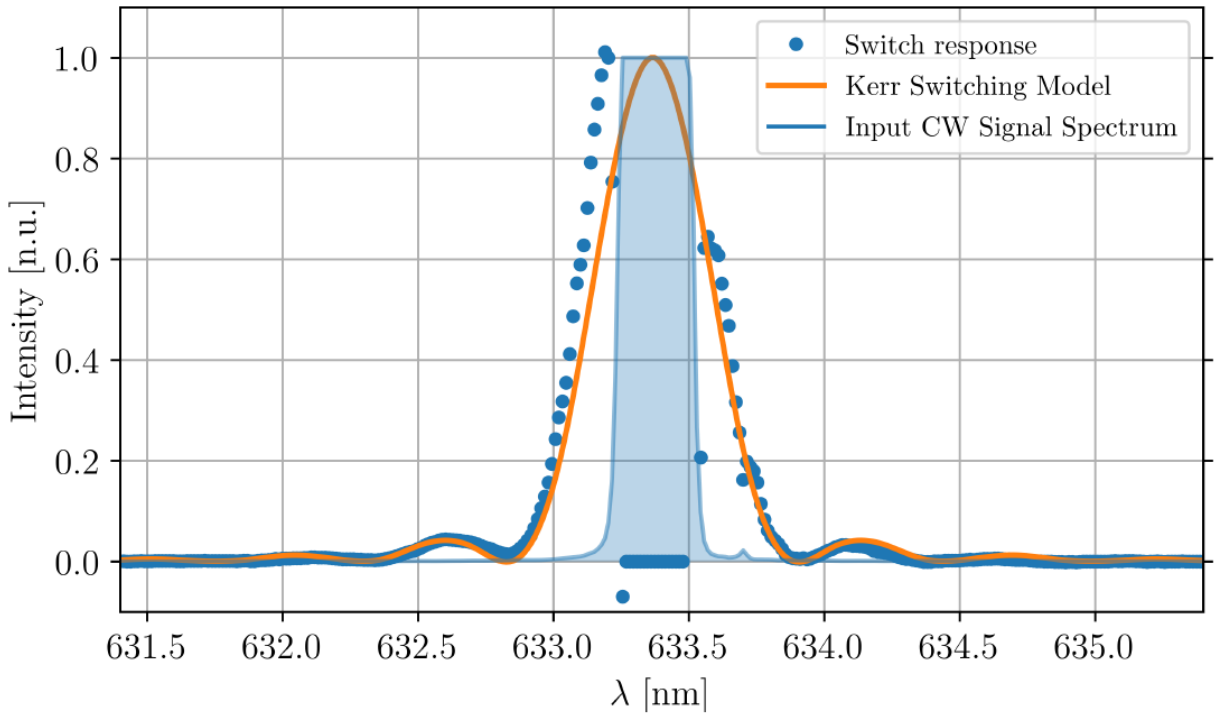

Figure 5.3: Switching response (blue dots) of the 633 nm He:Ne in a 10-cm-long bare fibre using a pump pulse of 775 nm, plotted with the intrinsic Kerr switching efficiency (orange line), and the input continuous wave He:Ne spectrum (light blue area). Figure created by Sacha Schwarz and data collected by Kate Fenwick and Sandra Cheng.

Using the appropriate average power input, the experimental switching response agrees well with the intrinsic switching efficiency. Slight deviation may be due to not accounting for pump pulse chirp. We note that the He:Ne spectrum is too strong near the peak of its output so that the switching response cannot be extracted. This noise will, however, not be an issue when switching with single photons as the intensities are too weak.

5.4 Single photon switching setup

To obtain an intrinsic switching speed near the order of 0.3 ps, a new bare fibre length of 3 cm was chosen. At this short of a length, we have to consider how to evaluate the average power in the core. In a typical SMF, light passes through both cladding and core (for reference in a Thorlabs S630-HP, the cladding is 125 ± 1 μm and the core is

3.5 μm), but the cladding modes are extinguished as they travel through the fibre since a SMF is designed to output only one spatial mode: the TEM_{00} mode, which is Gaussian. This is to say that in the switching experiment, we only want Gaussian light because the birefringence due to the Kerr effect only occurs in the core. A 3-cm-long fibre allows some cladding modes to pass through, so average powers and counts cannot be measured by putting a power meter or detector after the Kerr medium. In this case, we note the average power and detector counts by examining the light which has passed through the Kerr medium and through another SMF.

A diagram of the single photon experimental setup is shown in Fig. 5.4. The ultrashort gate pulse remains 775 nm and is coloured red in Fig 5.4. Again, it originates from a 80 MHz repetition rate Titanium:Sapphire laser (Chameleon Ultra II from Coherent). It undergoes SHG in a BiBO crystal and produces blue light at 387.5 nm. Both the wavelengths were measured with the handheld spectrometer (OceanOptics HR2000+). The gate reflects off a dichroic mirror and follows a different path. The blue light transmits through to another BiBO crystal to undergo SPDC and produce non-degenerate entangled photon pairs. The signal and idler photons were measured to be, respectively, 823 nm and 732 nm by single photon spectrometers built in-house (detailed in Ref. [97]). These wavelengths can be adjusted by phase-matching and their bandwidths are tuned by filters. Additional information on this entangled photon source can be found in Appendix C.

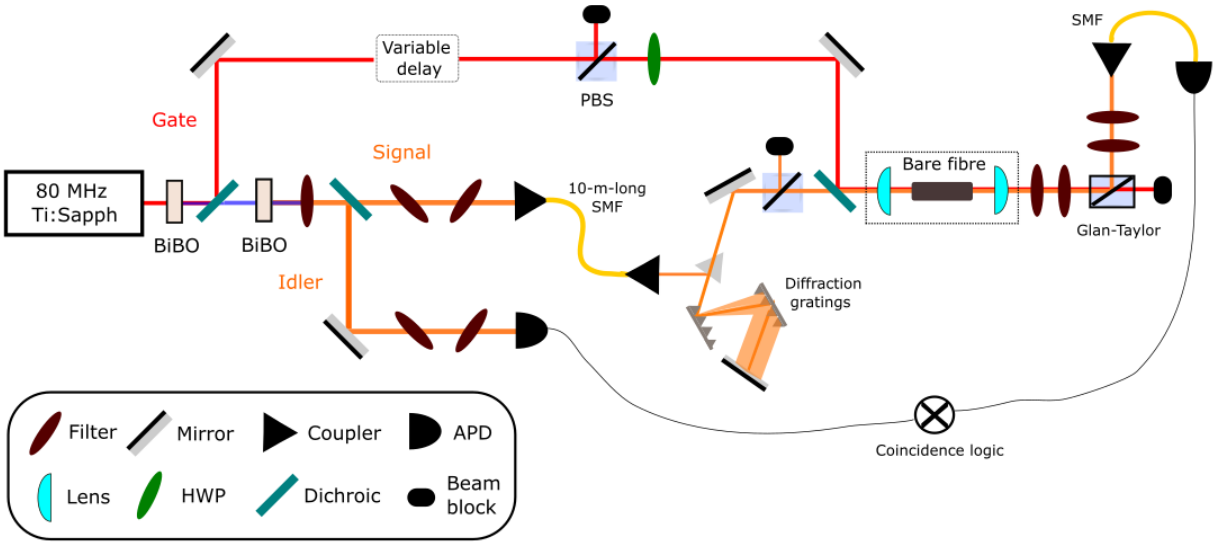

Figure 5.4: Schematic of the switching experiment for single photons.

The photon pairs are split up by another dichroic and coupled separately. The idler is

coupled to an APD and acts as a herald for the signal photon. The signal is shuttled into another part of the table by a 21-m-long SMF, and passes through a grating compressor (made of a pair of diffraction gratings) to compensate for chirp accumulated by travel in the SMF. A correct combination of the two allows for dispersion control. It then passes through polarization settings (a PBS) before meeting the gate pulse just before the Kerr medium. The gate pulse at this point has already passed through a variable delay (by means of a retroreflector on a translation stage) and also has its polarization set (a PBS and HWP). The variable delay is needed here to be able to sweep the gate pulse through the signal pulse (unlike with He:Ne which was always present in the Kerr medium). Recalling Eq. 5.1 and similar to the continuous wave case, the gate is set to $|D\rangle$ and the signal at $|H\rangle$ for maximum switching efficiency.

Both pass through a lens in order to be focused into the Kerr medium, a 3-cm-long bare fibre (Thorlabs S630-HP). The same collimating lens is set up after the fibre. After the Kerr switch, a set of four filters and an efficient PBS (a Glan-Taylor) is used to remove the pump, and signal photons which have not been switched. The rotated signal photons are coupled to an APD by another SMF. Coincidence logic is applied between the rotated signal APD and the idler APD.

5.4.1 Intrinsic switching response

Many of the same experimental parameters in the continuous wave case were used to obtain the intrinsic switching response in the single photon case, with the exception of using a 823 nm signal wavelength and the corresponding value for the group velocity, and a pump temporal width of 300 fs (measured by autocorrelation with SFG).

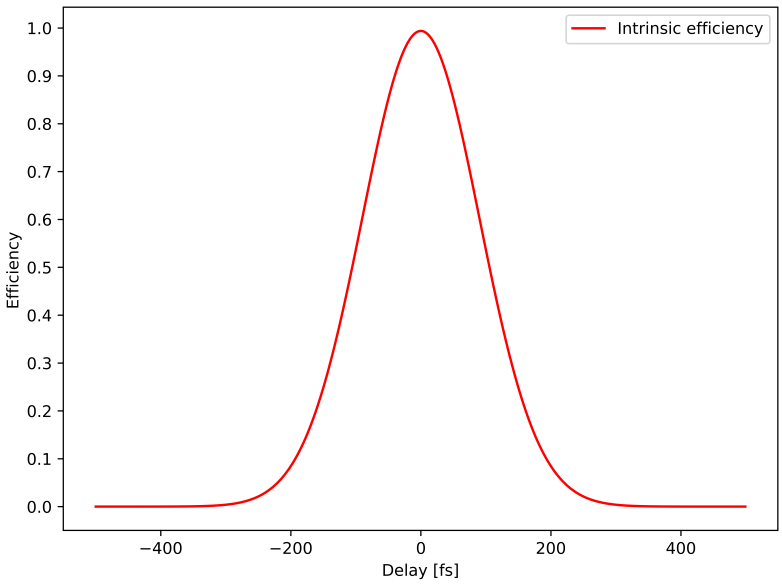

Figure 5.5: The intrinsic switching response of the 3-cm-long bare fibre Kerr switch in the single photon scenario, using a 775 nm pump wavelength, a 823 nm signal wavelength, and a pump temporal width of 300 fs. The temporal width of the signal photon is not incorporated.

The width of Fig. 5.5 implies an approximate switching speed of 0.348 ps, which is of an appropriate ps timescale. The experimental switching speed should be slightly slower, as the inclusion of the signal's temporal profile should broaden the response function. This numerical integration does not include the effects of chirp as the pump and signal propagate through the bare fibre. We assume it is negligible because the fibre is short. Temporal walk-off (using Eq. 3.22) between the two pulses is calculated to be 5.83 $\frac{\text{ps}}{\text{m}}$ corresponding to 0.1749 ps walk-off in the fibre, so we believe that the pulses are sufficiently temporally overlapped in the fibre and will not affect efficiency. For a better guess of the switching response, the temporal width of the signal should be measured so that Eq. 5.8 can be used.

5.4.2 Future experimental considerations

The switching efficiency given by Eq. 5.3 changes for different pump power intensities in the core since the change in refractive index is induced by the intensity of the strong light (recall Eq. 3.44; it is implicit in Eq. 5.8). To get an efficiency near 1 using our experimental parameters, we need about 90 mW of average power in the core as shown in Fig. 5.6. Note that the gate pulse has a coupling efficiency of 15% so the maximum efficiency corresponds to 0.6 W of pump power entering the Kerr switch.

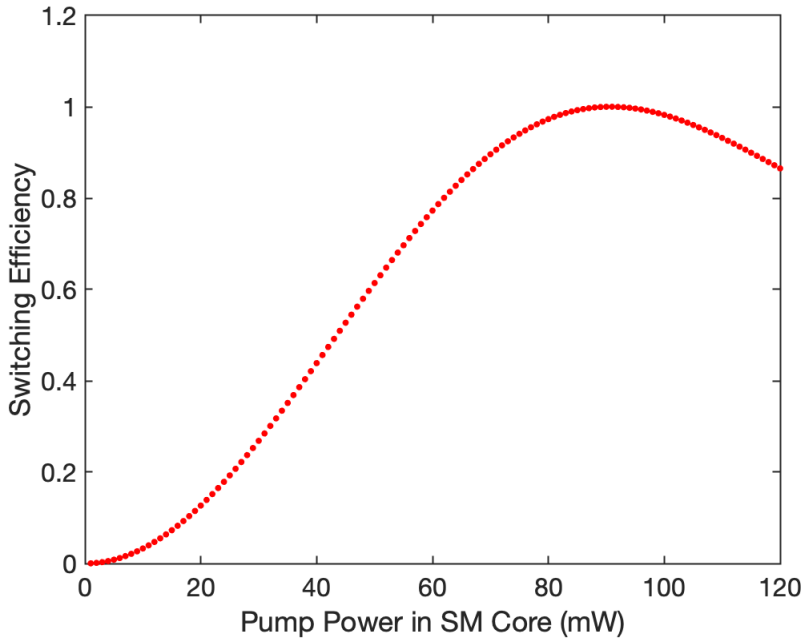

Figure 5.6: Switching efficiency given by the intrinsic response versus the amount of pump power passing through the core. Figure created by Kate Fenwick.

The higher the pump power entering the Kerr switch, the more difficult it will be to separate the signal from the pump pulse. Additionally, high pump intensities cause other nonlinear $\chi^{(3)}$ processes which add to the noise. These include SPM and stimulated Raman scattering. In the case of the former, SPM causes a broadening of the gate pulse. In the case of the latter, it is sufficient to understand that at high intensity in a material, pump photons can be converted into photons at the Stokes frequency at efficiencies of 10% or more [36]. To investigate the noise profile of the pump, we recorded two types of photon counts at the rotated signal photon APD as the intensity was increased. These were the

number of pump photons (termed singles) and accidental coincidences between the pump and the idler. This was plotted in Fig. 5.7, where the pump power is the average power in the bare fibre core.

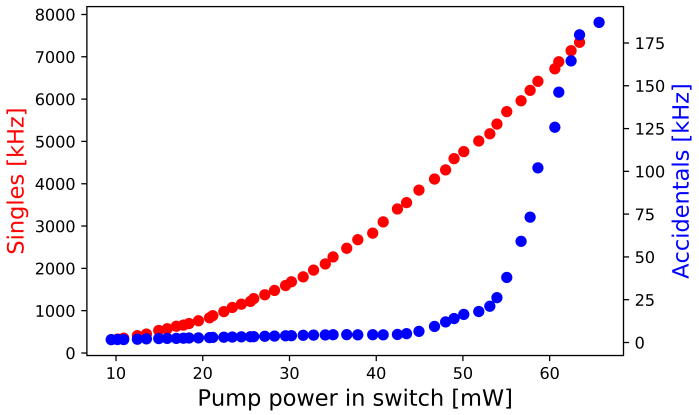

Figure 5.7: Pump noise characterization, looking at number of singles (left ordinate, red) and number of accidental coincidences (right ordinate, blue) vs. pump intensity. The counts are in kHz and the power is the average pump power coupled into the bare fibre.

A spectrum of the detected light at 87.8 mW (corresponding to about 8000 kHz singles and 178 kHz accidentals) was taken by a single photon spectrometer and is shown in Fig. 5.8.

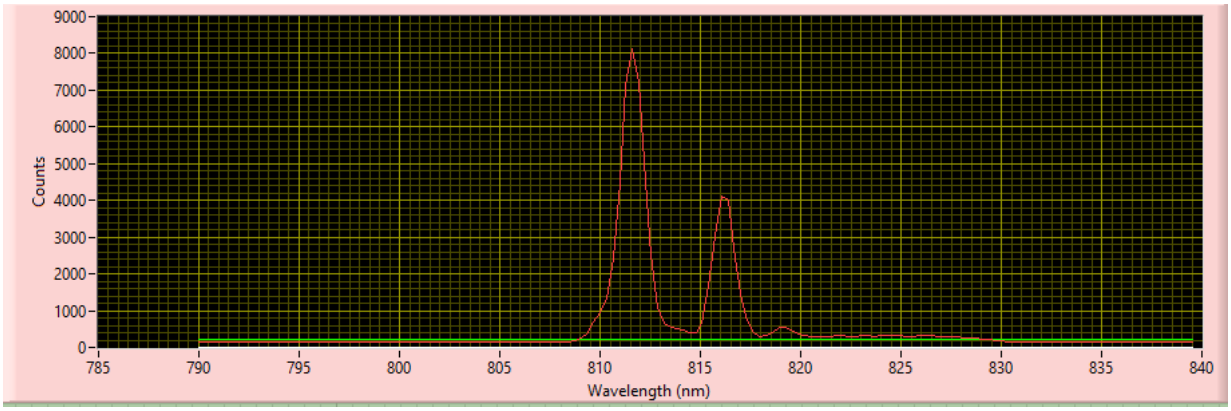

Figure 5.8: The spectrum of the detected light past the switch and the set of four filters, taken with one of the home-built single photon spectrometers.

The number of accidental coincidences increases exorbitantly after 50 mW. This is an

issue as the heralded coincidences are what will be used to indicate switching (a switched signal photon will only be accepted if its presence has been heralded by its idler partner). A majority of these coincidences are due to photons (generated by some nonlinear effect) with wavelengths of 812 nm and 817 nm. Average pump powers of this magnitude are required for good switching efficiency, so a possible workaround is adding another spatial filter to separate these photons from the signal at 823 nm. There is leeway in adjusting the pump and idler frequencies by playing with the phase-matching, so that the produced nonlinear frequencies are shifted away from 823 nm, though more walk-off between the pump and signal will occur in the fibre. There is also an option of switching out the bare fibre for a photonic crystal fibre (Thorlabs NL-2.4-800), which has been specially purchased so that the zero-dispersion point of 800 nm is near the pump and idler wavelengths of 775 nm and 823 nm. The noise characteristics of the photonic crystal fibre are unlikely to be similar to the bare fibre, and a separate analysis has to be done. However, an advantage may be gained because a smaller temporal walk-off between the gate and the signal increases temporal resolution. By choosing an appropriate signal wavelength and fibre length, the switching speed can be increased, possibly by another order of magnitude.

5.5 Concluding remarks and next steps

Discrimination of accidental coincidences from the heralded signal is crucial for observing switching. The signal's temporal width must be estimated so that the theoretical switching response, $\eta_R(T)$ given by Eq. 5.8, can be modelled. After this has been accomplished, we will be able to collect the number of heralded signal photons while a delay is introduced between the pump and the signal in order to generate the experimental response curve. The experimental switching speed is expected to be roughly 0.35 ps. The heralded $g^{(2)}(0)$ will also be calculated to examine how the Kerr switch affects the nonclassical properties of the photons.

The ultrafast all-optical setup has demonstrated Kerr switching of continuous wave light. The completion of the current project will be a proof-of-principle showing that entangled single photons may be switched with high efficiency and on sub-picosecond timescales. Additional adjustments can be made by changing the fibre length and type, and tuning the pump, signal and idler wavelengths to gain a faster switching speed. Based on the switch that motivated this work [83], the current setup mimics their advantages of being relatively simple for implementation: all components are readily commercially available, efficient switching is theoretically achievable with relatively small average pump power, and no active stabilization is required. If successful, it implies further speed improve-

ment in several quantum optics applications such as the conversion of photonic qubits [98], optical computing in a single spatial mode [99], and the processing of high-dimensional and hyperentangled quantum states [100, 101]. The increased switching speed in the Kerr switch may also be employed to improve the timing selectivity in microscopic [102] and spectroscopic [103] techniques.

The Kerr switch is also a promising high-efficiency alternative to current optical gating methods in ultrafast optics which use nonlinear effects like SFG [90, 22]. Future work is aimed toward a full characterization of energy-time entangled photon pairs by building another Kerr switch in the idler path. A FROG-type procedure may be followed by performing cross-correlations in both signal and idler using the gate pulse and implementing a phase-retrieval algorithm, allowing for a high efficiency method of recovering ultrafast two-photon entangled pulses. Ultimately, the switching experiment has potential to add to the plethora of techniques needed to manipulate and measure energy-time entangled single photon pairs, which are necessary to fully exploit single photons in quantum information processes.

References

[1] Michael A. Nielsen and Isaac L. Chuang. *Quantum Computation and Quantum Information*. Cambridge University Press, 2000.

[2] Reinhard F. Werner. Quantum states with Einstein-Podolsky-Rosen correlations admitting a hidden-variable model. *Phys. Rev. A*, 40:4277–4281, Oct 1989.

[3] Ryszard Horodecki, Paweł Horodecki, Michał Horodecki, and Karol Horodecki. Quantum entanglement. *Rev. Mod. Phys.*, 81:865–942, Jun 2009.

[4] Otfried Gühne and Géza Tóth. Entanglement detection. *Physics Reports*, 474(1-6):1–75, Apr 2009.

[5] Joonwoo Bae. Discrimination of two-qubit unitaries via local operations and classical communication. *Scientific Reports*, 5(1), Dec 2015.

[6] Charles H. Bennett, David P. DiVincenzo, Christopher A. Fuchs, Tal Mor, Eric Rains, Peter W. Shor, John A. Smolin, and William K. Wootters. Quantum nonlocality without entanglement. *Physical Review A*, 59(2):1070–1091, Feb 1999.

[7] Andrew G. White, Daniel F. V. James, Philippe H. Eberhard, and Paul G. Kwiat. Nonmaximally entangled states: Production, characterization, and utilization. *Phys. Rev. Lett.*, 83:3103–3107, Oct 1999.

[8] Richard Jozsa. Fidelity for Mixed Quantum States. *Journal of Modern Optics*, 41(12):2315–2323, December 1994.

[9] J. I. Cirac and P. Zoller. Quantum computations with cold trapped ions. *Phys. Rev. Lett.*, 74:4091–4094, May 1995.

[10] Morten Kjaergaard, Mollie E. Schwartz, Jochen Braumüller, Philip Krantz, Joel I.-J. Wang, Simon Gustavsson, and William D. Oliver. Superconducting qubits: Current state of play. *Annual Review of Condensed Matter Physics*, 11(1):369–395, Mar 2020.

[11] B.E. Kane. A silicon-based nuclear spin quantum computer. *Nature*, 393:133–137, May 1998.

[12] B. Brecht, Dileep V. Reddy, C. Silberhorn, and M. G. Raymer. Photon temporal modes: A complete framework for quantum information science. *Phys. Rev. X*, 5:041017, Oct 2015.

[13] M. Krenn, M. Malik, M. Erhard, and A. Zeilinger. Orbital angular momentum of photons and the entanglement of laguerre–gaussian modes. *Philosophical transactions. Series A, Mathematical, physical, and engineering sciences*, 375:20150442, Feb 2017.

[14] A.M. Yao and M.J. Padgett. Orbital angular momentum: origins, behavior and applications. *Advances in Optics and Photonics*, 3:161–204, 2011.

[15] Antonio Manzalini. Topological photonics for optical communications and quantum computing. *Quantum Reports*, 2(4):579–590, 2020.

[16] Thomas Durt, Berthold-Georg Englert, Ingemar Bengtsson, and Karol Życzkowski. On mutually unbiased bases. *International Journal of Quantum Information*, 08(04):535–640, Jun 2010.

[17] Jay N. Damask. *Elements and Basic Combinations*, page 143–210. Springer, 2011.

[18] Paul G. Kwiat, Edo Waks, Andrew G. White, Ian Appelbaum, and Philippe H. Eberhard. Ultrabright source of polarization-entangled photons. *Physical Review A*, 60(2):R773–R776, Aug 1999.

[19] Matthias Bock, Andreas Lenhard, Christopher Chunnilall, and Christoph Becher. Highly efficient heralded single-photon source for telecom wavelengths based on a PPLN waveguide. *Optics Express*, 24(21):23992–24001, 2016.

[20] Daniele Cozzolino, Beatrice Da Lio, Davide Bacco, and Leif Katsuo Oxenløwe. High-dimensional quantum communication: Benefits, progress, and future challenges. *Advanced Quantum Technologies*, 2(12):1900038, Oct 2019.

[21] Bänz Bessire, Christof Bernhard, André Stefanov, and Thomas Feurer. Qudit implementations with broadband energy-time entangled photons. In *2013 Conference on Lasers Electro-Optics Europe International Quantum Electronics Conference CLEO EUROPE/IQEC*, page 1, 2013.

[22] Jean-Philippe W. MacLean, John M. Donohue, and Kevin J. Resch. Direct characterization of ultrafast energy-time entangled photon pairs. *Phys. Rev. Lett.*, 120:053601, Jan 2018.

[23] Stefano Mancini, Vittorio Giovannetti, David Vitali, and Paolo Tombesi. Entangling macroscopic oscillators exploiting radiation pressure. *Phys. Rev. Lett.*, 88:120401, Mar 2002.

[24] Kevin J. Resch. *Quantum optics*. University of Waterloo, 2020.

[25] J. D. Franson. Bell inequality for position and time. *Phys. Rev. Lett.*, 62:2205–2208, May 1989.

[26] Michael A. Horne, Abner Shimony, and Anton Zeilinger. Two-particle interferometry. *Phys. Rev. Lett.*, 62:2209–2212, May 1989.

[27] R. Brown and R.Q. Twiss. Correlation between photons in two coherent beams of light. *Nature*, 177:27–29, Jan 1956.

[28] Kevin Zielnicki, Karina Garay-Palmett, Daniel Cruz-Delgado, Hector Cruz-Ramirez, Michael F. O'Boyle, Bin Fang, Virginia O. Lorenz, Alfred B. U'Ren, and Paul G. Kwiat. Joint spectral characterization of photon-pair sources. *Journal of Modern Optics*, 65:1141–1160, 2018.

[29] M. Beck. Comparing measurements of $g^{(2)}(0)$ performed with different coincidence detection techniques. *Journal of the Optical Society of America B*, 24(12):2972–2978, dec 2007.

[30] Mónica B. Agüero, Alejandro A. Hnilo, and Marcelo G. Kovalsky. Measuring the entanglement of photons produced by a nanosecond pulsed source. *Journal of the Optical Society of America B*, 31(12):3088, Nov 2014.

[31] M. D. Eisaman, J. Fan, A. Migdall, and S. V. Polyakov. Invited review article: Single-photon sources and detectors. *Review of Scientific Instruments*, 82(7):071101, Jul 2011.

[32] Andrew Marc Weiner. *Ultrafast optics*. Wiley, 2009.

[33] Kraig E. Sheetz and Jeff Squier. Ultrafast optics: Imaging and manipulating biological systems. *Journal of Applied Physics*, 105(5):051101, Mar 2009.

[34] Hadeel Elayan, Osama Amin, Raed M. Shubair, and Mohamed-Slim Alouini. Terahertz communication: The opportunities of wireless technology beyond 5G. In *2018 International Conference on Advanced Communication Technologies and Networking (CommNet)*, pages 1–5, 2018.

[35] Yasukazu Izawa, Noriaki Miyanaga, Junji Kawanaka, and Koichi Yamakawa. High power lasers and their new applications. *Journal of the Optical Society of Korea*, 12(3):175–185, 2008.

[36] Robert W. Boyd. *Nonlinear optics*. Academic Press is an imprint of Elsevier, 2020.

[37] David Jeffrey Griffiths. *Introduction to electrodynamics*. Cambridge University Press, 2018.

[38] Annamaria Dosseva, Łukasz Cincio, and Agata M. Brańczyk. Shaping the joint spectrum of down-converted photons through optimized custom poling. *Physical Review A*, 93(1), Jan 2016.

[39] W. P. Grice and I. A. Walmsley. Spectral information and distinguishability in type-II down-conversion with a broadband pump. *Phys. Rev. A*, 56:1627–1634, Aug 1997.

[40] Francesco Graffitti, Dmytro Kundys, Derryck T Reid, Agata M Brańczyk, and Alessandro Fedrizzi. Pure down-conversion photons through sub-coherence-length domain engineering. *Quantum Science and Technology*, 2(3):035001, 2017.

[41] David S. Hum and Martin M. Fejer. Quasi-phasematching. *Comptes Rendus Physique*, 8(2):180–198, 2007. Recent advances in crystal optics.

[42] Rick Trebino. *Frequency-resolved optical gating: the measurement of ultrashort laser pulses*. Kluwer, 2002.

[43] C. Iaconis and I.A. Walmsley. Self-referencing spectral interferometry for measuring ultrashort optical pulses. *IEEE Journal of Quantum Electronics*, 35(4):501–509, 1999.

[44] Ian A. Walmsley and Christophe Dorrer. Characterization of ultrashort electromagnetic pulses. *Advances in Optics and Photonics*, 1:308–437, 2009.

[45] K.W. Delong, Rick Trebino, J. Hunter, and W.E. White. Frequency-resolved optical gating with the use of second-harmonic generation. *Journal of the Optical Society of America B*, 11(11):2206–2215, 1994.

[46] Andrew R. Cameron, Sandra W. L. Cheng, Sacha Schwarz, Connor Kapahi, Dusan Sarenac, Michael Grabowecky, David G. Cory, Thomas Jennewein, Dmitry A. Pushin, and Kevin J. Resch. Remote state preparation of single photon orbital angular momentum lattices, 2021.

[47] Ebrahim Karimi, Lorenzo Marrucci, Vincenzo Grillo, and Enrico Santamato. Spin-to-orbital angular momentum conversion and spin-polarization filtering in electron beams. *Phys. Rev. Lett.*, 108:044801, Jan 2012.

[48] Vincenzo Grillo, Tyler R. Harvey, Federico Venturi, Jordan S. Pierce, Roberto Balboni, Frédéric Bouchard, Gian Carlo Gazzadi, Stefano Frabboni, Amir H. Tavabi, Zi-An Li, Rafal E. Dunin-Borkowski, Robert W. Boyd, Benjamin J. McMorran, and Ebrahim Karimi. Observation of nanoscale magnetic fields using twisted electron beams. *Nature Communications*, 8, Sept 2017.

[49] Dusan Sarenac, Connor Kapahi, Wangchun Chen, Charles W. Clark, David G. Cory, Michael G. Huber, Ivar Taminiau, Kirill Zhernenkov, and Dmitry A. Pushin. Generation and detection of spin-orbit coupled neutron beams. *Proceedings of the National Academy of Sciences*, 116(41):20328–20332, 2019.

[50] Andrei V. Afanasev, D. V. Karlovets, and V. G. Serbo. Schwinger scattering of twisted neutrons by nuclei. *Phys. Rev. C*, 100:051601, Nov 2019.

[51] D. Sarenac, J. Nsofini, I. Hincks, M. Arif, C. W. Clark, D. G. Cory, M. G. Huber, and D. A. Pushin. Methods for preparation and detection of neutron spin-orbit states. *New Journal of Physics*, 20(10):103012, oct 2018.

[52] Denis A. Ikonnikov, Sergey A. Myslivets, Mikhail N. Volochaev, Vasily G. Arkhipkin, and Andrey M. Vyunishev. Two-dimensional Talbot effect of the optical vortices and their spatial evolution. *Scientific Reports*, 10(1):20315, November 2020.

[53] S. Schwarz, C. Kapahi, R. Xu, A. R. Cameron, D. Sarenac, J. P. W. MacLean, K. B. Kuntz, D. G. Cory, T. Jennewein, K. J. Resch, and D. A. Pushin. Talbot effect of orbital angular momentum lattices with single photons. *Phys. Rev. A*, 101:043815, Apr 2020.

[54] Xinzhong Li, Haixiang Ma, Hao Zhang, Yuping Tai, Hehe Li, Miaomiao Tang, Jingge Wang, Jie Tang, and Yangjian Cai. Close-packed optical vortex lattices with controllable structures. *Opt. Express*, 26(18):22965–22975, Sep 2018.

[55] Yu-Jing Han, Zhen-Yu Rong, Li Zhang, and Xiao-Yi Chen. Generation of propagation-invariant vector beams with square array by use of 2d binary phase mask and pentagonal prism. *Appl. Opt.*, 58(23):6325–6328, Aug 2019.

[56] Dusan Sarenac, Connor Kapahi, Andrew E. Silva, David G. Cory, Ivar Taminiau, Benjamin Thompson, and Dmitry A. Pushin. Direct discrimination of structured light by humans. *Proceedings of the National Academy of Sciences*, 117(26):14682–14687, 2020.

[57] Dusan Sarenac, Andrew E. Silva, Connor Kapahi, Ben Thompson, David G. Cory, and Dmitry A. Pushin. Human psychophysical discrimination of spatially dependant Pancharatnam-Berry phases in optical spin-orbit states, 2020.

[58] M. F. Andersen, C. Ryu, Pierre Clade, Vasant Natarajan, A. Vaziri, K. Helmerson, and W. D. Phillips. Quantized rotation of atoms from photons with orbital angular momentum. *Phys. Rev. Lett.*, 97:170406, Oct 2006.

[59] H. He, M. E. J. Friese, N. R. Heckenberg, and H. Rubinsztein-Dunlop. Direct observation of transfer of angular momentum to absorptive particles from a laser beam with a phase singularity. *Phys. Rev. Lett.*, 75:826–829, Jul 1995.

[60] N. V. Morrow, S. K. Dutta, and G. Raithel. Feedback control of atomic motion in an optical lattice. *Phys. Rev. Lett.*, 88:093003, Feb 2002.

[61] Christian T Schmiegelow, Jonas Schulz, Henning Kaufmann, Thomas Ruster, Ulrich G Poschinger, and Ferdinand Schmidt-Kaler. Transfer of optical orbital angular momentum to a bound electron. *Nature Communications*, 7(1):12998, 2016.

[62] Xi-Wang Luo, Xingxiang Zhou, Jin-Shi Xu, Chuan-Feng Li, Guang-Can Guo, Chuanwei Zhang, and Zheng-Wei Zhou. Synthetic-lattice enabled all-optical devices based on orbital angular momentum of light. *Nature Communications*, 8(1):16097, July 2017.

[63] Eleni Diamanti, Hoi-Kwong Lo, Bing Qi, and Zhiliang Yuan. Practical challenges in quantum key distribution. *npj Quantum Information*, 2(1):16025, November 2016.

[64] Mhlambululi Mafu, Angela Dudley, Sandeep Goyal, Daniel Giovannini, Melanie McLaren, Miles J. Padgett, Thomas Konrad, Francesco Petruccione, Norbert Lütkenhaus, and Andrew Forbes. Higher-dimensional orbital-angular-momentum-based quantum key distribution with mutually unbiased bases. *Phys. Rev. A*, 88:032305, Sep 2013.

[65] Jino Heo, Min-Sung Kang, Chang-Ho Hong, Hyung-Jin Yang, Seong-Gon Choi, and Jong-Phil Hong. Distribution of hybrid entanglement and hyperentanglement with time-bin for secure quantum channel under noise via weak cross-Kerr nonlinearity. *Scientific Reports*, 7(1):10208, 2017.

[66] Isaac Nape, Nikiwe Mashaba, Nokwazi Mphuthi, Sruthy Jayakumar, Shanti Bhattacharya, and Andrew Forbes. Vector-mode decay in atmospheric turbulence: An analysis inspired by quantum mechanics. *Phys. Rev. Applied*, 15:034030, Mar 2021.

[67] Ilaria Gianani, Alessia Suprano, Taira Giordani, Nicolò Spagnolo, Fabio Sciarrino, Dimitris Gorpas, Vasilis Ntziachristos, Katja Pinker, Netanel Biton, Judy Kupferman, and Shlomi Arnon. Transmission of vector vortex beams in dispersive media. *Advanced Photonics*, 2(3):1 – 8, 2020.

[68] Willner, Alan E. and Liu, Cong. Perspective on using multiple orbital-angular-momentum beams for enhanced capacity in free-space optical communication links. *Nanophotonics*, 10(1):225–233, 2021.

[69] Cheng, Wenchi and Zhang, Wei and Jing, Haiyue and Gao, Shanghua and Zhang, Hailin. Orbital Angular Momentum for Wireless Communications. *IEEE Wireless Communications*, 26(1):100–107, 2019.

[70] Zhang, Wei and Ding, Dong-Sheng and Dong, Ming-Xin and Shi, Shuai and Wang, Kai and Liu, Shi-Long and Zhou, Zhi-Yuan and Shi, Bao-Sen and Guo, Guang-Can. Experimental realization of entanglement in multiple degrees of freedom between two quantum memories. *Nature Communications*, 7:13514, Nov 2016.

[71] Lydia Vermeyden. Fundamental tests of quantum mechanics using two-photon entanglement. Master's thesis, University of Waterloo, 2014.

[72] Deny R. Hamel. Realization of novel entangled photon sources using periodically poled materials. Master's thesis, University of Waterloo, 2010.

[73] Charles H. Bennett, David P. DiVincenzo, Peter W. Shor, John A. Smolin, Barbara M. Terhal, and William K. Wootters. Remote state preparation. *Phys. Rev. Lett.*, 87:077902, Jul 2001.

[74] D. Sarenac, D. G. Cory, J. Nsofini, I. Hincks, P. Miguel, M. Arif, Charles W. Clark, M. G. Huber, and D. A. Pushin. Generation of a lattice of spin-orbit beams via coherent averaging. *Phys. Rev. Lett.*, 121:183602, Oct 2018.

[75] Joachim Nsofini, Dusan Sarenac, Christopher J. Wood, David G. Cory, Muhammad Arif, Charles W. Clark, Michael G. Huber, and Dmitry A. Pushin. Spin-orbit states of neutron wave packets. *Phys. Rev. A*, 94:013605, Jul 2016.

[76] Teledyne Princeton Instruments. *PI-Max4 Camera System*, 10 edition, March 2019.

[77] Matthew Brown. Bohmian mechanics: Towards illuminating the quantum potential. Master's thesis, University of Waterloo, 2018.

[78] Daniel F. V. James, Paul G. Kwiat, William J. Munro, and Andrew G. White. Measurement of qubits. *Phys. Rev. A*, 64:052312, Oct 2001.

[79] L. Marrucci, C. Manzo, and D. Paparo. Optical spin-to-orbital angular momentum conversion in inhomogeneous anisotropic media. *Phys. Rev. Lett.*, 96:163905, Apr 2006.

[80] Ebrahim Karimi, Bruno Piccirillo, Eleonora Nagali, Lorenzo Marrucci, and Enrico Santamato. Efficient generation and sorting of orbital angular momentum eigenmodes of light by thermally tuned q-plates. *Applied Physics Letters*, 94(23):231124, May 2009.

[81] A.A. Zinchik. Application of spatial light modulators for generation of laser beams with a spiral phase distribution. *Scientific and Technical Journal of Information Technologies, Mechanics and Optics*, 15:817–824, 2015.

[82] Netanel Biton, Judy Kupferman, and Shlomi Arnon. OAM light propagation through tissue. *Scientific Reports*, 11(2407), 2021.

[83] Connor Kupchak, Jennifer Erskine, Duncan England, and Benjamin Sussman. Terahertz-bandwidth switching of heralded single photons. *Optics Letters*, 44(6):1427–1430, 2019.

[84] Sebastian Werner, Javier Navaridas, and Mikel Lujń. A survey on optical network-on-architecture. *ACM Computing Surveys*, 50(6):1–37, Jan 2018.

[85] V. Sasikala and K. Chitra. All optical switching and associated technologies: a review. *Journal of Optics*, 47(3):307–317, 2018.

[86] Amer Kotb. Simulation of high quality factor all-optical logic gates based on quantum-dot semiconductor optical amplifier at 1Tb/s. *Optik: International Journal for Light and Electron Optics*, 127(1):320–325, 2016.

[87] Robert Prevedel, Philip Walther, Felix Tiefenbacher, Pascal Böhi, Rainer Kaltenbaek, Thomas Jennewein, and Anton Zeilinger. High-speed linear optics quantum computing using active feed-forward. *Nature*, 445(7123):65–69, Jan 2007.

[88] S. Andersson-Engels, S. Berg, S. Svanberg, and Jarlman O. Time-resolved transillumination for medical diagnostics. *Optics Letters*, 15(21):1179–1181, 1990.

[89] Giuseppe Vicidomini, Gael Moneron, Kyu Y Han, Volker Westphal, Haisen Ta, Matthias Reuss, Johann Engelhardt, Christian Eggeling, and Stefan W Hell. Sharper low-power STED nanoscopy by time gating. *Nature Methods*, 8(7):571–573, 2011.

[90] Jean-Philippe W. MacLean, Sacha Schwarz, and Kevin J. Resch. Reconstructing ultrafast energy-time-entangled two-photon pulses. *Phys. Rev. A*, 100:033834, Sep 2019.

[91] Abdul-Hamid Fattah, Assegid Mengistu Flatae, Amr Farrag, and Mario Agio. Ultrafast single-photon detection at high repetition rates based on optical Kerr gates under focusing. *Opt. Lett.*, 46(3):560–563, Feb 2021.

[92] J. Etchepare, G. Grillon, R. Muller, and A. Orszag. Kinetics of optical Kerr effect induced by picosecond laser pulses. *Optics Communications*, 34(2):269–272, aug 1980.

[93] Hirohisa Kanbara, Hideki Kobayashi, Toshikuni Kaino, Takashi Kurihara, Naoki Ooba, and Ken'ichi Kubodera. Highly efficient ultrafast optical Kerr shutters with the use of organic nonlinear materials. *Journal of the Optical Society of America B*, 11(11):2216, 1994.

[94] G.P. Agrawal. *Nonlinear fiber optics*. Academic Press, 1995.

[95] I.H. Malitson. Interspecimen comparison of the refractive index of fused silica. *Journal of the Optical Society of America*, 55(10):1205–1209, 1965.

[96] Kate L. Fenwick. Exploiting ultrafast optical pulses: probing excitonic properties of 2D materials and utilizing the Kerr effect for all-optical switching. Master's thesis, Queen's University, 2019.

[97] Jean-Philippe MacLean. *Ultrafast Metrology in the Quantum Domain*. PhD thesis, University of Waterloo, 2019.

[98] J. Brendel, N. Gisin, W. Tittel, and H. Zbinden. Pulsed energy-time entangled twin-photon source for quantum communication. *Physical Review Letters*, 82(12):2594–2597, Mar 1999.

[99] Peter C. Humphreys, Benjamin J. Metcalf, Justin B. Spring, Merritt Moore, Xian-Min Jin, Marco Barbieri, W. Steven Kolthammer, and Ian A. Walmsley. Linear optical quantum computing in a single spatial mode. *Physical Review Letters*, 111(15), Oct 2013.

[100] Matthew A. Hall, Joseph B. Altepeter, and Prem Kumar. Ultrafast switching of photonic entanglement. *Phys. Rev. Lett.*, 106:053901, Feb 2011.

[101] Takuya Ikuta and Hiroki Takesue. Implementation of quantum state tomography for time-bin qudits. *New Journal of Physics*, 19:013039, oct 2017.

[102] Jolie C. Blake, Jesus Nieto-Pescador, Zhengxin Li, and Lars Gundlach. Ultraviolet femtosecond Kerr-gated wide-field fluorescence microscopy. *Opt. Lett.*, 41(11):2462–2465, Jun 2016.

[103] Sonja Draxler and Max E. Lippitsch. Time-resolved fluorescence spectroscopy for chemical sensors. *Appl. Opt.*, 35(21):4117–4123, Jul 1996.

[104] E. Knill, R. Laflamme, and G. Milburn. A scheme for efficient quantum computation with linear optics. *Nature*, 409:133–137, May 1998.

[105] Manuel Erhard, Robert Fickler, Mario Krenn, and Anton Zeilinger. Twisted photons: new quantum perspectives in high dimensions. *Light: Science & Applications*, 7(3):17146–17146, 2017.

[106] Christopher C. Gerry and Peter L. Knight. *Introductory quantum optics*. Cambridge Univ. Press, 2008.

[107] Hadi Sarieddeen, Nasir Saeed, Tareq Y. Al-Naffouri, and Mohamed-Slim Alouini. Next Generation Terahertz Communications: A Rendezvous of Sensing, Imaging, and Localization. *IEEE Communications Magazine*, 58(5):69–75, 2020.

[108] J. Ma, M. Weidenbach, R. Guo, M. Koch, and D.M. Mittleman. Communications with THz Waves: Switching Data Between Two Waveguides. *Journal of Infrared, Millimeter and Terahertz Waves*, 38:1316–1320, aug 2017.

APPENDICES

Appendix A

Acquiring optimal gate delay with the emICCD

The PI-Max4: 1024 EMB camera is very sensitive so alignment cannot be done with classical light (in fact, it's so sensitive that opening the lab door when the camera is working poses a significant risk of damage). Choose a single photon signal pattern to observe, and ensure the idler is triggering the camera.

The gate delay is roughly about 100 ns, since it takes the photons about that time to transverse the 30-m-long fibre spool, but the exact delay is unknown. There is a rather straight-forward optimizing algorithm that can be used to find it. The two parameters involved are the gate width, which is the window in which the camera takes data, and the gate delay, which controls when the window starts. Eventually, we want the gate width to be 3 ns, but at the beginning, the window is bigger so that we can easily search for the correct delay. A change in the gate width is a different picture-taking regime, so the emICCD's parameters must be adjusted accordingly.

The idea of the optimization is start with a large gate width, narrow down the gate delays into two halves, choose the half which gives a signal, and repeat. The gate width can be set at a maximum of 500 ns. Just for visualization of the optimization, think about setting the window to be 1-250 ns and 250-500 ns, and then selecting the window in which you can see an image. If the latter is chosen, then check between 250-375 ns and 375-500 ns; so on and so forth. If the other parameters are not adjusted, two outcomes are likely. Either there is no signal even though there should be, so the resulting image is all black, or there is too much noise which results in an all white intensity distribution. These are empirically determined but we recommend starting with:

- Gate width: 200 ns
- Gate delay: 100 ns
- Exposures per frame: 50
- Intensifier gain: 1
- Electron-multiplying (EM) gain: 1
- External trigger: 1.5 V (keep this constant)
- Speed: 10 MHz.

Appendix B

LOV prism alignment

B.1 Classical setup

A classical diode set at the photon wavelength and the BeamView program is used. Different wavelengths travel through the LOV prisms differently due to the refractive index, so if classical alignment is done using a different wavelength, then different intensity distributions will be seen when using single photons on the emICCD. To look at the patterns classically, projective measurements must be performed, else you will only see a Gaussian beam on the BeamView camera. In Fig. 4.3, keep the HWP, QWP, and PBS after the LOV prism pairs. Moving the HWP and QWP will emulate the signal's projective measurement, so I will refer to these as the **m**easurement waveplates. Put the camera after one of the PBS ports; we chose the transmitted port, effectively choosing to always measure $|H\rangle$. Insert a PBS, a HWP and QWP before the LOV prism pairs. Moving these waveplates in the classical setup will emulate the idler, so I will refer to these as the **p**reparation waveplates. By using the camera, the HWPs and QWPs in this way, you can check that the LOV prisms are properly aligned by ensuring all polarisation measurement choices match the theoretical intensity distributions.

B.2 Classical alignment

Refer to Fig. 4.2. First, ensure the wedges are straight such that the prisms are 90° to both the $\hat{x}$- and $\hat{y}-$axes. Recall that the prisms have befringent axes which cause a multiple of 2π phase as light passes through more of the quartz, so when only the $\hat{U}_y$ prisms are

inserted, they cause horizontal fringes (parallel to the $\hat{y}-$axis). Similarly, when only the $\hat{U}_x$ prisms are inserted, they cause vertical fringes (parallel to the $\hat{x}-$axis). Make sure that these fringes are straight by adjusting the tilt of the prisms. The beam should be aligned for when all four prisms are in place, so when looking at an individual prism, the beam will be deflected slightly and the fringes will be difficult to see. Aligning in pairs makes them easier to see, but check that the prisms are straight not just relative to each other. After locking in the phase via an Allen key, look at the other prism pair.

Now, we emulate what the emICCD will see with the $|\Phi^+\rangle$ Bell state by using classical light by setting the measurement and preparation waveplates. We liberally used the waveplate basis conversion guide in the QOQI Wiki. First, align the prisms nicely by observing the classical $|R\rangle_p$, $|R\rangle_m$ measurement, since its donut pattern is the easiest to evaluate qualitatively. Adjust the translation knobs (the right/left knobs should only affect the $\hat{U}_y$ prisms, and the up/down knobs should only affect the $\hat{U}_x$ prisms) so that the donut pattern looks even and centred in the beam. Then check the classical $|H\rangle_p$, $|V\rangle_m$ and the $|A\rangle_p$, $|D\rangle_m$ measurements, whose intensity distributions are horizontal and vertical bars respectively. Re-iterate with the knobs so that all of the patterns are correct, and qualitatively look even and centred. After this is done, begin comparing the set of $\{H, V, D, R\}$, shown in Fig. B.1, to the theoretical distributions (Fig. 4.4(a)). Adjust the translation knobs as needed.

Brief projective measurement examples:

- e.g. to look at the classical intensity distribution of $|V\rangle_p$, $|D\rangle_m$, set the preparation waveplates to send $|H\rangle$ to $|V\rangle$, assuming the newly-inserted PBS allows transmitted light to pass through these waveplates. Set the measurement waveplates to send $|D\rangle$ to $|H\rangle$, since we are reading out the transmitted port of the second PBS.

- Recall Eq. 4.3 which shows that the only anti-correlations are with $\{|R\rangle, |L\rangle\}$. If the idler in the RSP experiment is projected to $|L\rangle$, the signal gets the equatorial state $|R\rangle$. So any classical intensity distribution that wants to look at an $|R\rangle$ projection with the measurement waveplates must actually have $|L\rangle$ instead. e.g. to look at what the $|R\rangle_i$,$|R\rangle_s$ will be, set the classical intensity distribution to $|R\rangle_p$, $|L\rangle_m$. The preparation waveplates should send $|H\rangle$ to $|R\rangle$ and the measurement waveplates should send $|L\rangle$ to $|H\rangle$.

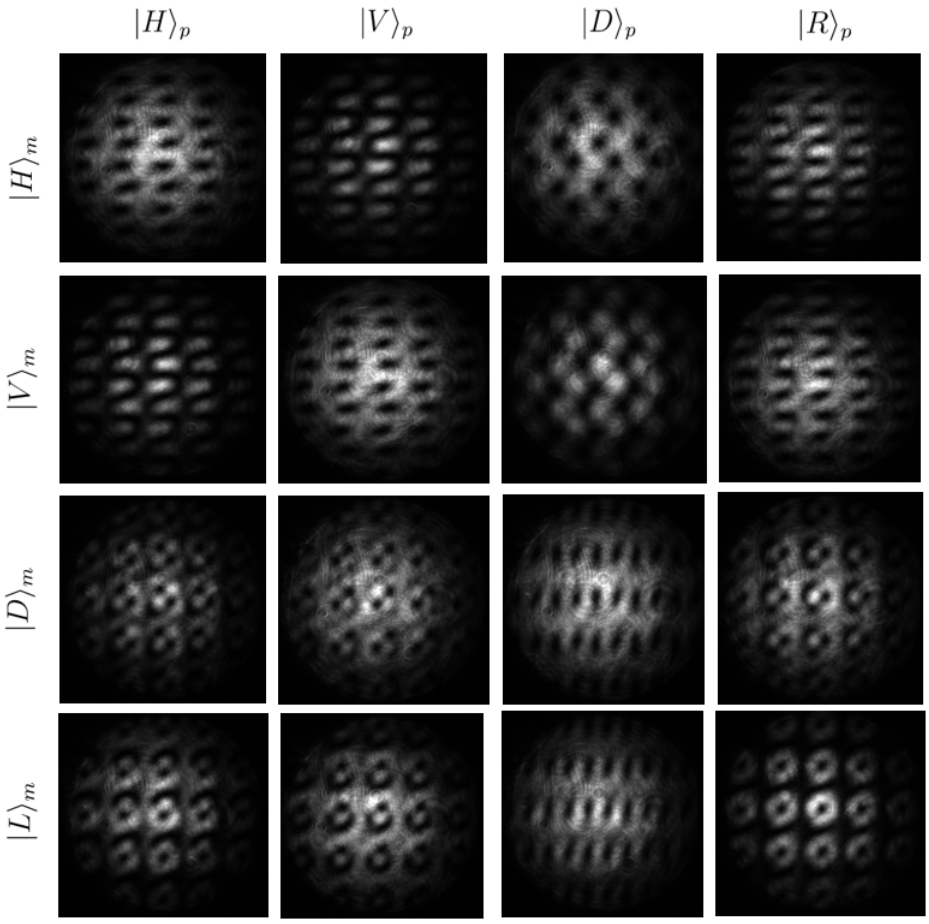

Figure B.1: Intensity distributions using a classical diode and the BeamView camera. Compare to Fig. 4.4(a) to check LOV prism alignment. Note that the patterns are a good representation of the experimental intensity distributions in Fig. 4.4(b), including pattern distortion.

Other notes:

- If the images do not match the theoretical intensity distributions, it may be that one of the crystals is inserted wrongly (e.g. flipped across an axis). There's no easy way to see this because the prisms are hidden in their Thorlabs holders.
- Make sure the QWPs are not backwards. We double-checked but only caught this on the third go.

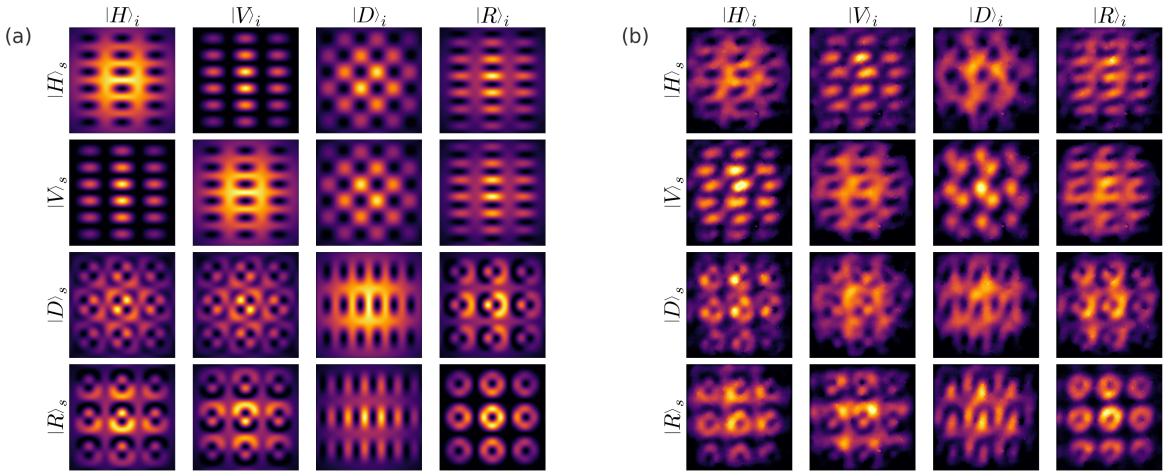

Fig. 4.4 reproduced here for convenience. Theoretical predictions (a) and experimental results (b) are shown for the tomographically complete set of $\{|H\rangle, |V\rangle, |D\rangle, |R\rangle\}$.

Appendix C

Finding coincidences with the Chameleon source

C.1 Historical context

The Chameleon Ultra II source of single photons normally only needs a quick tune-up using the signal and idler couplers and the angle phase-matching, even after months of being untouched. However, after Andrew and I were finally allowed back into the lab for the first time during the pandemic, the Chameleon was broken and had to be shipped off for repair. When it returned, we had to align this source from point zero to its usual state of generating non-degenerate single photon pair coincidences. The full alignment guide is in the QOQI Wiki, but the most difficult part was obtaining coincidences, which is detailed below.

C.2 Finding coincidences

At this point, the laser should be aligned such that there are single photon counts in both the signal and the idler couplers, but there aren't any coincidences. Frequency, polarisation, and timing are not the issues at hand. You will have checked this by looking at the signal and idler spectra, by ensuring the correct polarisation produced by the SPDC is allowed through each coupler, and by observing the timing histogram VI to note the correct delay between the two detectors.

If the above 3 DoFs are not causing the issue, then the most likely reason why coincidences are not seen is because of spatial correlations. The probabilities of the spatial positions of the down-converted daughter photons can be thought of as two emerging light cones. Each photon has a partner which exists in a particular geometric part of the other cone. The problem is that the signal and idler couplers are attached to detectors via SMFs which only capture a minuscule amount of the light cones, plus it is difficult to know which spatial parts of the cones are being seen. Our alignment method relies on the idea that in type-I SPDC, the two light cones emerge collinearly and are very overlapped, so the partner photons are in roughly the same position in each cone. Each light cone is mapped out, and then each coupler is moved to its centre.

1. Designate directions (up, down, left, right) with the translation stage knobs. Choose one coupler.

2. Look at the number of the singles. Choose a direction to explore and keep track of your movements with the micrometer notches. Every time a movement is made with the translation, recover the singles by using both tilts. Continue in the same direction until the singles count has dropped by $\approx$ 15%. You've now found one edge of the map!

3. Now, move in the opposite direction with the translations. Similarly, record your movements, and recover at each step with both tilts. Continue until the singles once again drop $\approx$ 15%. This is the other edge!

4. Now knowing both edges of one axis, move to the centre coordinate using the translation knob, and maximize singles with the tilts.

5. In the other axis, choose one direction to move. Use the same technique with the translations and recovering singles with the tilts. Move to the centre coordinate after finding it!

6. Follow the above procedure for the second coupler; as you get closer to its centre, coincidences should get larger!

For reference, Andrew and I mapped each cone to be roughly 10×10 mm in about an hour. It is possible that even with this method, coincidences are absent. In this case, try spiralling from the centre. This method involves drawing out a spiral pattern using one of the couplers e.g. moving left by one unit, up one unit, right two units, down two units, etc. We also believe that our method could be tweaked for type-II SPDC, where

the outgoing polarisations of the daughter photons are different, so the entangled photon pairs are no longer in the same position of the cones but are still at intersections where the cones overlapped.

Appendix D

Bare fibre handling

D.1 General lab notes

- Andrew cut all of the bare fibre at the RAC 2 building after being trained to do so. It is BYOF (bring-your-own-fibre). The smallest length of bare fibre he has been able to produce is 1.5 cm.
- We store the bare fibre in old Thorlabs circular fibre containers, sandwiched by two pieces of foam.
- Sacha and Andrew had previously observed that having a high-powered pump input misaligned the fibre and reduced coupling. Andrew and I believe that this is due to heat being absorbed by the clamp near the tip of the bare fibre, since the old holder (Thorlabs: HFF003) is black, and the new holder (Thorlabs: HFF001) is silver and has no noticeable power issue.
- We set the fibre into the holder by using a pair of optic tweezers (Thorlabs: TZ1). When setting the fibre into the grooves of the holder, we carefully nudged the middle of the fibre to get it in place, and left the fibre ends untouched. The tip of the fibre should be barely poking out of the holder, so that (a) it does not bend or succumb to weird air pressure changes and (b) it is easier for the laser to enter the fibre tip rather than lighting up the clamp.
- The bare fibre is fragile, so accidents were bound to happen (sorry, Andrew). Broken or ruined fibre went into a sharps container. I built a roofed cage over the fibre to prevent overhead mishaps.

D.2 Core alignment procedure

A bare fibre's core is very small (3.5 μm for S630-HP Thorlabs fibre), so coupling light into it from free space is not easy. When first coupling into bare fibre, most of the light will probably pass through the cladding instead. On the BeamView program, the output resembles speckled donuts. When the light is truly passing through the core, the output is Gaussian since the core is designed to output the TEM_{00} spatial mode. Moving away from this position in any of the four directions (up/down or in/out of the table; not the optical axis) results in the speckled donut output and eventually followed by blackness. Note that as the fibre gets shorter, less of the cladding modes are killed, which results in messier Gaussian profiles as shown in Figs. D.1 and D.2. It is important to ensure that the camera isn't saturated, else light through the cladding can appear Gaussian. With at least a 10-cm-long fibre, these messy cladding modes are removed entirely.

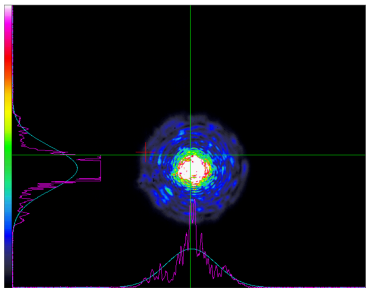

(a) 3 cm bare fibre length.

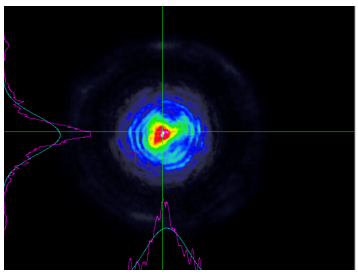

(b) 1.5 cm bare fibre length.

Figure D.1: Classical beam profiles after passing through bare fibre core. Both images were taken with BeamView with the Chameleon at 823 nm, the idler wavelength.

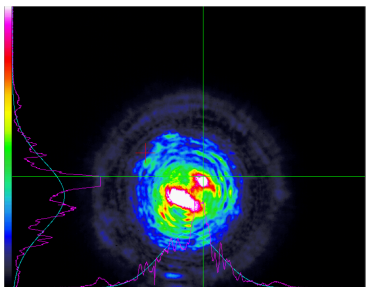

(a) 3 cm bare fibre length.

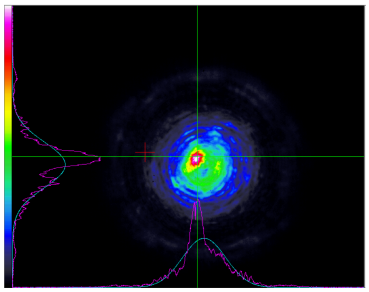

(b) 1.5 cm bare fibre length.

Figure D.2: Classical beam profiles after passing through bare fibre core. Both images were taken with BeamView with the Chameleon at 775 nm, the pump wavelength.

D.2.1 Initial setup

First, align the pump and idler paths using the camera, with at least two irises and a poker.

Now, secure the bare fibre into its holder, and place the front lens on its separate holder outfitted with controls. The adjustment of the lens is fiddly, but place it such that the tip of the bare fibre is very near its focal length. Make sure the lens is straight relative to the fibre. Put the camera directly after the fibre's end. Note that after exiting fibre core, light shoots out and diverges very quickly, so put the camera close to catch its output.

The goal now is to move the lens controls such that both light paths focus into the fibre. Aim to see the cladding modes. The holder heights should've been set with the same poker, so hopefully you won't be too far off. I recommend using the wavelength which is most visible by eye (for us, this was the pump), so that you can see when the light is hitting the holder and adjust. At your own risk, you could also ***very carefully*** put an IR card between the lens and the fibre tip to check if the light is being focused onto the tip.

D.2.2 Finding the core

At this point, light should be passing through the cladding but not the core. The focus is likely in a sub-optimal position. Here, we apply the fact that these fibres are manufactured to be nearly perfectly coaxial.

1. Choose a position using the fine zoom control on the front lens. Keep track using the micrometer notches.

2. Scan through the one of the other two directions (up/down or in/out of the table) with the lens control. You should notice on the BeamView program that the speckled donuts should fade to nearly nothing at each end of the chosen direction. Adjust the control so that it is in between those two end positions. Keeping track of the micrometer notches is helpful e.g. if the light fades to dark at 10 μm and 100 μm, move to the centre which is at 55 μm.

3. Similarly, scan through the other direction to find the centre coordinate.

4. Reiterate these steps until the emerging light is Gaussian.

Once you have found the core, put the collimating lens behind the fibre end. You can have it in before finding the core, but the output may be misleadingly Gaussian. You can test this by adjusting the zoom of the collimating lens.

This is the end of the hardest part! Now, whenever you take out the fibre or replace it, you should be really close to the core. Just play the game with finding the middle in both directions without touching the zoom. It should take less than 20 minutes.